Modelling bubbly flows using Volume of Fluid, Front Tracking and Discrete Bubble Models

promotie commissie:
dr. R.P.J. Duursma
prof.dr. B.H. Hjertager
prof.dr. R.F. Mudde
prof.dr.ir. J.A.M. Kuipers (promotor)
dr.ir. M.van Sint Annaland (assistent promotor)
prof.dr. G. Tryggvason
prof.dr. J.J.W. van der Vegt
prof.dr.ir. M.M.C.G. Warmoeskerken
prof.dr.ir. L. van Wijngaarden (voorzitter)

Twente University **Press**

P.O. box 217, 7500 AE Enschede, The Netherlands

This study was funded by *CORUS RD&T*.

©2004 Michiel Gunsing, Ede, The Netherlands

No part of this book may be reproduced in any form by print, photoprint, microfilm or any othe means without written permission from the author/publisher.

Niets uit deze uigave mag worden vermenigvuldigd en/of openbaar gemaakt door middel van druk, photokopie, microfilm of op enige andere wijze zonder voorafgaande schriftelijke toestemming van de schrijver/uitgever.

CIP-data Koninklijke Bibliotheek, Den haag
Gunsing, Michiel
ISBN 90-365-1800-8

MODELLING OF BUBBLY FLOWS USING VOLUME OF FLUID, FRONT TRACKING AND DISCRETE BUBBLE MODELS

PROEFSCHRIFT

ter verkrijging van
de graad van doctor aan de Universiteit Twente,
op gezag van de rector magnificus,
prof.dr. F.A. van Vught,
volgens besluit van het College voor Promoties
in het openbaar te verdedigen
op donderdag 26 februari 2004 om 16.45 uur

door

Michiel Gunsing

geboren op 17 december 1971

te IJsselstein

Dit proefschrift is goedgekeurd door de promotor

prof.dr.ir. J.A.M. Kuipers

assistent promotor

dr.ir. M. van Sint Annaland.

Summary

Introduction

Intense contact between gasses and liquids is an essential step in many (bio) chemical and metallurgic processes amongst others. A device that is often used for this step of the process is the bubble column. Bubble columns have good mixing characteristics, resulting in good mass and heat transfer qualities. In spite of their frequent application, fundamental knowledge on the behaviour of bubble columns is still lacking. Their design and operation is based on a large number of empirical correlations and scale-up continues to be very complicated. In this thesis, a number of mathematical models have been developed, improved and validated which can help obtain more detailed knowledge on the important phenomena prevailing in gas-liquid dispersed flows.

Modelling

With three different models, two levels of detail (i.e. length and time scales) have been studied. The two most detailed models track the gas-liquid interface and solve both issues of pressure and flow distribution of the gas and the liquid phase. These models focus on the bubble dynamics at the scale of one single bubble. In the first model, the *Front Tracking* algorithm, originating from Unverdi and Tryggvason (1992) is applied, while the second uses the *Volume of Fluid* (*VoF*) algorithm originating from Youngs (1982, 1987).

The improvements that were made to the original models include, for the *Front Tracking* model:

- a new solver strategy for the pressure Poisson equation was included to handle high density ratios up to $\rho_l/\rho_g = 10000$,
- a new, easier approach to the original surface tension model was developed and implemented,
- a re-triangulation algorithm reducing the total surface energy was included,
- an integrated version of the Peskin smoothing function was embedded,
- the re-meshing algorithm to avoid failure due to extreme mesh deformation was improved,
- the evaluation of the local viscosity was computed by harmonic weighing of the kinematic viscosity (Prosperetti, 2001).

and for the *VoF* model:

- a new surface tension model based on the tensile forces between adjacent elements was developed and implemented,
- a smoothening of the colour function over several cells, resulting in a more stable calculation of the Pressure Poisson Equation(PPE) and a more accurate prediction of the orientation of the interface elements.
- a flux correction algorithm was introduced

A second level of detail is modelled using a Eulerian-Lagrangian approach. The Discrete Bubble Model (*DBM*), describes the liquid phase flow field in a complete bubble column and tracks all gas bubbles individually. A typical number of bubbles can go up to about 10^5 bubbles. The gas bubbles tracked by solving the Newtonian laws of motion. Closure relation were used to account for all relevant forces acting on the bubbles. The model accounts for two-way coupling and for the volume occupied by the gas bubbles. The *DBM* model originally developed by Delnoij (1999) was refined by incorporating a number of new elements. These include:

- the introduction of state of the art closure relations,

- a second order accurate Barton flux scheme was introduced,
- the adoption of a LES turbulence model,
- incorporation of a full three dimensional collision algorithm.

Results

Both detailed models were programmed into a computer code and all individual components of the codes were tested separately. Finally, a number of simulations were performed and compared to experimental data taken from the literature. The computed shape and bubble rise velocity agree well with taken from the bubble diagram of Grace (1973). The terminal rise velocity predicted by the models was also compared to velocities obtained from drag closure relations that were taken from Clift et al. (1978). Both models produce reasonably accurate results for the bubble shape and the terminal rise velocity. Although a number of small differences between the models were found, none of the models showed to be significantly more accurate than the others.

The modifications embedded in the *DBM* model were shown to be a significant improvement to its application window and predictive capability. Using the collision algorithm, gas fractions up to 40% can now be evaluated by the model. The addition of the Barton flux scheme proved to have little influence on the dynamics of the bubble column. The introduction of the LES model decreased the mean liquid velocity, as was expected. The new closure relations resulted in a different distribution of the bubbles over the column. Results from simulations ran with the complete model were compared to experimental data obtained from *Particle Image Velocimetry* measurements and showed a reasonable agreement.

Outlook

In future research, a number of improvements and extensions can be made. First of all in the detailed models coalescence and break-up should be incorporated. For both models this a sub-grid scale model is needed to resolve

the pressure and momentum equations between two interfaces. In addition to this, *Front Tracking* would need, an algorithm for interface mesh reconstruction. *VoF* will need a algorithm to allow more than one interface within a control volume. For the *DBM* model new elements could be incorporation of bubble induced turbulence, embedding an algorithm for bubbles with a diameter exceeding the cell spacing and the incorporation of closure relations that are valid in dense bubble swarms.

samenvatting

Inleiding

In veel (bio-)chemische en metallurgische processen speelt het contact tussen gassen en vloeistoffen een belangrijke rol. Een apparaat dat hier vaak voor wordt gebruikt is de bellenkolom. Bellenkolommen zijn met name geschikt de vloeistoffase goed gemengd is waardoor een goede warmte- en stofoverdracht plaatsvindt. Ondanks hun frequente toepassing is de fundamentele kennis over het dynamische gedrag van bellenkolommen nog steeds beperkt. Het ontwerp en het gebruik van deze apparaten is gebaseerd op een groot aantal empirische correlaties en het opschalen of verkleinen is mede hierdoor niet eenvoudig. In dit proefschrift zijn een aantal numerieke modellen ontwikkeld, verbeterd en gevalideerd, die kunnen helpen om een meer gedetailleerd beeld van de belangrijkste fenomenen te krijgen.

Modellering

Met behulp van drie verschillende modellen is onderzoek gedaan op twee verschillende detail niveaus (zowel lengte als tijd). De twee meest gedetailleerde modellen beschrijven de verplaatsing van het gas-vloeistof oppervlak en rekenen voor zowel de gas- als de vloeistoffase de druk en het snelheidsveld uit. Met deze modellen is de dynamica van gasbellen op het niveau van een enkele bel bestudeerd. Het eerste model gebruikt een *Front Tracking* methode die is ontwikkeld door Unverdi and Tryggvason (1992). Het tweede model gebruikt een *Volume of Fluid*(*VoF*) methode van Youngs (1982, 1987).

Het *Front Tracking* model is op de volgende punten verbeterd:

- de pressure Poisson vergelijking wordt opgelost met een andere strategie waardoor het mogelijk is dichtheidsverschillen tot een ratio van $\rho_l/\rho_g = 10000$ te modelleren.
- het algoritme waarmee de oppervlaktespanning wordt uitgerekend is vernieuwd en vereenvoudigd.
- een re-triangulatie methode is geïntroduceerd. Hiermee kan de totale oppervlakte energie worden teruggebracht.
- ter voorkoming van fouten in het re-meshen zijn nieuwe re-meshing methoden geïntroduceerd.
- de locale viscositeit wordt berekend door middel van een harmonische middeling van de kinematische viscositeit. (Prosperetti, 2001)

Het *VoF* model is op de volgende punten verbeterd:

- er is een nieuwe methode ontwikkeld om de oppervlaktespanning uit te rekenen. Deze is gebaseerd op de trekkracht tussen twee naast elkaar liggende oppervlakte elementen
- de kleurfunctie is ge-smoothed. Dit heeft ertoe geleid dat het oplossen van de Pressure Poisson vergelijking (PPE) eenvoudiger is en dat de oriëntatie van de oppervlakte-elementen beter wordt voorspeld.
- er is een correctie term ingevoerd die de fouten in de flux corrigeert.

Een tweede, minder gedetailleerd niveau, is gemodelleerd met een Euler-Langrangiaanse methode. Het Discreet Bellen Model (*DBM*), beschrijft de stroming van de gas- en vloeistoffase in de gehele bellenkolom. Hierbij worden alle gasbellen afzonderlijk gevolgd. Het aantal bellen dat tegelijk gevolgd wordt ligt in de orde van 10^5 bellen. De verplaatsing van de bellen wordt berekend door toepassing van de bewegingswetten van Newton. De krachten die op de bellen werken worden bepaald met behulp van sluitingsrelaties. Het model berekent 'two-way coupling' en houdt rekening met het belvolume. Het *DBM* model, dat oorspronkelijk door Rudman (1998) is ontwikkeld, is verfijnd op de volgende punten:

- de introductie van moderne sluitingsrelaties.

- een tweede orde accuraat Barton discretisatie schema voor de flux.
- een LES turbulentie model,
- en een volledig drie dimensionaal botsing algoritme.

Resultaten

De twee gedetailleerde modellen zijn in een computerprogramma geprogrammeerd en alle onderdelen van deze programma's zijn onafhankelijk getest. Met dit computerprogramma zijn simulaties uitgevoerd, die zijn vergeleken met experimentele data uit de literatuur. De bel vorm en dynamica zijn kwalitatief vergeleken met de gegevens uit het bellen diagram van Grace (1973) en komen daarmee goed overeen. De terminal stijgsnelheden, die door de modellen werden voorspeld, zijn vergeleken met waarden verkregen met behulp van sluitingsrelaties uit Clift et al. (1978). Ook hier geven beide modellen vergelijkbare en redelijk betrouwbare resultaten. Ondanks dat een aantal verschillen zijn aan te wijzen in de details van de simulatieresultaten, is geen van beide modellen meer of minder accuraat dan de ander.

De aanpassingen aan het *DBM* model hebben aanzienlijke verbeteringen laten zien. Door gebruik te maken van het botsings algoritme, kunnen nu gasfracties tot 40% worden gesimuleerd. De toevoeging van het Barton schema had weinig invloed op de dynamica van de bellenkolom. Het LES model verlaagde de gemiddelde vloeistofsnelheid, zoals verwacht. De nieuwe sluitingsrelaties hadden tot gevolg dat de bellen op een andere manier over de kolom verdeeld werden. Vergelijking van de simulaties met experimentele data, die met *Particle Image Velocimetry* zijn verkregen laten een redelijk overeenstemming zien.

Vooruitblik

In toekomstig onderzoek kunnen een aantal nieuwe elementen worden onderzocht. In de gedetailleerde modellen zou coalescentie en break-up kunnen worden toegevoegd. Voor beide modellen is hiervoor een sub-grid model nodig om de druk en impuls vergelijkingen op te lossen. *Front Tracking* zou

als extra nog een extra re-meshing algoritme nodig hebben. In *VoF* zou een mogelijkheid moeten worden gezocht om meerdere interfaces in een cel te construeren. Het *DBM* zou kan worden verbeterd door de introductie van een model voor bel geïnduceerde turbulentie, een methode om bellen te behandelen die groter zijn dan een cel en het toevoegen van sluitingsrelaties die gelden bij hoge gasfracties.

Contents

1 Introduction **1**

1.1 Introduction 1

1.2 Bubble columns 2

1.3 Mathematical models 3

1.4 Experimental validation 3

1.4.1 Single bubble experiments 4

1.4.2 Bubble plume experiments 4

1.5 This thesis 5

2 Modelling single gas bubble behaviour using a Front Tracking model **7**

2.1 Introduction 8

2.2 Model description 10

2.2.1 Flow problem 10

2.2.2 Interface grid 12

2.2.3 Surface tension force 14

2.2.4 Restructuring of the interface mesh 16

2.3 Numerical method 22

2.4 Model verification 23

2.4.1 Number of surface elements 24

2.4.2 Grid size of the Eulerian mesh 24
2.4.3 Surface tension model verification 25
2.4.4 Interface viscosity interpolation 27
2.4.5 Standard advection test 29
2.4.6 Stability test 30
2.4.7 Energy minimalisation 30
2.5 Conclusion 32
2.5.1 Verification 34
2.6 Acknowledgements 35

3 Modelling single gas bubble behaviour using the Volume of Fluid method 37
3.1 Introduction 38
3.2 Model equations 41
3.2.1 Flow problem 41
3.2.2 Interface reconstruction and flux calculations 42
3.2.3 Treatment of the discontinuety at the interface 46
3.2.4 Surface tension force 48
3.3 Numerical method 54
3.4 Model verification 56
3.4.1 Influence of the Eulerian grid size 56
3.4.2 Standard advection test 57
3.4.3 Model stability test 58
3.4.4 Verification of surface tension force model: prediction of the interior excess pressure of a spherical bubble . . 61
3.5 Conclusions 63

4 Comparison of detailed models to experimental data 65

4.1 Introduction 67
4.2 Detailed models versus reported experiments 67
4.2.1 Bubble shape and dimensionless numbers 67
4.2.2 Correlations for the terminal rise velocity 68
4.2.3 Simulation results 71
4.2.4 Spherical bubbles 71
4.2.5 Ellipsoidal/Wobbling bubbles 74
4.2.6 Discussion 75
4.3 Ultra sound versus simulations 78
4.3.1 Introduction 78
4.3.2 Experimental method 78
4.3.3 Experimental data 79
4.3.4 Simulation results 81
4.3.5 Discussion 82
4.4 Conclusion 83

5 Discrete bubble modelling **85**
5.1 Introduction 86
5.2 Model equations 88
5.2.1 Liquid phase hydrodynamics 88
5.2.2 Bubble dynamics 90
5.2.3 Direct bubble-bubble interaction 93
5.3 Numerical method 95
5.4 Experimental set-up 96
5.5 Model verification 98
5.5.1 Comparison to experimental results. 111
5.6 Concluding remarks 111

5.7 Acknowledgements 112

6 Conclusion and outlook **113**

6.1 Conclusions: Detailed models 113

6.1.1 Comparison of the models 115

6.2 Conclusions: Discrete Bubble Models 116

6.3 Outlook: detailed models 116

6.3.1 Single bubble systems 116

6.3.2 Multiple bubble systems 117

6.3.3 Discussion 120

6.4 Outlook: Discrete Bubble Modelling 121

6.4.1 Code optimisation and speed-up of the simulations . . 122

6.4.2 Final remarks 122

A Interface reconstruction in 3D-VOF **125**

A.1 Introduction 125

A.2 Determination of the surface element type 125

A.3 Calculation of the fluxes 126

B Translation **139**

B.1 Forward translation 139

B.2 Backward translation of fluxes 140

B.3 Backward translation of the tangent vectors 141

B.3.1 Translation to original axis 141

B.3.2 Swapping the back and front. 141

C Results for the parameter study with the Front Tracking model **145**

D Results for the parameter study with the Volume of Fluid model 153

E Smoothing with an integrated Peskin function 159

Curriculum Vitae 171

Dankwoord 173

Chapter 1

Introduction

1.1 Introduction

Bubbles rising in liquids have widespread applications. A well known example of an apparatus in which this is encountered, is the bubble column. These apparatus can be found in a wide range of process industries varying from waste water treatment to various chemical processes. Bubble columns are easy to construct and maintain because they do not include any mechanical parts. Bubble columns have good heat and mass transfer characteristics due to the very high mixing induced by the rising bubbles. A special class of bubble columns can be found in metallurgical industry. Where in (bio-)chemical reaction engineering intense gas-liquid contact is the main objective, in metallurgic processes rising bubbles are also applied to force a fluid velocity in a specified direction.

To understand the importance of the parameters that influence the behaviour of single bubbles, bubble plumes or the complete bubble column including the liquid phase, numerous research projects have been (and still are being) conducted. Experimental work has resulted in a wide variety of empirical correlations that predict the dynamics of bubble columns, giving direction to the design of currently applied devices. Recent developments in computer speed open up the opportunity to develop detailed numerical models that can be applied to study the importance of the proposed parameters. Once these mathematical models are validated against analytical solutions and experi-

mental data, they can help to predict the dynamic flow behaviour of bubble columns. This is of special interest to those who want do design or operate bubble columns that are hard to handle in experiments e.g. hazardous gasses or liquids or liquid metals. A great advantage of computational models over experimental work is the ease at which physical and geometrical parameters can be modified towards optimisation: numerical experiments are increasingly accepted as a substitute for expensive, hazardous and time consuming laboratory programs.

Computational models can not include all scales (levels of details) simultaniously. Models that describe the phenomena in more detail generally consume more computer capacity. The models in the present study operate on two levels: either on the scale of one bubble or on the scale of a laboratory size bubble column. The latter models describe the phenomena in less detail and can be used to compute larger systems within a reasonable time. However, they do not include the dynamics on bubble scale e.g. interface deformation. To account in some way for details that are not resolved, so-called closure relations are needed. Closure relations describe the independent forces acting on each bubble.

The more detailed models, evaluating the dynamic behaviour of a single, or a few bubbles and its surrounding liquid, can be used to check or even develop closure relations required in the less detailed models.

To validate the above mentioned mathematical models, the results of simulations run with these models were compared to experimental work from own measurements, using an Particle Image Velocimetry method and an ultra sound method. The results have also been compared to experimental data reported in literature.

1.2 Bubble columns

Bubble columns can be operated in several regimes. If relative low gas fluxes are applied, the columns operate in the *homogeneous regime*: small bubbles of about equal size are uniformly distributed throughout the column, the bubble velocity is below 0.3 m/s approximately. If higher gas fluxes are applied the *heterogeneous regime* is entered. In this regime a wide range of bubble diameters develop, breaks up and coalesce, the flow is unstable and is

dominated by the larger bubbles. At even higher gas fluxes, the gas bubbles grow so large that they occupy the whole width of the column resulting in an alternation of liquid phase and gas phase passing through the column. These alternating phases are called 'slugs'. Therefore, this regime is called the *slug flow* regime. In this study only the first two regimes will be looked at.

1.3 Mathematical models

Over the last fifty years a number of approaches to fluid dynamics have been developed. Starting off from one fluid model, it was tried to model two fluid flows by multi fluid models in which the two (or more) phases are seen as inter-penetrating liquids, the so called "Euler-Euler" or multi-fluid models.

A more detailed approach is found in the Euler-Lagrangian models. In these models the discrete elements (bubbles and/or particles) are traced individually by Newtonian laws of motion. These models are also known as Discrete Bubble Models (DBM) (Delnoij, 1999) or Discrete Particle Models (Hoomans, 2000).

A third even more detailed model is the class in which the flow field inside and outside a bubble, the shape of the bubble and the interface dynamics are evaluated in detail. Examples of models that can perform these kind of computations are *Volume of Fluid*(*VoF*), *Front Tracking* and *Level-Set*. On even lower levels one could do Direct Numerical Simulation (DNS) or Lattice Bolzman type of modelling.

In this thesis we focus in the *VoF*, *Front Tracking* and *DBM*. A final objective, in combining these two levels of detail is that the outcome of the *Front Tracking* and *VoF* models can be used as input for *DBM*. For example, closure relations derived using one of the detailed models could be applied in *DBM*.

1.4 Experimental validation

Validation of mathematical models was done by comparing the simulation results to experimental data. Since a wide range of experimental data has been reported in literature, only a few specialised experiments will be showed

here.

In two different experimental setups a number of bubble column experiments have been carried out. Two kinds of experiments can be distinguished.

- single bubble experiments
- bubble plume experiments

The single bubble experiments were done at the metallurgical laboratory at *CORUS RD&T, The Netherlands*, involving liquid metals and using an ultrasound technique. The other experiments were done at the laboratory of the department of Chemical Engineering at Aalborg University in Esbjerg (Denmark) using a dual camera Particle Image Velocimetry technique. The latter experiments concerned plumes of air bubbles rising in water.

1.4.1 Single bubble experiments

In the range where no experimental data could be found in the literature, specialised experiments were conducted to validate the detailed models. The technique used to obtain this data is highly dependent on the liquid used. Liquid metals such as liquid aluminium and liquid raw iron are hard to handle because of the high temperatures involved. During this project *CORUS-RD&T* developed an ultra-sound measurement technique that is capable of detecting and following the position of a bubble interface in those materials.

1.4.2 Bubble plume experiments

The simulations run with the *DBM* are also compared to experiments. A bubble plume was released through 49 nozzles in the bottom plate of a rectangular column. *Particle Image Velocimetry* (*PIV*) was used to measure the liquid flow in the vicinity of the plume. *PIV* was also applied to measure the motion of the gas bubbles themselves.

1.5 This thesis

In this study three mathematical models were developed and validated. In chapter 2 and 3 development of a *Front Tracking* and a *Volume of Fluid*(*VoF*) model are described. The governing equations will be given followed by a description of the numerical implementation. Test of the newly incorporated algorithms will be presented.

In chapter 4 simulation results from the *Front Tracking* model and the *VoF* model are compared to a wide range of experimental data reported in the literature and experimental data on argon bubbles rising in liquid aluminium are considered. Both the *Front Tracking* model and the *VoF* model were applied to determine their operating windows. The results of a number of simulations, from both models, will be shown and compared to data from literature. Measurements conducted with the ultrasound method will be explained and the resulting data will be compared with simulation results for the liquid-alumina system. Finally, the differences between the models will be discussed.

In chapter 5 improvements to the *Discrete Bubble Model* originally developed by Delnoij (1999) are described. The impact of the improvements will be shown as well as a comparison of the improved model to *PIV* measurements in water-air bubble columns.

In chapter 6, the conclusions of the previous chapters will be summarised and an outlook to potential areas of development will be given.

Chapter 2

Modelling single gas bubble behaviour using a Front Tracking model

Abstract

To model complex multi-fluid flows Unverdi and Tryggvason (1992) introduced a *Front Tracking* method, where they combined the capabilities of both *Marker and Cell methods (MAC)* (Harlow and Welch, 1965) and *Volume of Fluid methods* (*VoF*) (Nichols and Hirt, 1971), (Youngs, 1982) methods. In *Front Tracking* methods an unstructured dynamic mesh is used to represent the surface separating the two fluids (e.g. two different liquids or a liquid and a gas). A one-field continuum approach is used to describe the velocity fields of both fluids using an indicator function obtained from the position of the interface-mesh, to compute the phase fractions. The Navier-Stokes equations are solved on a fixed (Eulerian) grid.

In the present study, the front tracking method originally developed by Tryggvason et al. (2001) has been modified by: applying a non-conservative form of the Navier-Stokes equations enabling us to handle flow problems with very large density ratios, an improved version of the Peskin smoothing function, a different and more direct approach to calculate the surface tension force and finally a new method for restructuring the interface mesh by minimisation of

the surface energy.

The need for these improvements originated from the main objective of this study, e.g. modelling gas-liquid flows with a high density ration and a high surface tension, as encounterd in the processing of e.g. liquid metals. Our *Front Tracking* method can solve these problems with density ratio as high as $\frac{\rho_l}{\rho_g} = 10^4$, provided that the number of Eulerian cells within the bubble (in each direction) is about 20 to avoid significant losses of gas volume. Furthermore, the product of the surface tension (σ) and the curvature (κ) should not exceed 800 Pa to avoid the development of parasitic currents. Finally simulation of bubbles with a large bubble diameter ($d_{eq} = 0.05\ m$) will require additional criteria to perform appropriate re-meshing the surface.

2.1 Introduction

Bubble columns are widely applied in chemical, biological, petrochemical and metallurgical industries. Typical applications are encountered in processes involving, among others, absorption, coal liquification and liquid metal refining. Bubble columns can be constructed with relative ease, have good heat transfer characteristics and good mixing properties. In metallurgical processes gas jets are applied in some cases to achieve mixing of liquid metals. In the chemical industry mixing of fluids is commonly achieved using impellers, however, these cannot be used in metallurgical processes because of the high prevailing process temperatures (e.g. melting point of iron : 1808.15 K). Despite the widespread application of bubble columns, fundamental knowledge on the fluid mechanical behaviour is still lacking and therefore the dynamic behaviour is not fully understood.

Modelling bubble columns using different approaches and different strategies can provide this kind of knowledge while the important phenomena can be studied in detail. Industrial scale bubble columns are frequently simulated using Euler-Euler models. These models describe the two phases as inter-penetrating fluids. Euler-Euler models do not capture the complex phenomena on the scale of the bubbles, and bubble-liquid interactions are taken into account via empirical closure relations. Often these closure relations have been obtained from studies on single bubbles of spherical shape rising in quiescent liquids. More complex systems have proven difficult to study

because of experimental limitations. Therefor very little is known about the behaviour of swarms of bubbles rising in clusters and their impact on the overall flow patterns. Another example is the interaction between large and small bubbles and their interaction with the liquid phase.

Detailed multi-phase flow models, like *Front Tracking* and *Volume of Fluid* (*VoF*) models can be used to evaluate and derive closure relations for drag, lift and virtual mass forces, in more complex flows. For example Tomiyama et al. (1995) reported some computational experiments to determine the lift force acting on gas bubbles rising in linear shear fields using a modified *SOLA-VoF* method. The numerical studies of Tomiyama (1998), Esmaeeli and Tryggvason (1998) and Esmaeeli and Tryggvason (1999) give a good indication of what can be achieved with these models.

In the present study a full three dimensional *Front Tracking* model was developed, that can be used to carry out the same kind of computational experiments. A *Front Tracking* method was chosen because of its excellent capability to calculate the surface tension forces, which significantly effects the bubble shape and dynamics. Other methods, like the classical *VoF*, *level set* and *MAC* models, do not allow for such an accurate and detailed representation of the surface tension forces. At present most of these models use the *Continuum Surface Force*-model (*CSF*) first proposed by Brackbill et al. (1992) and encounter problems to accurately evaluate the curvature of the bubble interface. This, however, could lead to a misprediction of the interface behaviour, resulting in a wrong bubble shape.

A disadvantage of the *Front Tracking* method is however, that the volume of the bubble is not intrinsically exactly conserved. The gas volume of the bubble slowly changes in time, caused by the method used to move the interface, the applied filters and the re-meshing of the interface mesh. The markers that span the surface elements are moved with their local velocities. These local marker velocities are interpolated from the velocity field on the Eulerian grid. These interpolated velocities introduce minor small-scale anisotropy (Unverdi and Tryggvason, 1992). By using a finer computational grid this problem can however effectively be suppressed.

This chapter starts off with a description of the model equations, followed by details on the numerical implementation of our front tracking method. Subsequently a model verification is carried out to demonstrate the capabilities of the model especially to asses the performance of the new elements added

in the method. Special attention is given to the conservation of mass, the interior gas bubble pressure, and the bubble shape. In Chapter 4 the capabilities of the model to predict the bubble shape and its terminal rise velocity are investigated. Also a comparison between the *Front Tracking* model with the *VoF* model and experimental data will be reported in that chapter.

2.2 Model description

In this section the mathematical formulation of the model will be explained. Every subsection covers one part of the model. The numerical implementation is given in the next section.

2.2.1 Flow problem

The equations governing the unsteady motion of two immisable viscous liquids are given by the Navier-Stokes equations (equation 2.1). We use a one fluid approach with local density and viscosity variation to account for the separate phases. Because of this one fluid approach only three momentum equations (to calculate the velocities in three dimensions) have to be solved,

$$\frac{\partial \rho \mathbf{u}}{\partial t} + \nabla \cdot \rho \mathbf{u}\mathbf{u} = -\nabla p + \nabla \cdot \mu \left((\nabla \mathbf{u}) + (\nabla \mathbf{u})^T \right) + \rho \mathbf{g} + \mathbf{F_{st}} \tag{2.1}$$

where $\mathbf{u}$ is the fluid velocity field, p the local pressure and ρ and μ represent the local density and viscosity, respectively. $\mathbf{F_{st}}$ is the volumetric surface tension force which only acts in the vicinity of the interface.

The Navier-Stokes equations are supplemented by the continuity equation for incompressible flow:

$$\nabla \cdot \mathbf{u} = 0 \tag{2.2}$$

and the equations of state for the density (equation 2.4) and viscosity (equations 2.5 or 2.6).

An indicator function $f(\mathbf{x})$ is used to indicate the local liquid fraction at position $\mathbf{x}$ and time t. $f(\mathbf{x}) = 1$ corresponds to the presence of the liquid

phase only and $f(\mathbf{x}) = 0$ to the presence of the gas phase only. In the *Front Tracking*-model it is assumed that this indicator function is conserved (travelling along its path, with the local velocity, the volume of a fluid element remains constant):

$$\frac{Df(\mathbf{x})}{Dt} = 0 \tag{2.3}$$

However, in the *Front Tracking* method this conservation equation, which is based on the assumption of incompressibility of both the liquid and the gas phase, is not solved directly. The indicator function is evaluated from the position of the interface(mesh) that is moved every time step.

From the $f(\mathbf{x})$ the local density is evaluated as:

$$\rho = f(\mathbf{x}) \cdot \rho_l + (1 - f(\mathbf{x}))\,\rho_g = f(\mathbf{x})\,(\rho_l - \rho_g) + \rho_g \tag{2.4}$$

For the evaluation of the local viscosity several different approaches have been proposed. Often (e.g. Unverdi and Tryggvason (1992) and Rudman (1998)) a simple linear weighing is used:

$$\mu = f(\mathbf{x})\,(\mu_l - \mu_g) + \mu_g \tag{2.5}$$

Another approach was recently proposed by Prosperetti (2001). Based on a detailed mathematical derivation Prosperetti showed that the momentum transfer along the gas-liquid interface can be considered analogously to an electrical current passing through two parallel resistances. Considering the flow along an interface: In absence of normal viscous stresses and surface tension forces, the pressure difference (analogue of voltage) along the interface is equal on both sides of the interface, so that the two fluid streams (analogous to currents) flow in parallel along the interface under the action of the same pressure gradient. Thus the total resistance is a combination of two resistances in parallel, which results in:

$$\frac{\rho}{\mu} = f(\mathbf{x}) \left(\frac{\rho_l}{\mu_l} - \frac{\rho_g}{\mu_g} \right) + \frac{\rho_g}{\mu_g} \tag{2.6}$$

The evaluation of the surface tension force will be explained in section 2.2.3.

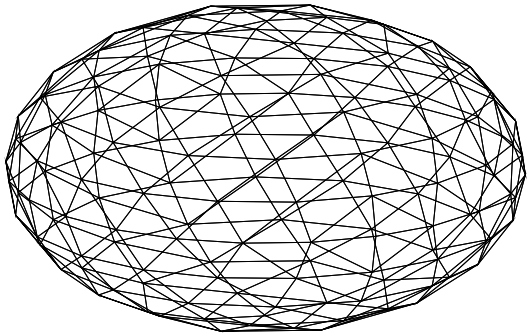

Figure 2.1: Example of an interface mesh.

2.2.2 Interface grid

To indicate the location of the interface, an unstructured mesh is generated at the interface. The interface mesh consists of triangles that are connected to each other and form a continuous surface (see e.g. figure 2.1). From this mesh the indicator function $f(\mathbf{x})$, on the Cartesian grid, is computed, which is used in the evaluation of the local fluid properties needed to solve the Navier-Stokes equations.

Once the flow field has been computed all the verticil of every triangular surface element are moved with the local interpolated fluid velocity. This results in a different shape of the bubble surface. By moving the verticil the triangular surface elements become stretched. If an element becomes too large, becomes too small or if its shape is deviating too far from that of an equally sided triangle, then the surface elements are deleted or added to adjust their shape. Two points need special attention, firstly the displacement of the verticil of each triangle and secondly the calculation of the value of the indicator function. They will be discussed subsequently in more detail.

Displacement of the verticil

In the code two algorithms for moving the verticil have been programmed. The first algorithm uses an 8 point stencil and the second one uses 64 grid

points that are within a $2h$ radius of the vertex considered, h being the Eulerian grid spacing.

The first algorithm is a simple volume weighed average of the velocity in the eight surrounding grid points on the Eulerian staggered mesh. Because the components of the velocity are not located at the same spatial coordinate of the staggered grid, for each direction eight different grid points are taken into account.

The second algorithm uses a numerical approximation of the Dirac-δ function indicated by $D(\mathbf{x} - \tilde{\mathbf{x}})$, where $\tilde{\mathbf{x}}$ is the coordinate of the vertex and $\mathbf{x}$ are the coordinates of the nodes where the velocities on the staggered Cartesian mesh are available.

$$\mathbf{u}^l = \sum_i D(\mathbf{x} - \tilde{\mathbf{x}})\, \mathbf{u}_i \tag{2.7}$$

Using this interpolation method every component of the velocity is calculated using a $(2n)^3$ points stencil, where $n = 2$ is commonly used. The δ-function used in the model is an integrated form of the Peskin function (Trapp and Mortensen, 1993). Details on this integrated version of the Peskin function can be found in appendix E.

Evaluation of the indicator function

For solving the Navier-Stokes equations information is needed on the local density and viscosity in the Eulerian domain. These properties are evaluated using equation 2.4 and equation 2.6 respectively. The problem focuses on the evaluation of the indicator function $f(\mathbf{x})$. In *Front Tracking* the value is calculated from the interface information. The method used by Unverdi and Tryggvason (1992) is also applied here. A function $\mathbf{G}(\mathbf{x})$ is evaluated using

$$\mathbf{G}(\mathbf{x}) = \sum_l D(\mathbf{x} - \tilde{\mathbf{x}}_\mathbf{l})\, \mathbf{n}_\mathbf{l} \Delta s_l \tag{2.8}$$

where $\mathbf{n_l}$ is the outwardly pointing normal on interface element l, Δs is the surface area of this element. The function $\mathbf{G}(\mathbf{x})$ is a vector that contains the value of $\nabla f(\mathbf{x})$. The $f(\mathbf{x})$ values could be computed from $\mathbf{G}(\mathbf{x})$, starting

in a cell where $f(\mathbf{x})$ is known (e.g. at the boundary) and evaluate $f(\mathbf{x})$ in the other cells by moving around and adding the value of $\mathbf{G}(\mathbf{x})$. The path along the cells is arbitrary but could result in slightly different values for certain grid cells depending on the selected path. An elegant way to overcome this problem is via numerical differentiation. Using a second order accurate centred difference the divergence $(\nabla \cdot \mathbf{G})$ is calculated, thus calculating the Laplacian of the indicator function, which is zero except near the interfaces. To find the indicator function equation 2.9 is solved using an ICCG solver.

$$\nabla^2 f = \nabla \cdot \mathbf{G} \tag{2.9}$$

Solving equation 2.9 in this manner gives minor undershoots and overshoots in $f(\mathbf{x})$ near the interface and therefore minor filtering is applied.

2.2.3 Surface tension force

The accurate calculation of the curvature of the interface is one of the main advantages of the *Front Tracking* model. In this work a new approach is adopted that is much easier to implement than the one used by Tryggvason et al. (1998). In both approaches the $\partial \mathbf{F_e}$ force acting on a surface element must be calculated.

$$\partial \mathbf{F_e} = \int_{\partial A} \sigma \kappa \mathbf{n} dA \tag{2.10}$$

The definition of the curvature $\kappa \mathbf{n} = (\mathbf{n} \times \nabla) \times \mathbf{n}$ is used to rewrite this equation into

$$\partial F_e = \sigma \int_{\partial A} \kappa \mathbf{n} dA = \sigma \int_{\partial A} (\mathbf{n} \times \nabla) \times \mathbf{n} dA = \sigma \oint_s (\mathbf{t} \times \mathbf{n})\, ds \tag{2.11}$$

where $\mathbf{t}$ is the counter clockwise unit tangent vector along the edges of the element and s is the length of these tangent vectors. Tryggvason et al. (1998) and Tryggvason (1999) construct a second order polynomial to compute the length of the (curved) edge and compute $(\mathbf{t} \times \mathbf{n})$ from the divergence of this polynomial. In this work the cross product of $\mathbf{t}$ and $\mathbf{n}$ on the adjacent

surface elements is calculated directly (see figure 2.2). Using this method the construction of the polynomial can be avoided. Furthermore, the normal to all the interfaces has already been calculated and the tangent vectors can easily be constructed from the coordinates of the verticil of a surface element. The amount of computational work needed to calculate the surface tension force with this method is considerably less than a method using a polynomial. The calculation results in three pull forces acting on the edges of each element. Once the forces on all the edges of all triangles are known, the forces acting at the position of the nodes of the staggered Cartesian grid are then computed using:

$$(\mathbf{F}_{st})_{i,j,k} = \sum D\left(\mathbf{x} - \tilde{\mathbf{x}}\right) \partial \mathbf{F}_e \tag{2.12}$$

where $D\left(\mathbf{x} - \tilde{\mathbf{x}}\right)$ is again a smooth δ-function, for which the integrated Peskin-function is used.

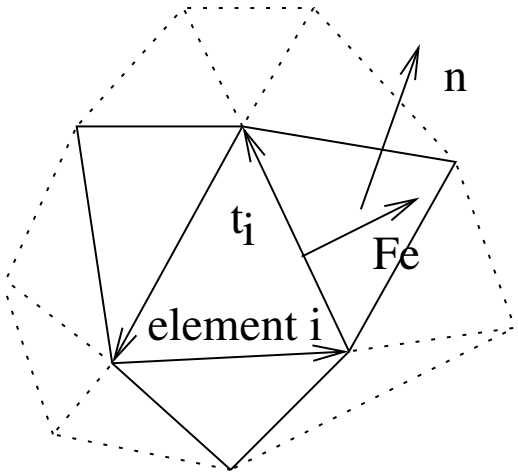

Figure 2.2: Schematic representation of the calculation of the surface tension force on element i using the tangent $\mathbf{t}_i$ and the normal $\mathbf{n}_j$.

Since the surface tension force is only dependent on the length of the edge ($|\mathbf{t}|$) and the constant surface tension σ, the two forces that act on the common edge of two adjacent elements are always exactly equal and have only a different direction. Therefore there is no need to average these two forces, as was done by Tryggvason (1999).

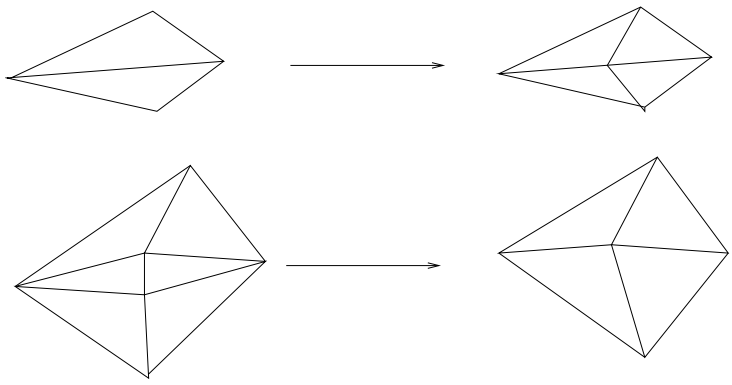

Figure 2.3: Addition or removal of interface elements.

2.2.4 Restructuring of the interface mesh

When the surface of the bubble is moved, the surface mesh deforms. For example, when a bubble rises through a liquid, the liquid surrounding this bubble moves downwards. Also the flow inside the bubble near the interface is directed downwards. Due to this flow pattern the elements on the top of the bubble become stretched,, while the elements at the bottom of the bubble shrink. The surface resolution at the top would eventually become low, resulting in a less accurate description of the surface, while the resolution at the bottom would become (unnecessary) high. Furthermore, a large number of surface elements within the size of the Cartesian grid can also have an adverse effect on the surface description, because the verticil are all moved with an interpolated velocity that is not necessarily divergence free. Stretching and shrinking of the surface elements could cause numerical problems after some simulation time if too many elements are used.

In their codes Tryggvason (1999) uses a number of techniques to restructure the surface mesh. Most of these were adopted in our study. The most evident restructuring is the addition or removal of new surface elements if one of the edges of an element becomes too long or too short. This process is illustrated in figure 2.3 below.

A couple of elements is removed if their common edge is becoming too short (e.g. edge length less than $0.3h$). A new point is placed in between the two verticil at the end of the short edge. Curvature is not taken into account

because the merical errors introduced will be very small if the edge is small enough.

If the edge between two adjacent elements becomes too large (e.g. edge length exceeding $1.7h$), then the two elements are split into four surface elements. The needed new vertex is positioned in the middle of the long edge.

Rare cases

By applying this addition and removal of elements, in very rare cases an interface mesh can develop artifacts. The most simple case of such an artifact is that two elements become connected twice to each other as if they are standing back to back. Since the volume between these elements is 0, they do not influence the indicator function $f(\mathbf{x})$, but because the angle between these faces is 2π the surface tension force introduced by this pair is very large. In this work, the two mesh elements are removed and the two elements that are connected to either one of these artifact-elements are reconnected to each other.

An other even more rare artifact as shown in figure 2.4 can develop. This could become troublesome if, in a later stadium, an interface element closes the gap that exist between the points 1-3-5. When this occures this could result in a situation where four interface elements are connected to two points along the same edge. As long as no further addition or removal of these elements takes place there is no problem, but when one set is deleted the common point with the other set of elements is deleted which will give rise to numerical problems. To avoid this problem, two additional points are inserted and the element pairs are rearranged resulting in a pair C-D and F-B. By introducing two new points for one of those pairs at the position of point 3 and 5 the mesh is computationally broken in two parts. Since the two new points and the points 3 and 5 respectively are located at exactly the same coordinate, they will always be translated with the same local velocity. If one of the element pairs C-D of F-B is deleted the mesh will be broken in two parts. This however, is still just a computational break-up without any physical meaning, but it gives a good starting point for incorporating bubble break-up in *Front Tracking*-codes. The results of such a rearrangement is shown in figure 2.5. Recently Shin and Juric (2002) reported the use of an mesh without connectivity where this kind of problems can be avoided.

Their method generates a new mesh over the level contour $f(\mathbf{x}) = 0.5$, once every n time steps. They claim that their method can handle the break-up of bubbles and coalescence of bubbles but without including a physical model for these phenomena.

Energy minimalisation

In addition to this addition and removal of surface elements also the total surface energy is minimised. This technique was taken from van Damme and Alboul (1995). The idea behind this minimisation technique is that if the total energy, that is related to the total curvature, of the surface is minimised, also the interface area is minimised. This results in a nicely smooth interface. The total surface energy is defined by equation 2.13

$$E = \sum_{\forall j} \sum_{i} \alpha_i \, l_i \tag{2.13}$$

with j being the surface element number, i the edge number, α the angle between normal vectors of two adjacent surface elements and l the length of the edge joined by the two elements.

For every edge it is tried whether the energy of the total system decreases if two adjacent elements are flipped as shown in figure 2.6. Only the topology of the interface elements is changed. The marker points that span the interface elements remain unaltered during this operation.

Figure 2.7 was taken from van Damme and Alboul (1995) and shows the Schwartz's polyhedral 'cylinder' (figure 2.7(a)). This is a typical example of a bad triangulation. In figure 2.7(b) the same 'cylinder' is shown after applying the minimalisation algorithm.

In the case of *Front Tracking* the local minimalisation of the local curvature has a beneficial effect on the local surface tension force. By decreasing the local curvature, also the local surface tension is decreased.

Since this is a very costly operation, it is performed only once every n time steps where n typically equals 1000.

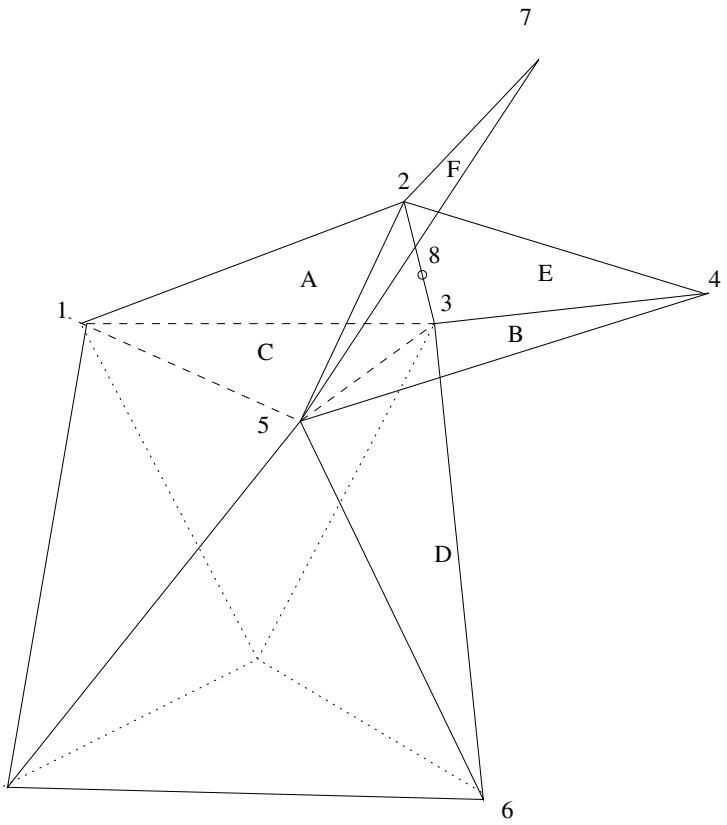

Figure 2.4: Extreme interface problem. Element A is connected to the points 1-2-3, B to 3-4-5, C to 1-2-5, D to 3-5-6, E to 2-3-4 and F to 2-5 and 7. When the edge 2-3 becomes too short, the elements A and E are deleted, points 2 and 3 put to one new point 8 in between 2 and 3. The elements pairs D-B and C-F share edge 8-5 but are not connected to each other. This could lead to problems in further mesh restructuring.

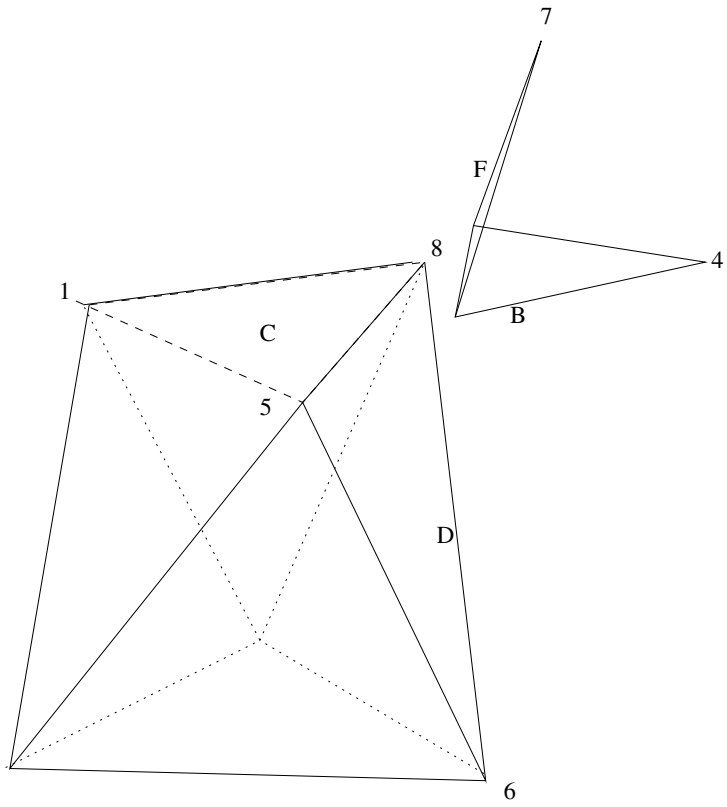

Figure 2.5: Extreme interface problem: Mesh after recombination. The element pairs C-D and F-B which used to have edge 3-8 as a joining edge have now become detached.

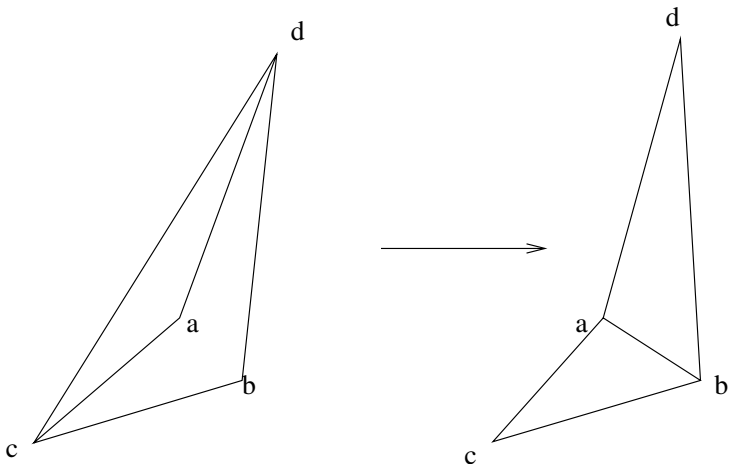

Figure 2.6: Element flip.

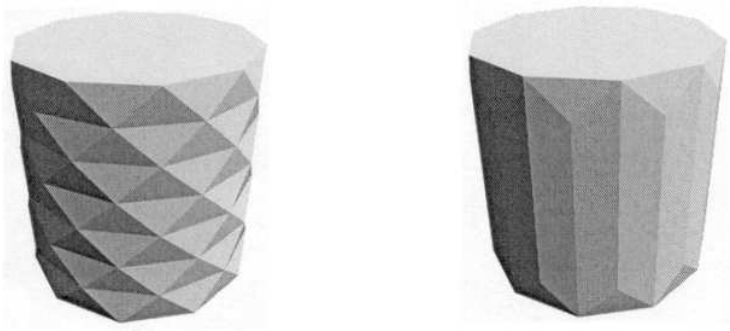

Figure 2.7: Schwartz's polyhedral 'cylinder' before (a) and after (b) applying the minimalisation algorithm. Figures were taken from van Damme and Aboul (1995).

2.3 Numerical method

In figure 2.8 a schematic overview of the computational steps in our computer code is given.

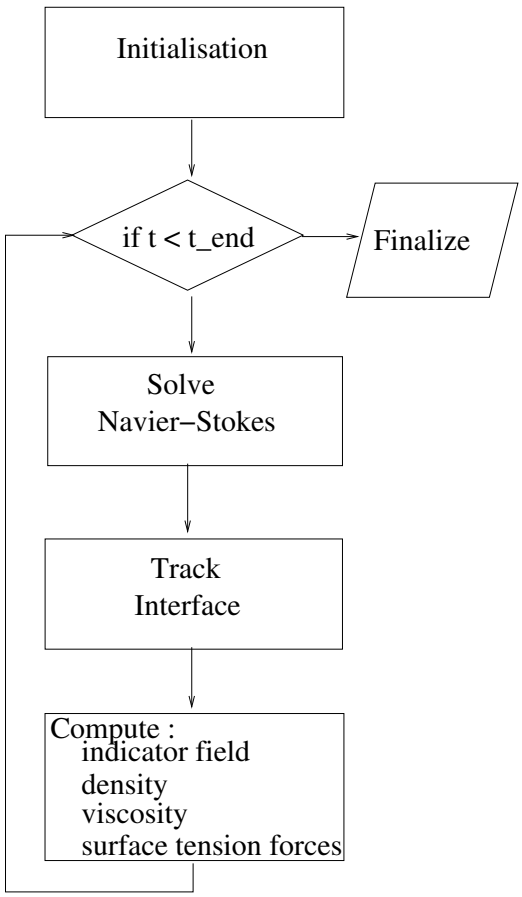

Figure 2.8: Computational flow diagram of our *Front Tracking* code.

During the initialisation step the fluid velocities are set to 0 m/s, the pressure is initialised accordingly to the hydrostatic profile, and the initial interface mesh is constructed. From this interface mesh the surface tension forces are computed and the indicator field is calculated. From the indicator field the local density and viscosity are evaluated.

In the main loop firstly the Navier-Stokes equations are solved yielding the flow and pressure fields. Secondly, the interface nodes are tracked with the local interpolated fluid velocity which gives the new position of the interface nodes and implicitly the new bubble shape. Finally the new surface tension forces, indicator field and density and viscosity fields are calculated. Subsequently the time is advanced and the computational steps are repeated until the final time step.

In order to be able to handle very large density variations as often encountered in gas-liquid flows, the Navier-Stokes equations (2.1) are rewritten in their non-conservative form using the continuity equation given

by 2.2.

$$\rho\left(\frac{\partial \mathbf{u}}{\partial t}+\nabla\cdot\mathbf{uu}\right)=-\nabla p+\nabla\cdot\mu\left((\nabla\mathbf{u})+(\nabla\mathbf{u})^{T}\right)+\rho\mathbf{g}+\mathbf{F_{st}} \tag{2.14}$$

Typically the error introduced by assumption is below 0.5% and is therefore accepted.

The convection terms of the Navier-Stokes equation are computed using the Barton scheme, a second order flux-delimited scheme Centrella and Wilson (1984), Harley et al. (1984), Goldschmidt (2001) while the diffusive terms are computed using a standard second order icentral finite difference representation.

The Navier-Stokes equations are solved on a staggered rectangular three-dimensional grid using a finite-volume method, in combination with the SIMPLE algorithm (Patankar, 1980). The pressure Poisson equation (PPE) is solved by an Incomplete Choleski Conjugate Gradient (ICCG) algorithm.

No slip boundary conditions are implemented for all walls except for the top of the computational domain, where a free-slip boundary condition is applied. The computational domain is shifted in such a way that the centre of mass of the total gas content is kept more or less in the centre of the domain. This reduces the number of Eulerian computational cells required to simulate a fast rising gas bubble.

In order to avoid numerical instabilities due to very steep gradients in the density or the viscosity, the interface is extended over four Eulerian grid cells. In this transition zone the fluid properties change smoothly from one side of the interface to the other. This is accomplished by smoothing of $f(\mathbf{x})$ using an integrated Peskin function that is explained in appendix E.

2.4 Model verification

A number of simulations were carried out to check the model performance. The following aspects were investigated:

- Influence of the number of surface elements on the degree of mass conservation.

- Influence of the grid size of the Eulerian mesh on the bubble volume conservation and bubble rise velocity.
- Verification of the surface tension model by comparing the interior excess pressure of a spherical bubble with the analytical solution.
- Influence of Prosperetti's viscosity interpolation on the magnitude of the parasitic currents close to the bubble surface.
- Standard advection test in an artificial flow field.
- Model stability test.
- Influence of the energy minimalisation procedure on the bubble shape and bubble volume conservation.

In the following sections the results of these investigations will be reported.

2.4.1 Number of surface elements

The size of the interface mesh elements was varied to investigate the influence on the bubble behaviour. A 3.4 mm air bubble was released in a 1 cm^3 container filled with water using $20 \times 20 \times 20$ Eulerian grid cells. The number of interface elements is related to the Eulerian grid size. Two computations were performed using an edge length of $\frac{2}{3} \times h_{min}$ and $\frac{1}{3} \times h_{min}$, where h_{min} is the minimum cell spacing of an Eulerian grid cell. After 0.01 s simulated time the maximum variation in the relative gas loss were 0.003% and 0.002% respectively. The finer mesh produced only a slightly better representation of the bubble surface resulting in a somewhat lower deviation from the initial volume of the spherical bubble. The computational time for using the finer mesh is however about 2.5 times as high. Additional calculations were carried out to optimise the desired accuracy in mass conservation and the required computational effort, using an edge length of $\frac{2}{3} \times h_{min}$ for the interface mesh.

2.4.2 Grid size of the Eulerian mesh

The influence of the mesh size of the Eulerian grid was investigated in order to determine the minimum number of nodes required to resolve the flow

Table 2.1: Relative gas loss (in %) for a 3.4 mm diameter air bubble rising in a 1 cm^3 container filled with water over a time period of 0.1 s using different numbers of Eulerian grid cells. Computing time is the time needed on a single CPU 1800 MHz AMD computer. Clift et al. (1978) report a terminal rise velocity Reynolds number of about 80.

number of grid cells in x, y and z direction	terminal rise velocity Reynolds number	relative gas loss [%]	computing time [s]
$20 \times 20 \times 20$	74	-13.5	$9 \cdot 10^3$
$40 \times 40 \times 40$	85	-4.6	$103 \cdot 10^3$
$60 \times 60 \times 60$	85	-2.0	$700 \cdot 10^3$
$80 \times 80 \times 80$	85	-0.9	$1400 \cdot 10^3$

inside the bubble, the surrounding fluid and the interface with reasonable accuracy. Model calculation results for a 3.4 mm diameter air bubble rising in a 1 cm^3 container filled with water, using different numbers of grid cells, are listed in table 2.1.

Based on these results it is concluded that a $60 \times 60 \times 60$ Eulerian grid results in acceptable low gas volume losses and acceptable computing times.

2.4.3 Surface tension model verification

The pressure inside a bubble is higher than the pressure in the surrounding liquid due to the surface tension forces acting on the surface. For spherical bubbles the excess pressure satisfies the Youngs-Laplace equation:

$$\Delta p = \frac{2}{r}\sigma \tag{2.15}$$

In figure 2.9 the pressure distribution inside the gas bubble and the surrounding liquid calculated by the model is compared to the analytical solution. The diameter d_{eq} is the equivalent bubble diameter. The grid spacing is relative to the bubble diameter.

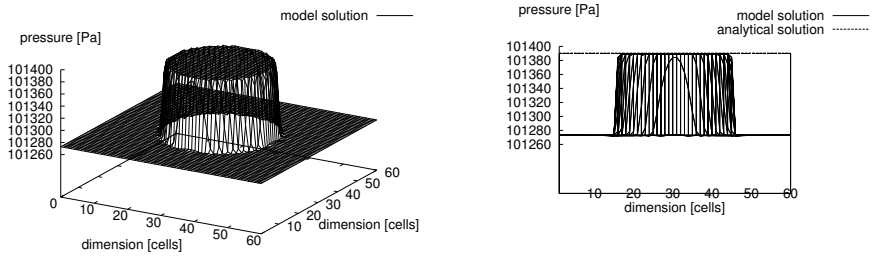

(a)

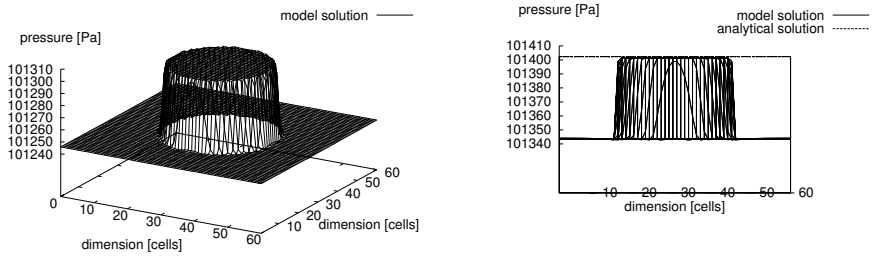

(b)

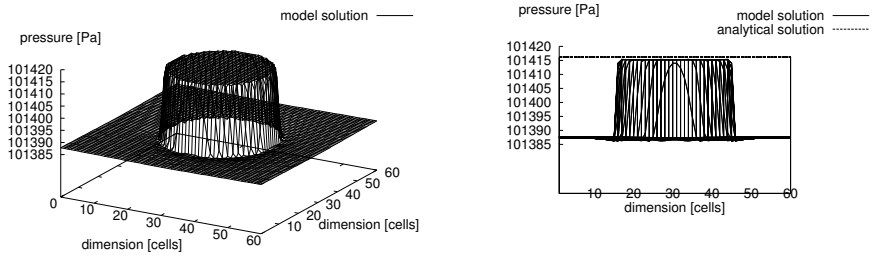

(c)

Figure 2.9: Pressure distribution across the column in a horizontal plane through the centre of a spherical air bubble in water for different bubble diameters keeping the number of grid cells constant at $60 \times 60 \times 60$. (a) $d_{eq} = 2.5\ mm$, (b) $d_{eq} = 5\ mm$ and (c) $d_{eq} = 10\ mm$.

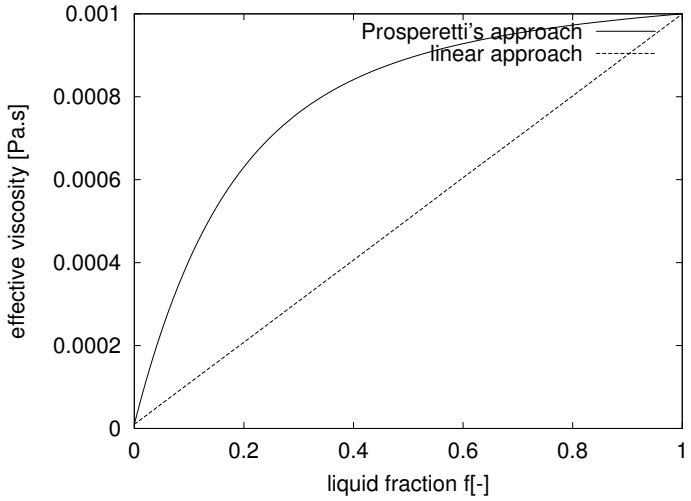

Figure 2.10: Comparison of interface viscosity interpolation methods on the effective viscosity for air-water systems

From this figure it can be concluded that the model is very well capable of computing the pressure distribution for a range of practically relevant bubble diameters. It is also concluded that the surface tension model computes the surface tension forces with good accuracy.

2.4.4 Interface viscosity interpolation

The harmonic averaging of the kinematic viscosity as recently proposed by Prosperetti (2001)(equation 2.6) is compared with the conventional linear weighing (equation 2.5) of the dynamic viscosity. In figure 2.10 the effective viscosity for air water mixtures is given as a function of the liquid fraction. The figure clearly indicates that the effective viscosity near the interface ($f = 0.5$) with the new approach is much higher than with the linear weighing.

If an appropriate smoothing of the indicator function is applied, Prosperetti's approach pushes the high shear region further into the gas phase. This will decrease the velocity near the interface. This is indeed observed in the simulation results (see figure 2.11).

The velocities at the bubble interface (inside as well as outside) are slightly

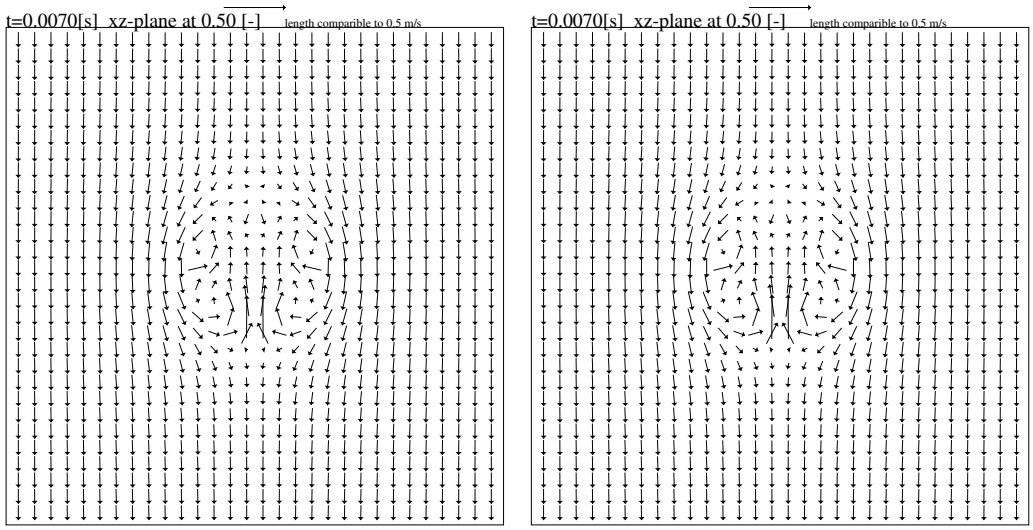

(a) (b)

Figure 2.11: Computed velocity field at a vertical plane through the centre of a 8 mm air bubble in an aquatious sugar solution. Linear weighing (a), Prosperetti's weighing (b), Eulerian grid: $60 \times 60 \times 60$ cells, $\rho_l = 1230\ kg/m^3$, $\mu_l = 0.0237\ Pa.s$, $\sigma = 0.0759\ N/m$, $\rho_g = 1.2\ kg/m^3$.

higher in the case of linear weighing. This can only be observed from comparing the numerical data in detail. On the largest vector a difference of about 5% can be found. Although the effect of these approaches differs slightly, it is expected that Prosperetti's approach gives a more stable computation. Because of this and because of the more fundamental basis of this approach, for all further computations Prosperetti's approach will be used.

2.4.5 Standard advection test

Rider and Kothe (1998) proposed a flux test for *VoF* models, consisting of positioning a gas bubble with a relative radius of 0.15, in a box with unit length imposing a given constant velocity field, for which the stream function Ψ is given below. The initial location of the centre of the bubble is $(0.50, 0.75, 0.50)$.

$$\Psi = \frac{1}{\pi} \sin^2(\pi x) \sin^2(\pi y) \tag{2.16}$$

where $u_x = -\frac{\partial \Psi}{\partial y}$, $u_y = \frac{\partial \Psi}{\partial x}$ and $u_z = 0$.

This test was also applied to the developed *Front Tracking* code to compare the initial shape of the bubble in this artificial flow field with the shape obtained when the flow is advanced for n time steps and then reversed for the same number of time steps. In figure 2.12 the shape of the bubble is presented at the beginning, halfway and in the final situation. The flow was advanced for 1 second ($n = 1000$).

The position of the centre of mass of the bubble in the final situation is exactly equal to the initial location of the bubble, from which it can be concluded that the translation of the verticil and the regridding procedures were implemented correctly. A closer observation of the results reveals that the surface mesh has been deformed, resulting in a somewhat more irregular surface compared with the initial surface mesh. This was to be expected because the criteria for addition and removal of surface elements are not completely reversible. Elements are added if an edge of an element is longer than 1.7 times the grid size of the Eulerian grid and are removed if an edge is shorter than 0.3 times this length.

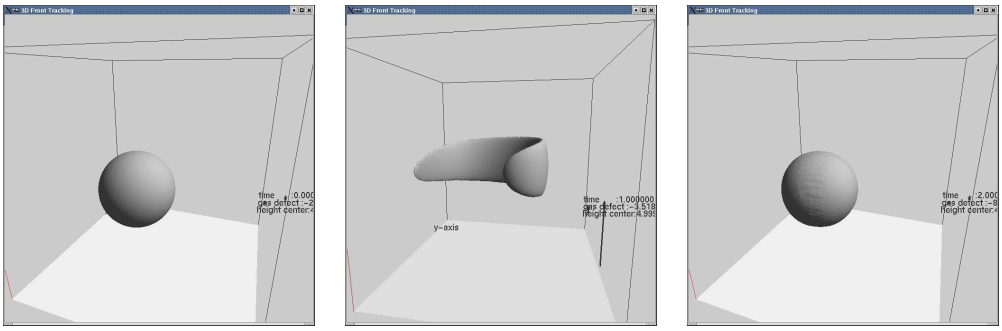

(a) (b) (c)

Figure 2.12: Results for the standard advection test. Initial configuration (a), half time result (b) and final result (c), Eulerian grid : $30 \times 30 \times 30$, the flow is advanced for 1 s and then reversed for 1 s (1000 time steps).

2.4.6 Stability test

A computational experiment was carried out to find out whether the code runs stable also for longer simulation times. In figure 2.13 the result is shown. In table 2.2 the physical data for this computation are given. A low density ratio was chosen to reduce the required calculation time.

The resulting Re number should be about 80 according to the Grace diagram (Clift et al., 1978). The Re number resulting from the stationary rise velocity of the bubble is $Re = 30$. This relative large difference in Reynolds number is probably due to the high gas density and viscosity, resulting in less internal circulation in the bubble. The loss of gas-volume is about 0.25% over the entire simulation time.

2.4.7 Energy minimalisation

Energy minimalisation effects the *Front Tracking* model at two points, the actual value of the indicator function and the local curvature.

The actual values of the indicator function $f(\mathbf{x})$ depend strongly on the exact structure of the interface mesh. In figure 2.14 the relative gas loss for

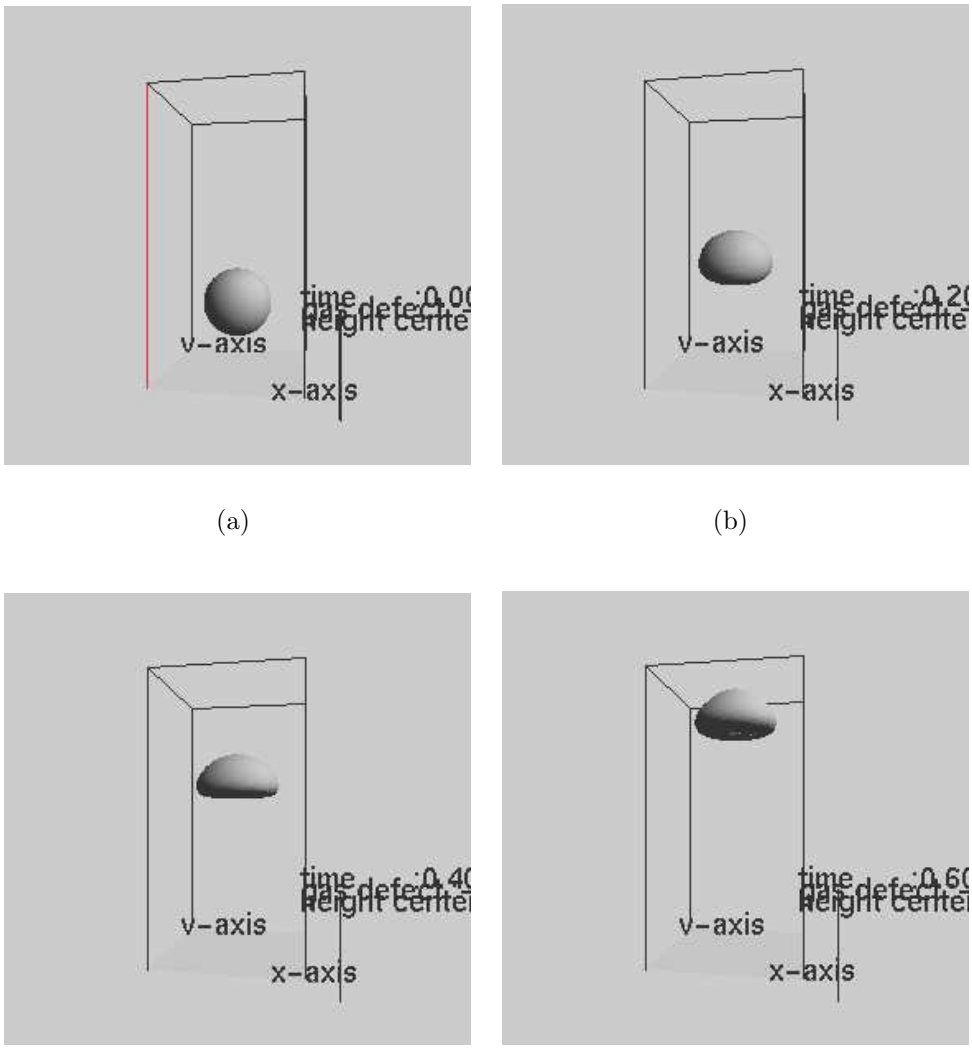

(a) (b)

(c) (d)

Figure 2.13: Result of the stability test using *Front Tracking*. After (a) 0.0 s, (b) 0.2 s, (c) 0.4 s and (d) 0.6 s. Physical data are listed in table 2.2. The dimensions of the computational domain are 0.05 $m \times 0.05 \times 0.10\, m$.

Table 2.2: Physical data for the long time simulation.

equivalent bubble diameter	d_eq	$0.025\ m$
dimensionless numbers	$\log(Mo)$	-3.7
	Eo	12.3
liquid phase	ρ	$1000\ kg/m^3$
	μ	$0.1\ Pa.s$
gas phase	ρ	$800\ kg/m^3$
	μ	$0.1\ Pa.s$
	σ	$0.1\ N/m$
column	number of cells	$50 \times 50 \times 100$
	dimensions	$0.05 \times 0.05 \times 0.1\ m^3$

a simulation with and without incorporation of the energy minimalisation algorithm is shown. Because of the large number of interface elements it is not directly clear which elements have been swapped, but because the coordinates of the marker points involved are not changed, the global topology of the bubble interface does not change much. From the figure it is clear that the minimalisation has a considarable impact on the indicator function $f(\mathbf{x})$, once the bubbles start to deform ($t > 0.04\ s$). The global surface energy decreased about 5 %.

2.5 Conclusion

A full three-dimensional *Front Tracking* code was developed following Unverdi and Tryggvason (1992), with a capability to solve flow problems with a very large density ratio. Furthermore a new method for evaluating the surface tension force as well as an improved version of the Peskin smoothing function and an energy minimalisation algorithm were embedded in the code.

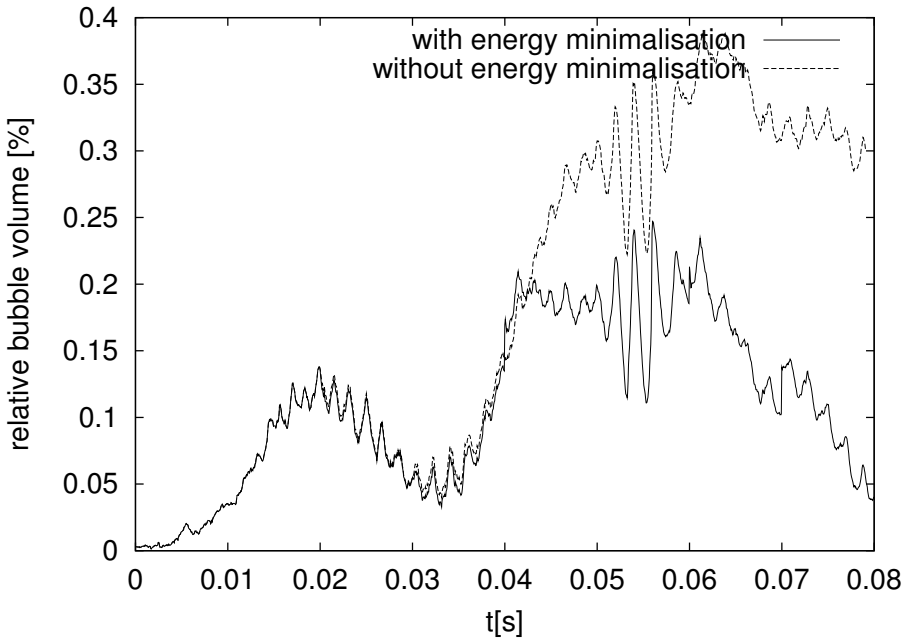

Figure 2.14: Relative gas loss as function of time for a simulation with and without the energy minimalisation algorithm of van Damme and Alboul (1995). Bubble diamteter $d_{eq} = 8\ mm$ Dimensionless numbers Eö= 10, $\log(Mo) = -5.24$.

2.5.1 Verification

In a number of test cases all parts of the implementation were tested and it was concluded that

- The number of nodes in the unstructured mesh that represents the interface has almost no effect on the relative gas losses for spherical and ellipsoidal bubble shape, but it does have a large effect on the computational time required. Taking surface elements with an initial edge length of $\frac{2}{3}\min(h_x, h_y, h_z)$ seems optimal.

- By varying the Eulerian grid size, compared to the bubble size, it was found that at least 20 Eulerian cells contained in the bubble in each spatial direction should be selected to obtain a reasonable accuracy. The required computational time varies almost linearly with the number of Eulerian nodes, but the difference in relative gas losses between a $60 \times 60 \times 60$ and $80 \times 80 \times 80$ grid is relatively small, so the former grid seems sufficiently accurate.

- The new surface model is well capable of predicting the surface tension forces as can be concluded from the almost exact agreement with the analytical solution for the excess pressure inside a spherical bubble. Since this method needs less computational work, it is preferred over the method proposed by Tryggvason et al. (1998).

- The viscosity is evaluated using the scheme proposed by Prosperetti (2001). This method has a sound physical basis and is therefore preferred.

- The code gave good results for a deformation test similar to the one carried out by Rider and Kothe (1998) for *VoF*-models. The deformation test gives confidence in the correct implementation of the *Front Tracking* algorithm.

- The code has been tested for a problem running over a large number of time steps demonstrating the numerical stability of the code.

- The energy minimalisation has shown to have a considerable impact on the computed relative bubble volume wich implies that the actual

stucture of the interface is very important to the final outcome of the simulations.

Overall it is concluded that the model is fully functional and has a number of improvements over the existing codes.

In chapter 4 the computational results of the presented *Front Tracking* model are shown. The the bubble shape and the rise velocity will be compared to experimental data reported in literature and to data from ultra sound measurements.

2.6 Acknowledgements

The author wishes to acknowledge prof. G. Tryggvason for giving me the opportunity to stay at the Worcester Polytechnical Institute and for introducing me to the details of their codes. The author also likes to acknowledge dr. A. Esmaeeli for his kind guidance and email support during and after my stay at WPI and thanks to all the kind people at WPI who supported me when I encountered problems returning home due to the criminal attack on the World Trade Centre in New York on the 11th of September 2001.

Chapter 3

Modelling single gas bubble behaviour using the Volume of Fluid method

Abstract

Volume of Fluid (*VoF*) models were introduced in the 1970s by DeBar (1974), Nichols and Hirt (1975), Hirt and Nichols (1981) and Noh and Woodward (1976). *VoF* models reconstruct an interface from the local gas or liquid fraction distribution. Once the interface is computed the fluxes through the cell faces for each fluid phase can be calculated very accurately, where mass conservationi is inherently assured. The velocity field is calculated from the Navier-Stokes equations on a staggered Cartesian mesh using a one fluid formulation, where the local density and viscosity are evaluated from the local liquid fraction distribution. In this study a three dimensional Youngs *VoF* algorithm was implemented in a computer code to calculate the interface fluxes.

New elements that were included are

- a new surface tension model based on the concepts derived from *Front Tracking* models,
- smoothing of the indicator function for the computation of the normal

to the interface (required for the evaluation of the fluxes and the surface tension forces) and

- a correction for non-divergence free flow fields (arising from very small residuals in the iterative solution of the pressure Poisson equation (PPE)).

The simulation results show that the new algorithm for evaluating the surface tension does predict the internal excess pressure very accurateily. The representation has improved significantly by using a smoothed indicator function in the computation of the normal to the interface and the inon-zero divergence correction shows indeed a very rigorous conservation of mass that cancels exactly the numerical error introduced by solving the Pressure Poisson Equation (PPE). These three improvements enable us to perform simulations involving small bubbles or liquids with a high surface tension as compared to the conventional approach (surface tension evaluated by the *CSF* model (Brackbill et al., 1992), no smoothing of the indicator function for computing the normal to the interface and no inon-zero divergence correction).

Simulations were carried out to verify the new computational methodologies and the predicted bubble shape and bubble dynamics. The flux computation performs well, the code runs stable over long (simulation) times and the new surface tension model gives a very accurate prediction of the excess pressure inside a spherical bubble.

3.1 Introduction

Gas-liquid two phase flow is encountered in a large variety of process equipment, such as in bubble columns and distillation columns. Since these pieces of process equipment are very frequently applied, an optimal design and operation is of great (economic) interest. Since the advent of chemical engineering, the design of various kinds of equipment was based on extensive experimentation and usage of empirical correlations. Due to advances in computational methods and the increased computer capacity, computer simulation of complex multi fluid flows has come within reach. The usage of validated computer models can significantly reduce the extent and cost of required experimental work. However, fundamental knowledge that is needed

for the optimal design of process equipment is still lacking. Questions that need to be answered demand for very detailed experiments. Since these experiments are often difficult if not impossible to conduct, there is a large interest in simulation tools that can provide this detailed information and insight. In this study such a detailed model was developed for gas-liquid two phase-flow.

It was decided to develop a *VoF* model because of its very good inherent mass conservation. A known drawback of this model is the poor prediction of the surface tension force by the CSF method (Zaleski, 1999), especially at points where the interface has a strong curvature compared to the computational mesh size. In this chapter a completely new surface tension method, that ovecomes this limitation, will be presented.

Since the introduction of the *VoF* method numerous researchers have worked in this field. Rider and Kothe (1998) give an excellent overview of the history, all the 'flavours' and the advances in *VoF* that were made over the last three decades.

Yet the essence of all these *VoF* models is the same. From a known spatial liquid fraction distribution, $f(\mathbf{x})$, in a given computational domain the normal $\mathbf{n}$ to the interface has to be determined. One of the most often used methods is given below, although Rider and Kothe (1998) describe a number of alternative methods.

$$\mathbf{n} = \frac{\nabla f(\mathbf{x})}{|\nabla f(\mathbf{x})|} \tag{3.1}$$

From the normal $\mathbf{n}$ and the liquid fraction $f(\mathbf{x})$ an interface is constructed in every computational cell. In our computer code, the model originally proposed by Youngs (1982) (see also Youngs (1987) and Rudman (1997)) has been used. This model was preferred because of its relatively simple implementation e.g. compared to higher order methods like for example the *ELVIRA* model from Zaleski (1999) and because of its superior performance compared to the classical model proposed by Nichols and Hirt (1975). Rudman (1997) and Zaleski (1999) have presented good overviews of the accuracy of the different *VoF* implementations.

Once the interface is reconstructed the flux of material through the faces of the Eulerian cells can be calculated using the computed flow field. From

these fluxes the liquid fraction at the new time step can be evaluated. At the new time step the flow field is solved again.

In our implementation of *VoF*, two models for the surface tension force have been included and mutually compared. One model is the well-known *CSF* model from Brackbill et al. (1992), the second model is a new model that is based on the surface tension model used by Bunner and Tryggvason (1997) in their *Front Tracking* codes. Both models use a 27 points stencil to calculate the normal $\mathbf{n}$. The *CSF* method also requires the derivatives of the normal which makes this method very sensitive to minor numerical errors in the liquid fraction field. As a consequence the curvature can only be calculated accurately if the curvature is relatively small compared to the mesh size. The new model calculates the surface tension forces on the edges of the surface elements using the normal vectors to the adjacent surface elements. This enables an accurate computation of the surface tension forces over a large range of curvatures.

Rider and Kothe (1998) have demonstrated that direct application of equation 3.1 to the indicator field could lead to a mis-prediction of this normal. This conclusion has been confirmed in our study. Other methods given by Rider and Kothe (1998) use a complicated iterative method and are therefore not considered. We propose a model that evaluates the normal to the interface from a smoothed indicator function, denoted by $\tilde{f}(\mathbf{x})$. The smoothing function proposed here is an integrated Peskin function.

The PPE equation is solved using an iterative numerical solution alorithm. This introduces small numerical erros that cause a non-zero divergence of the flow field. The correction proposed by Kothe et al. (1994) was implemented in our code to minimize the effect of this non-zero divergence.

In this chapter, the model equations and the numerical method will be briefly reviewed, followed by a detailed description of the construction of the interface and the evaluation of the surface tension forces.

A model verification has been conducted, which provides information on the algorithms and the quality of the model predictions.

In chapter 4 the presented *VoF* model will be compared to experimental data ontained from literature as wel as to experimental data obtained from ultrasound measurements. In this chapter also the results from simulations with this *VoF* code will be compared to simulation results the *Front Tracking*

code as described in the chapter 2.

3.2 Model equations

In this section the model equations will be presented.

3.2.1 Flow problem

A one-fluid formulation is used to solve the flow field. An indicator function $f(\mathbf{x})$ is used to indicate the local volume fraction of the two phases. Here $f(\mathbf{x}) = 1$ indicates the liquid phase and $f(\mathbf{x}) = 0$ the gas phase. The *VoF* model insures that $f(\mathbf{x})$ is conserved where $f(\mathbf{x})$ obeys:

$$\frac{Df(\mathbf{x})}{Dt} = 0 \tag{3.2}$$

The local density and viscosity are evaluated as a function of $f(\mathbf{x})$, according to

$$\rho = f(\mathbf{x})(\rho_l - \rho_g) + \rho_g \tag{3.3}$$

or

$$\frac{\rho}{\mu} = f(\mathbf{x})\left(\frac{\rho_l}{\mu_l} - \frac{\rho_g}{\mu_g}\right) + \frac{\rho_g}{\mu_g} \tag{3.4}$$

The harmonic averaging of the kinematic viscosity was proposed by Prosperetti (2001) and can be interpreted as an analogy of parallel electrical resistances. In section 2.2.1 this is explained in more detail.

The Navier-Stokes equations describe the motion of the unsteady, viscous, incompressible, immiscible two-fluid flow system.

$$\frac{\partial \rho \mathbf{u}}{\partial t} + \nabla \cdot \rho \mathbf{u}\mathbf{u} = -\nabla p + \nabla \cdot \mu \left((\nabla \mathbf{u}) + (\nabla \mathbf{u})^T\right) + \rho \mathbf{g} + \mathbf{F_{st}} \tag{3.5}$$

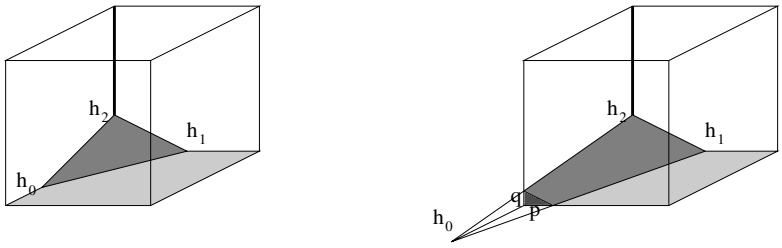

Figure 3.1: Interface element type 1 and 2.

Here $\mathbf{u}$ is the velocity field, ρ and μ are the density and viscosity fields, respectively and $\mathbf{F_{st}}$ is the surface tension force which only acts in the vicinity of the interface.

The Navier-Stokes equations are supplemented by the incompressibility condition

$$\nabla \cdot \mathbf{u} = 0 \tag{3.6}$$

and the equations of state for the density and viscosity.

3.2.2 Interface reconstruction and flux calculations

The key issue in *VoF* methods is the reconstruction of the interface. In this section the methods used in our implementation will be discussed.

Youngs (1987) reported that, if appropriate rotation and transformations are applied to the interface normal $\mathbf{n}$, the number of possible interface element types that need to be used to construct a piece-wise linear interface in a three dimensional space, is essentially five. These types are given in figures 3.1 to 3.3.

To determine what type of interface element is present in a computational cell a few steps are taken.

- The first step is the calculation of the normal to the interface using equation 3.7. Note that the smoothed indicator function $\tilde{f}(\mathbf{x})$ is used

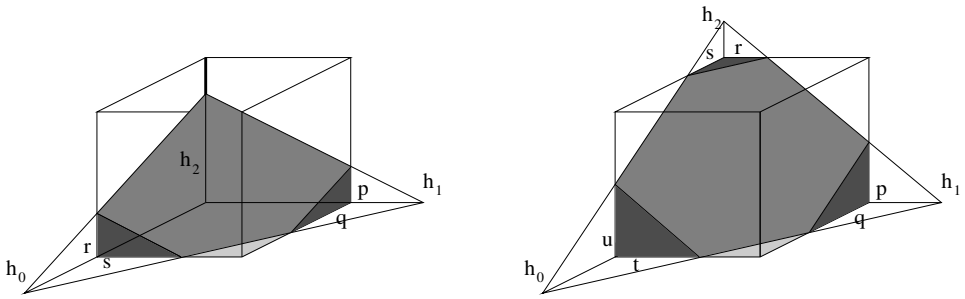

Figure 3.2: Interface element type 3 and 4.

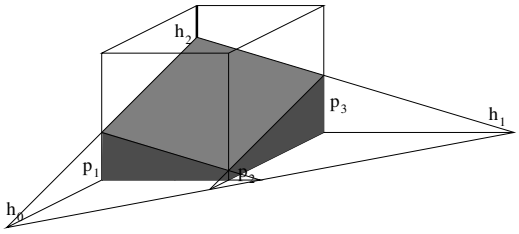

Figure 3.3: Interface element type 5.

here instead of the normal indicator function $f(\mathbf{x})$, as used in equation 3.1.

$$\mathbf{n} = \frac{\nabla \tilde{f}(\mathbf{x})}{\left|\nabla \tilde{f}(\mathbf{x})\right|} \tag{3.7}$$

Using the normal computed from the smoothed indicator function the adjacent surface elements are much better connected.

- The numerical procedure assumes $f(\mathbf{x}) \leq \frac{1}{2}$. If a cell is filled for more than 50% with liquid, the liquid and gas phase are temporarily exchanged in the numerical procedure. Once the fluxes through the interfaces are computed the real fluxes are calculated by reverting the gas and the liquid flux.

- The last step is calculation of a number of limiting criteria from which the interface type can be determined. These criteria are summarised in table 3.1. More details can be found in appendix A.

Once the interface elements and the velocities on the cell boundaries are known, the fractions that will be fluxed to the neighbouring cells can be computed. Due to the small time step a split advection is sufficiently accurate and is therefore used. In figure 3.4 a two-dimensional example of the flux calculation is summarised. The equations needed to compute the fluxes in a three dimensional domain are given in appendix A.

Flux correction

The flow solver applies an iterative method to solve the PPE and consequently small numerical deviations from the continuity equation will be produced. Since equation 3.2 is not solved directly but via the fluxes computed from the interface and flow field, this leads to a small mis-prediction of the fluxes computed by the *VoF* algorithm.The algorithm does not account for the right hand side term given in equation 3.8, which is an extended formulation of 3.2. This was firstly reported by Rider and Kothe (1998).

$$\frac{\partial f}{\partial t} + \nabla \cdot (\mathbf{u} f) = f \nabla \cdot \mathbf{u} \tag{3.8}$$

Table 3.1: Selection criteria for the five surface element types. $n_0 = \min(n_x, n_y, n_z)$, $n_1 = \text{median}(n_x, n_y, n_x)$ and $n_2 = \max(n_x, n_y, n_z)$.

type	criterion
1	$6fn_0n_1n_2 \leq {n_0}^3$
2	${n_0}^3 < 6n_0n_1n_2f \leq {n_1}^3 - (n_1 - n_0)^3$
3	$n_0 + n_1 \geq n_2$ and ${n_1}^3 - (n_1 - n_0)^3 < 6fn_0n_1n_2 \leq {n_2}^3 - (n_2 - n_0)^3 - (n_2 - n_1)^3$ or $n_0 + n_1 < n_2$ and ${n_1}^3 - (n_1 - n_0)^3 < 6fn_0n_1n_2 \leq (n_0 + n_1)^3 - {n_0}^3 - {n_1}^3$
4	$n_0 + n_1 \geq n_2$ and ${n_2}^3 - (n_2 - n_0)^3 - (n_2 - n_1)^3 < 6fn_0n_1n_2$
5	$n_0 + n_1 \leq n_2$ and $(n_0 + n_1)^3 - {n_0}^3 - {n_1}^3 < 6fn_0n_1n_2$

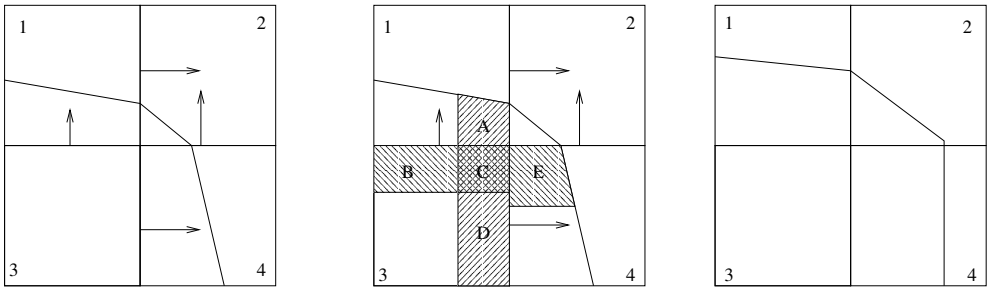

Figure 3.4: Two dimensional flux example. The left figure shows the original surface and velocity field. The middle figure shows the liquid phase that is being fluxed and the right figure shows the final configuration after the phases fluxed. Element A is fluxed to cell 2, B to cell 1, D to cell 4 and E to cell 2. Due to the split advection scheme block C is fluxed twice once to cell 1 and once to cell 4.

In the present code a non-zero divergence correction is applied. From a detailed analysis of the flow-field and the f-field data it can be concluded that this correction indeed exactly cancels all numerical errors introduced by the iterative matrix solver.

3.2.3 Treatment of the discontinuety at the interface

In most *VoF* models large gradients in the indicator function exist, causing numerical instabilities when solving the Navier-Stokes equations with a surface tension source term. Firstly, since the density and viscosity depend on the indicator function also these variables can have very steep gradients. Furthermore, the surface tension force is acting at the position of the interface as well. This induces a large momentum source term in the Navier-Stokes equations, resulting in very high velocities of the less dense phase close to the interface. High fluid velocities result in a low pressure as can be seen in figure 3.5.

In their RIPPLE-code, Kothe et al. (1994) proposed to use equation 3.9 to push the action of the surface tension into the liquid phase. By multiplying the computed surface tension force by $2f(\mathbf{x})$ the action of this force is reduced at the gas phase side of the interface while it is doubled on the liquid side. Since the density on the liquid side is higher the momentum is reduced.

$$F_{st} = 2f(\mathbf{x}) F_{st} \tag{3.9}$$

This function was applied in the same simulation as mentioned before. The resulting pressure distribution is given in the second graph of figure 3.5. It succeeds in minimising the pressure undershoot but the excesspressure inside the bubble, is almost half the excesspressure that should be expected from the analytical solution. This method is therefore not preferred.

A new method that is introduced here involves the use of a smoothed indicator function $\tilde{f}(\mathbf{x})$. This $\tilde{f}(\mathbf{x})$ is computed from the following expression:

$$\tilde{f}(\mathbf{x}) = \sum D(\mathbf{x} - \tilde{\mathbf{x}}) f(\mathbf{x}) \tag{3.10}$$

where the smoothing function $D(\mathbf{x} - \tilde{\mathbf{x}})$ is an integrated version of the one given by Peskin (1977). This function is explained in detail in in appendix E.

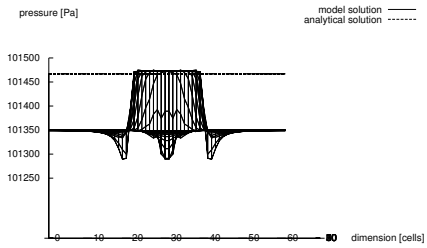

(a)

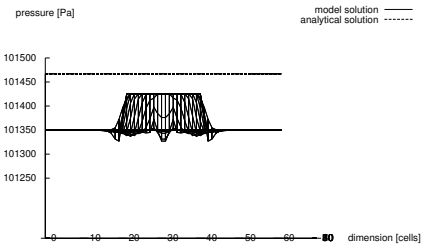

(b)

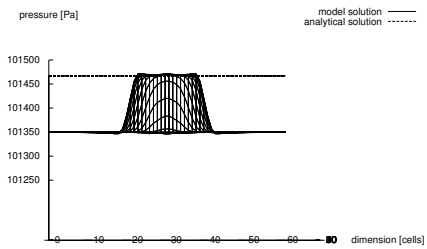

(c)

Figure 3.5: Pressure profile for *CSF* model without any correction (a) and with RIPPLE correction (b) and with smoothing function (c).

If the local density and viscosity are evaluated from $\tilde{f}(\mathbf{x})$ the gradients vary smoothly over the interface. The result obtained after applying this method is shown in the last graph of figure 3.5.

The excesspressure inside the bubble is predicted very well and the low pressure regions have vanished. Therefore this method has been used for all computations reported in this chapter.

Another advantage of this smoothed indicator function $\tilde{f}(\mathbf{x})$ is that, when the normal computed from this smoothe is used foa determlining the surface element types, the connection of adjacent interface elements is much better than by making use of the non-smoothed indicator function $f(\mathbf{x})$. However for the computation of the volume beneath the surface in both cases the non-smoothed $f(\mathbf{x})$ is used.

3.2.4 Surface tension force

In many *VoF* models, e.g. Rudman (1997) and Delnoij (1999) the surface tension force is computed using the *CSF*-model of Brackbill et al. (1992). This model uses a $3 \times 3 \times 3$ (in three dimensions) stencil for computing the normal $\mathbf{n}$ to the interface as well as $\nabla\mathbf{n}$. Both are used for the calculation of the curvature, which is in its turn used for the calculation of the surface tension force. The numerical differentiation implicitly used in this procedure makes the evaluation of the curvature very sensitive to mis-predictions of $\mathbf{n}$. Therefore, a new surface tension force method has been developed and implemented that avoids the calculation of this derivative.

In this section first a brief description of the *CSF* model is given, followed by the introduction of the new model, that is inspired on the approach reported in chapter 2.

CSF-surface tension model

The *CSF*-model calculates the surface tension force according to the following expression

$$F_{st} = \sigma\kappa(\mathbf{x}) \frac{\nabla f(\mathbf{x})}{[f]} \tag{3.11}$$

where, κ is the curvature and $[f]$ the jump in the indicator function. In the case of *VoF* $[f] = 1$ when going from one phase to the other phase. The curvature is calculated from

$$\kappa = \frac{1}{|\mathbf{n}|}\left[\left(\frac{\mathbf{n}}{|\mathbf{n}|}\cdot\nabla\right)|\mathbf{n}| - (\nabla\cdot\mathbf{n})\right] \tag{3.12}$$

where $\mathbf{n}$ is the normal to the interface that is computed as:

$$\mathbf{n} = \nabla f(\mathbf{x}) \tag{3.13}$$

The main disadvantage of this method is that the derivative of $\mathbf{n}$ must be calculated numerically from the gradient of $f(\mathbf{x})$ or $\tilde{f}(\mathbf{x})$, thus $\nabla\mathbf{n} = \nabla^2 f(\mathbf{x})$.

New surface tension model

Motivation The development of the new surface tension force model was initiated by the following two observations. Firstly *VoF* models conserve mass in a very rigorous manner compared to *Front Tracking* models (see figure 3.6). Secondly, the treatment of the surface tension in *Front Tracking* models is much better than in the conventional *CSF* model used in most *VoF* codes. Two major advantages of the *Front Tracking* approach to calculate the surface tension force are:

- *Front Tracking* is capable of handling highly curved interfaces.
- *Front Tracking* produces significantly smaller parasitic currents.

A new surface tension force model is developed incorporating the surface tension force model as used in *Front Tracking* models into the *VoF* model to get the best of both. The new surface tension force model avoids the calculation of the derivatives of $\mathbf{n}$.

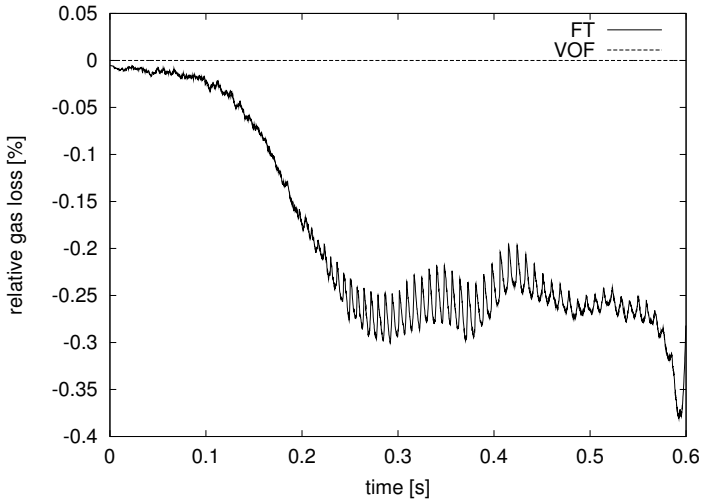

Figure 3.6: Conservation of mass in *Front Tracking* and *VoF*. These data were taken from the stability tests. The decrease in relative gas volume for the *VoF* calculation is in the order of 10^{-5} %.

Model The proposed surface tension force model calculates the surface tension forces directly from the interfacial pull forces acting between neighbouring surface elements. These forces are calculated using the counter clockwise tangent vectors along the edges of the five surface element types (see figure 3.7). The types of the surface elements are determined from the smoothed indicator field. After re-translation of the surface elements from their 'standard-case-position' to their real position in the computational domain the resulting contribution to the pull force is computed from

$$(\mathbf{F_{st}})_{i,j} = \sigma l_{edge}(\mathbf{t_{i,j}} \times \mathbf{n_j}) \tag{3.14}$$

$(\mathbf{F_{st}})_{i,j}$ is the pull force acting on element i, at the edge connecting elements i and j. Here σ is the surface tension constant, l_{edge} is the length of the edge, $\mathbf{t_{i,j}}$ is the unit tangent vector between the elements i and j, and $\mathbf{n_j}$ is the unit normal vector on element j (see figure 3.8).

The implementation of the re-translation procedure is one of the procedures that requires special attention for this method to work properly. The details of the initial translation and the re-translation are given in appendix B.

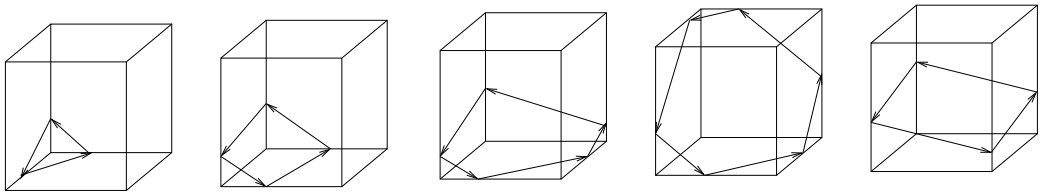

Figure 3.7: Tangent vectors for the five types of interface elements.

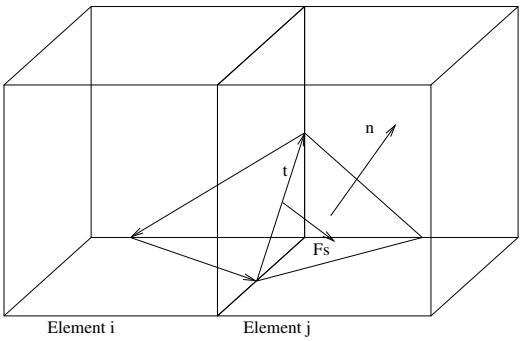

Figure 3.8: Calculations of the contribution of the pull force acting on element i via the connection with element j.

Summing all the pull forces for reference element i produces the net surface tension force acting on this element. Subsequently, the individual forces of all the edges of all the elements must be distributed to the Eulerian grid. Since the edges of the surface elements are at the cell faces, the force acting at the position of the cell face can be obtained from the summation of the forces acting on the two surface element edges that are at this cell face. This however, introduces a strong discontinuity in the Navier-Stokes equations. Therefor, very similar to the approach taken in *Front Tracking*, it was chosen to distribute the surface tension forces using

$$\mathbf{F_{st}} = \sum D\left(\mathbf{x} - \tilde{\mathbf{x}}\right) \mathbf{F_{st\,i,j}} \tag{3.15}$$

Where for the distribution function $D\left(\mathbf{x} - \tilde{\mathbf{x}}\right)$, again the integrated version of the Peskin function was used (see appendix E).

Results A first check on the performance of the new surface tension force model has been carried out by comparing simulation results for the excess pressure inside a spherical bubble with the analytical solution, the Youngs-Laplace equation. When comparing the pressure distribution predicted by the *CSF* model and the new surface tension model (both using the smoothed indicator function), see figure 3.5(c) and figure 3.14(c), a much steeper gradient at the interface is computed with the new model. Results will be discussed in more detail in section 3.4.4.

Another goal of the new model was to decrease the magnitude of the parasitic currents. In figure 3.9 the computed parasitic currents for a spherical bubble in a zero gravity field are shown. The simulated bubble is a 3.4 mm argon bubble in water on a $20 \times 20 \times 20$ Eulerian grid, $h = 0.226\ mm$. The flow field shown is in the xy-plane that crosses the centre of the bubble. The figure clearly indicates that the parasitic currents are significantly reduced. Most of the velocity vectors point in opposite direction in the two figures. This is caused by differences in the oscillation phase of the bubble at a given time step (induced by numerical errors), predicted by the two different models. Compared to the flow patterns induced by convection the magnitude of the parasitic currents is small. Only highly curved interfaces (small bubbles) are influenced by these currents.

Finally, differences in the shape of a rising bubble can be observed. In section 3.4.3 a series of simulations of rising gas bubbles will be presented calculated

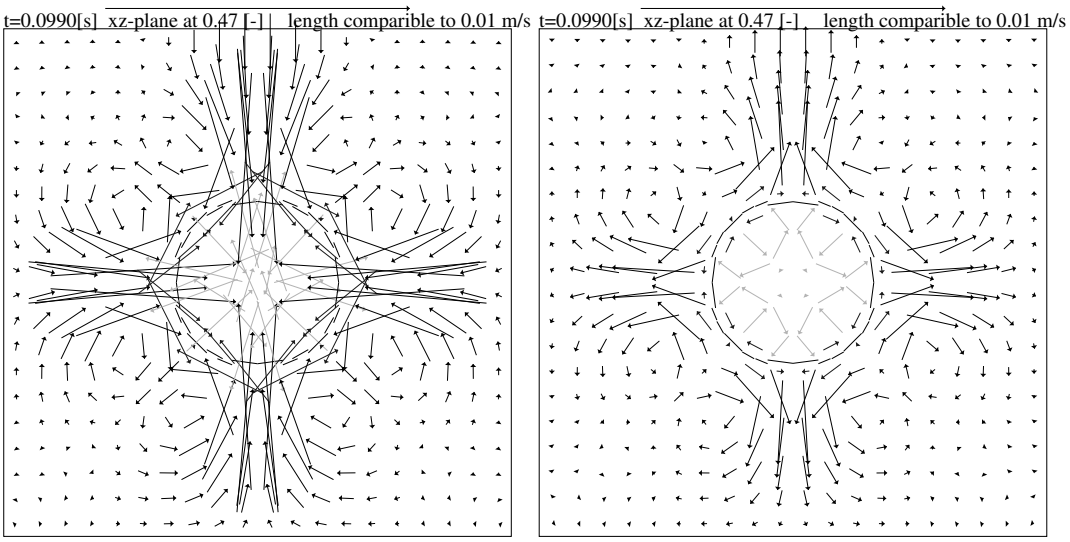

(a) (b)

Figure 3.9: Parasitic currents in a gravitation free field using the *CSF*-model (a) and the new surface tension force model (b).

using either the *CSF* model or the new surface tension force model. In section 2.4.6 a bubble with the same physical and model parameters was simulated using the *Front Tracking* model. From these figures it can be seen that the rear side of the bubble calculated using the new surface tension force model retains its somewhat curved shape, while with the *CSF* model a flat bottom is predicted. When comparing the computational shape of the bubble to the shape predicted by the bubble diagram of Grace (1973)(see figure 4.1) the more curved shape calculated by the new method seems to be more in line with experiments.

3.3 Numerical method

The implementation of the model equations in the code is given schematically in figure 3.10.

During the initialisation step the pressure is set according to the hydrostatic pressure profile and all velocity components are set to 0 m/s, corresponding to an initially stagnant fluid. From the specified initial position of the gas bubble the indicator field is computed by first setting all cell values to 1 and than subtracting the fraction of gas present in that cell. From the indicator field the local density and viscosity are evaluated and an bubble interface is constructed. This first interface is needed to compute the surface tension forces. In the main loop firstly the Navier-Stokes (3.16) equations are solved, whereas the second step in the main loop involves the determination of the interface information from the indicator field of the previous time step. Once the interface data and the velocity field have been computed, the fluxes through the cell faces can be computed. These are used to compute the new indicator field. In the last step in the main loop the density, viscosity and surface tension forces are updated. The finalisation step, called when the end time of the simulation has be reached, frees the computer memory and stores the final data.

The Navier-Stokes equations are rewritten in the non-conservative form for incompressible fluids:

$$\rho\left(\frac{\partial \mathbf{u}}{\partial t} + \nabla \cdot \mathbf{uu}\right) = -\nabla p + \nabla \cdot \mu\left((\nabla \mathbf{u}) + (\nabla \mathbf{u})^T\right) + \rho \mathbf{g} + \mathbf{F_{st}} \quad (3.16)$$

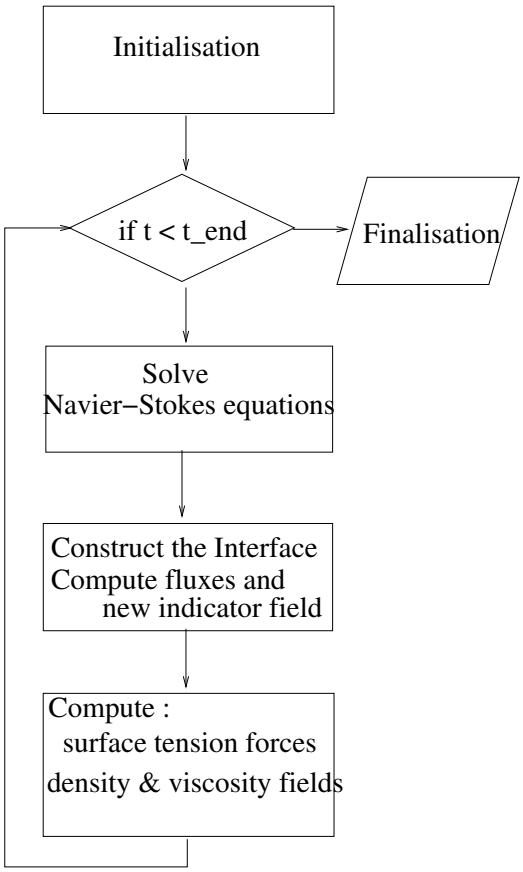

Figure 3.10: Computational flow diagram of the *VoF* code.

For the density the value of the former time step is used. This opens the possibility to solve problems with a very large density ratio. The error introduced by this method is very low, typically below 0.5% fot the time step used in this work.

The convection terms of the Navier-Stokes equations are computed using the second order scheme proposed by Barton Centrella and Wilson (1984), Harley et al. (1984) while the diffusive terms are computed using standard second order finite difference representations.

The equations are discretized on a three dimensional rectangular staggered mesh. The pressure Poisson equation (PPE) is solved by an Incomplete Choleski Conjugate Gradient (ICCG) algorithm.

On all the boundaries of the computational domain, except the top, no slip conditions were applied, while for the top a continuative inflow of outflow condition was used.

The density, viscosity and normal to the interface are evaluated from the smoothed indicator function $\tilde{f}(\mathbf{x})$. This gives a smooth change in density and viscosity resulting in improved numerical stability and and a better representation of the interface (improved connection between adjacent surface elements).

3.4 Model verification

In this section a number of tests are presented that were carried out to show the capabilities of the model. The following four topics were investigated and discussed in the next subsections:

- Influence of the grid size of the Eulerian mesh on the conservation of the bubble volume and the terminal rise velocity of the bubble.
- Standard advection test in an artificial flow field.
- Model stability test.
- Verification of the new surface tension force model by comparing the interior excess pressure of a spherical bubble with the analytical solution.

3.4.1 Influence of the Eulerian grid size

A number of simulations were performed to check the influence of the Eulerian grid size and to determine the minimum number of nodes that are needed to resolve the flow phenomena near a bubble with a reasonable accuracy. All simulations were carried out for a 3.4 mm diameter air bubble rising in a 1 cm^3 container filled with water. In table 3.2 the grid size used is shown as well as the volume changes after 0.1 s and the Reynolds number at that time, all rising bubbles reached their terminal rise velocity .

The gas loss is for all cases very small and well within the acceptable range. As can be seen the error increases with the number of grid cells. This is related to the increasing Courant-number. In all simulations the same time step was applied. By decreasing the mesh size a relative larger part of a control volume is fluxed during one time step. The Reynolds number at terminal rise velocity of a 3.4 mm diameter air bubble in water is about 80. It was chosen to use a $60 \times 60 \times 60$ grid for further computations.

Table 3.2: Relative change in gas volume (in %) and terminal rise velocity (in m/s) for a 3.4 mm air bubble rising in a 1 cm^3 container filled with water over a time period of 0.1 s using different numbers of Eulerian grid cells. The reported computing time is the time needed on a single CPU 1800 MHz AMD PC.

Number of grid cells in x,y and z direction	relative gas volume[%]	Reynolds number	computing time [s]
$20 \times 20 \times 20$	$+0.00005$	75	$13 \cdot 10^3$
$40 \times 40 \times 40$	-0.00005	75	$150 \cdot 10^3$
$60 \times 60 \times 60$	-0.0008	75	$536 \cdot 10^3$
$80 \times 80 \times 80$	-0.0022	75	$1900 \cdot 10^3$

3.4.2 Standard advection test

For a proper analysis of the performance of *VoF*-models, Rider and Kothe (1998) have indicated that a severe test should be carried out that brings about pronounced topology changes to elucidate the strengths and weaknesses of the algorithm. Among other methods they propose a single vortex advection test with the stream function given by

$$\Psi = \frac{1}{\pi} \sin^2(\pi x) \sin^2(\pi y) \tag{3.17}$$

where $u_x = -\frac{\partial \Psi}{\partial y}$, $u_y = \frac{\partial \Psi}{\partial x}$ and $u_z = 0$. This velocity field was applied to a bubble with a relative radius of 0.15 at position $(0.5, 0.25, 0.5)$ in a unit length box. In figure 3.11 the initial configuration and the deformed interface after 1 s (1000 time steps) and the final interface after again 1 s are given. By comparing this result obtained with *Front Tracking* it can be concluded that the latter yields better results for this test case.

By comparing the first and the last figure it is concluded that the flux mechanism is working properly with reasonable accuracy.

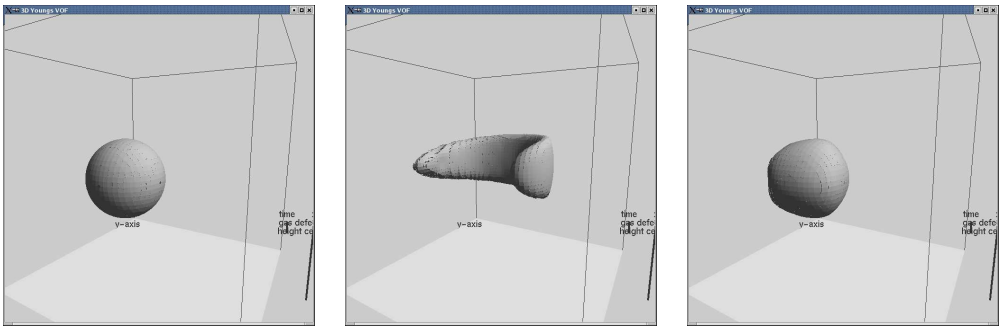

(a) (b) (c)

Figure 3.11: Result from the standard advection test. The flow is advanced for 1 s (1000 time steps) and then reversed for 1 s. Initial configuration (a), half time result (b) and final result (c), mesh : $60 \times 60 \times 60$.

3.4.3 Model stability test

In this section simulations will be presented to check whether the code can run stable for a long period of simulation time. To speed up these simulations a low density ratio was selected. The physical properties used for these simulations are given in table 3.3.

The results of these computations are summarised in figure 3.12 and figure 3.13. In figure 3.13 the new surface tension force model was used and in figure 3.12 the conventional *CSF*-model was used.

It can be concluded that the code can run stable for long simulation times. Small differences in the shape of the bubble can be discerned between the simulation using the *CSF*-model and the new surface tension force model. This is attributed to a better prediction of the surface tension force at the highly curved parts of the bubble interface. A higher value of the surface tension force acting at these locations gives the bubble a slightly more 'ellipsoidal' shape.

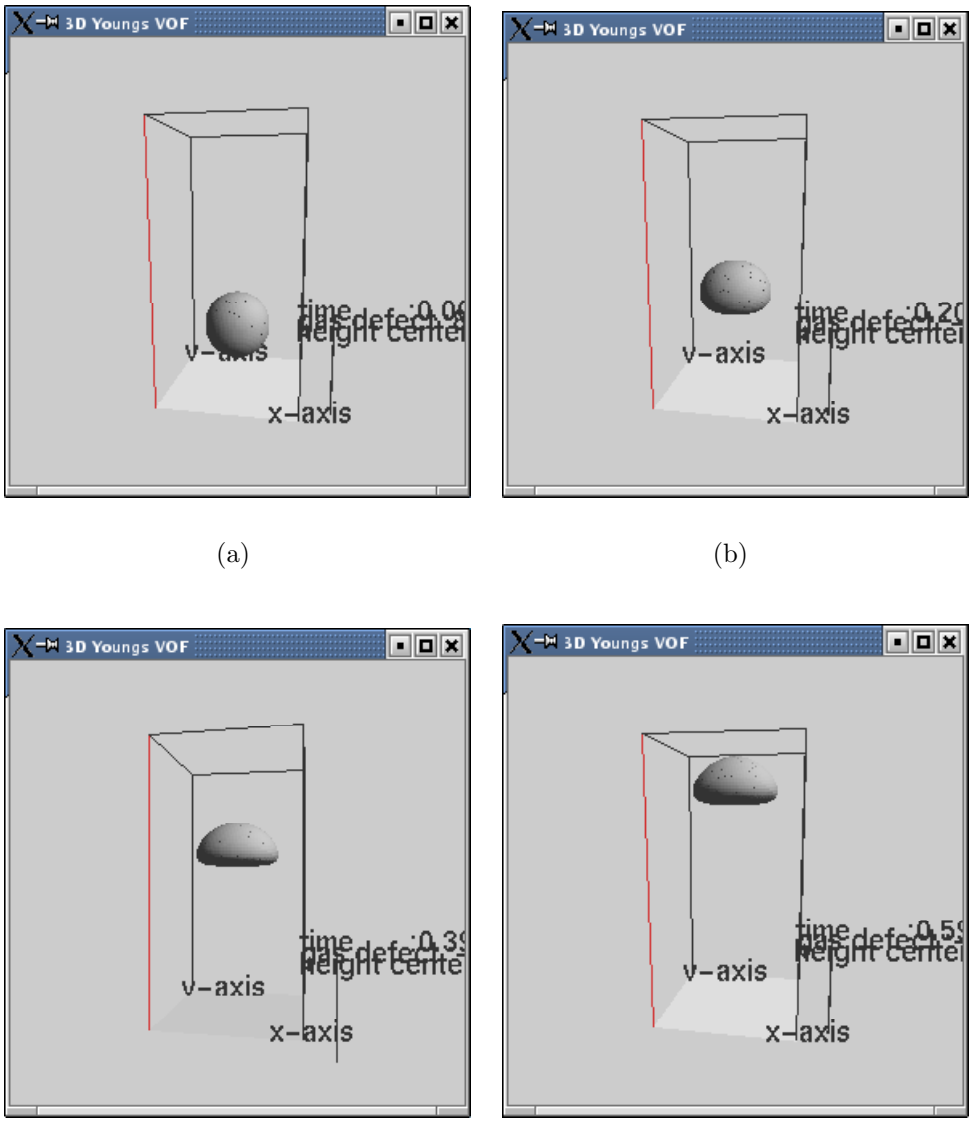

(a) (b)

(c) (d)

Figure 3.12: Results of the stability test using the CSF-model. After (a) 0 s, (b) 0.2 s, (c) 0.4 s en (d) 0.8 s.

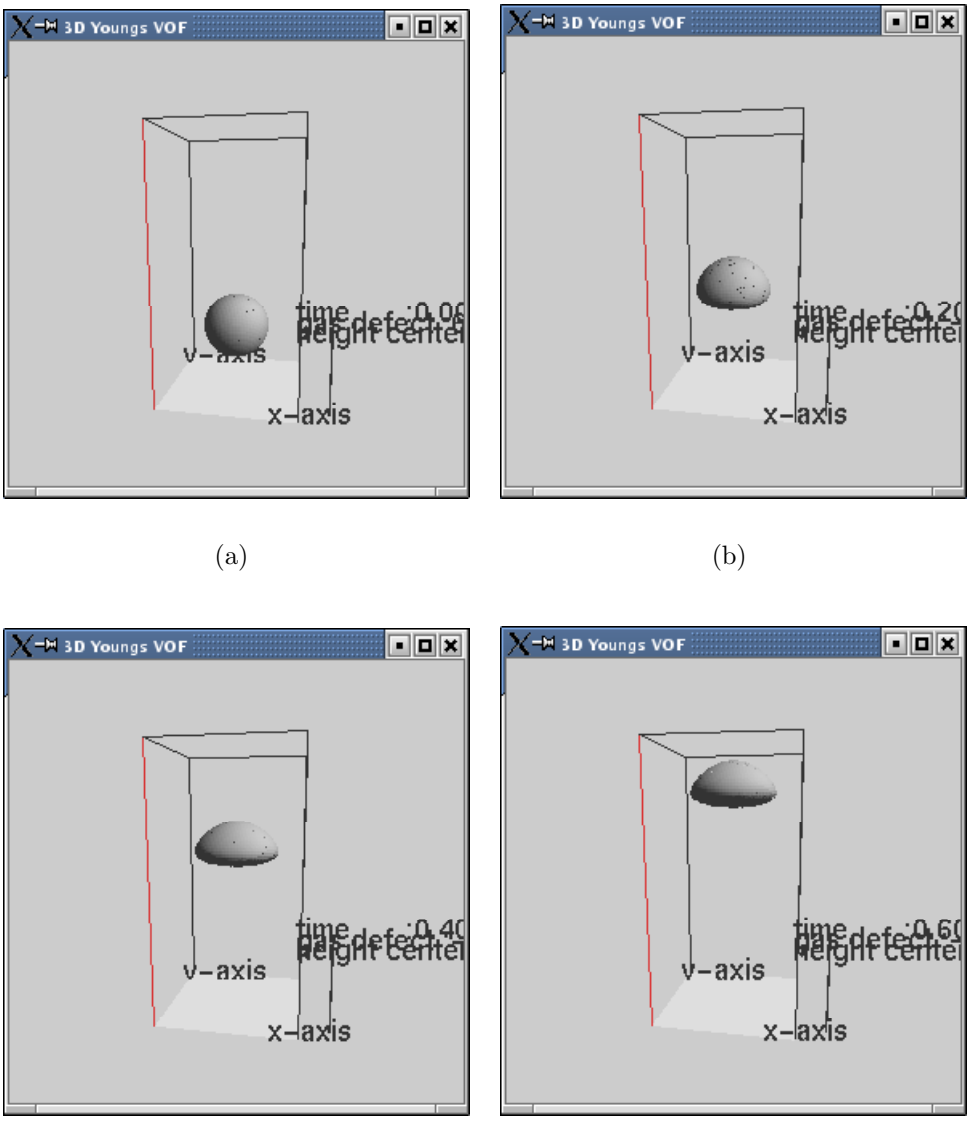

(a) (b)

(c) (d)

Figure 3.13: Results of the stability test using the new surface tension force model. After (a) 0 s, (b) 0.2 s, (c) 0.4 s en (d) 0.8 s.

Table 3.3: Physical and numerical data used in the stability tests.

bubble diameter	d_{eq}	$0.025\ m$
dimensionless numbers	$\log(Mo)$	-3.7
	Eo	12.3
liquid phase	ρ	$1000\ kg/m^3$
	μ	$0.1\ Pa.s$
gas phase	ρ	$800\ kg/m^3$
	μ	$0.1\ Pa.s$
	σ	$0.1\ N/m$
column	number of cells	$50 \times 50 \times 100$
	dimensions	$0.05 \times 0.05 \times 0.1\ m^3$

3.4.4 Verification of surface tension force model: prediction of the interior excess pressure of a spherical bubble

Surface tension forces induce an excess pressure inside a bubble which for a spherical bubble can be calculated from the Youngs-Laplace equation:

$$\Delta p = \frac{2}{r}\sigma \tag{3.18}$$

In figure 3.14 the pressure distribution in a horizontal plane through the computational domain at the height of the centre of the bubble is given and compared to the analytical solution. The excess pressure inside the bubble is predicted very accurately. The calculation results for the large bubbles show a small discrepancy with the analytical solution. The absolute value of this error is in the order of only a few Pascal. This small differance could be attributed to a small incertainty in the analytical value for the excesspressure, since this requires the far field pressure.

In the simulations which will be described in the subsequent chapter the new surface tension force model has been used.

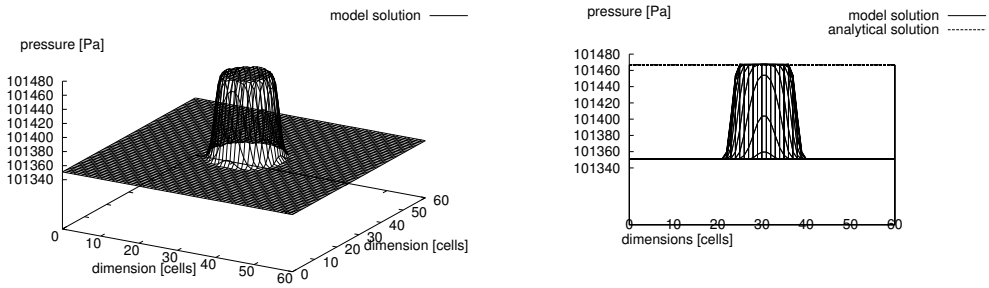

(a)

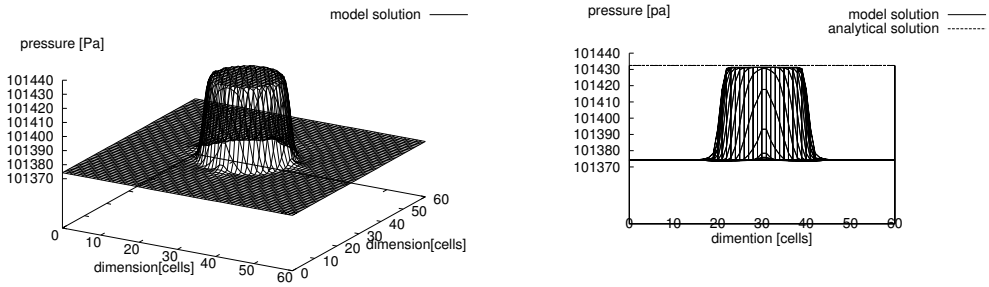

(b)

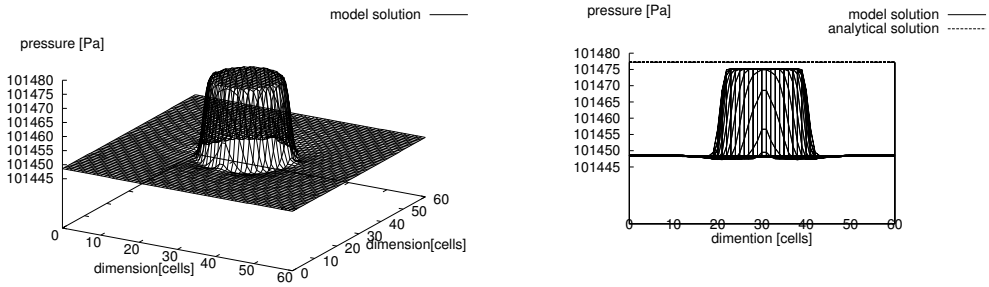

(c)

Figure 3.14: Pressure distribution across the computational domain in a horizontal plane through the centre of a spherical air bubble in water for different bubble diameters, using a constant number of grid cells (60×60×60). (a) $d_{eq} = 2.5\ mm\ L = 7.5\ mm$, (b) $d_{eq} = 5.0\ mm\ L = 15.0\ mm$ and (c) $d_{eq} = 10.0\ mm\ L = 30.0\ mm$.

3.5 Conclusions

A three dimensional *VoF*-algorithm, following the approach originally proposed by Youngs (1987), was successfully implemented in a computer code which is capable of predicting the behaviour of multi-fluid flow problems accurately. The pressure Poisson equation resulting from the one-fluid approach was solved with a robust ICCG matrix solver, even for systems with very high density ratios.

The well known *CSF* model (Brackbill et al., 1992) to calculate the surface tension force has been replaced by a new method. The novel method, inspired by *Front Tracking* models, is based on the calculation of the local pull forces acting between adjacent elements thereby avoiding the computation of the curvature. The undesired parasitic currents are much smaller when using this new method offering the opportunity to describe the behaviour of bubbles with a larger value for $\kappa\sigma$ (i.e. smaller bubble diameter or higher surface tension). The predicted excess pressure inside a spherical bubble agrees very well with the Youngs-Laplace equation, indicating that the algorithm accurately calculates the surface tension forces, provided that the normal vector to the interfaces is evaluated with the smoothed indicator function $\tilde{f}(\mathbf{x})$. This also results in a much better connectivity of the adjacent surface elements. Furthermore, $\tilde{f}(\mathbf{x})$ is also used to evaluate the local density and viscosity improving the prediction of, the velocity and pressure distribution in the vicinity of the interface, thereby enhancing the numerical stability.

Usage of the Rider and Kothe correction (Rider and Kothe, 1998) for a non-divergence free velocity field resulted in an even more rigorous mass conservation.

The fluid velocity near the interface is tempered when applying Prosperetti's approach (Prosperetti, 2001) to compute the local viscosity. This method uses the harmonic averaging of the kinematic viscosity which has a sound physical basis and is preferred over the linear weighing that is often applied. The higher viscosity near the interface resulting from Prosperetti's approach seems to have a stabilising effect on the interface dynamics.

In the validation section it was shown that a minimum of about 20 Eulerian grid cells contained within the bubble in each spatial direction is required to yield reasonably accurate predictions of the bubble shape, rise velocity and bubble dynamics. If the distance, counted in computational cells, between

two facing interfaces is much smaller, the mass of the bubble is over-predicted because the smoothing functions, used to evaluate the density, start to overlap each other.

The use of a non-conservative formulation of the Navier-Stokes equations in combination with a very small time-step opens the possibility to compute two-fluid systems with arbitrarily high density ratios.

The standard advection test of Rider and Kothe (1998) and the stability tests give good confidence that our *VoF* implementation gives accurate predictions of the gas and liquid fluxes and runs stable for long simulation times.

Chapter 4

Comparison of detailed models to experimental data

Abstract

Detailed computations using the *Front Tracking* model and the *VoF* model were compared to experimental data from literature and experimental data from ultrasound measurements. Several computations were carried out and all simulations were started with a spherical bubble in a stagnant liquid. While accelerating to their terminal rise velocity, the bubbles deformed to their final shape. The shape of the bubbles were compared to the bubble shapes predicted by the bubble diagram of Grace (1973). Terminal rise velocities were compared to closure relations taken from Clift et al. (1978) and Tomiyama (1998).

An ultrasound experimental technique was developed by *CORUS RT&D* specifically to study bubbles rising in liquid metals. The terminal rise velocity of argon bubbles rising in liquid aluminium was measured and compared to simulation results from the *VoF* and the *Front Tracking* model.

In the simulations, realistic values for the physical parameters of the gas and the liquid were used. The bubble shapes were in good agreement with those reported in the bubble diagram up to an Eötos number of about 40. The terminal rise velocity of small bubbles (Eö$<$ 0.3) was under-predicted by both models. Therefore the limits for which the current implementation

of these models yield results with good accuracy are thought to be in the range of $0.3 < \text{Eö} < 40$. The simulations that were carried out between these boundaries show a reasonably good agreement in the rise velocities, bubble shape and bubble dynamics as compared to those predicted by the closure relations and the bubble diagram. It was shown that the size of the computational domain did not influence the results.

The rise velocity of the smaller bubbles is probably affected by parasitic currents and therefore under-predicted. Parasitic are currents of numerical nature that occur near the interface of a bubble and is related to the surface tension forces. The simulations of the larger bubbles can probably be improved by using finer meshes or more realistic specialised start-up conditions.

The differences between the *Front Tracking* model and the *VoF* model were analysed. In most cases the *Front Tracking* model predicts a slightly lower terminal rise velocity than the *VoF* model. The *VoF* model also shows a more dynamic behaviour of the interface. It was tested if the relative large loss of gas volume in *Front Tracking* (as compared to *VoF*) could account for this effect, but since the gas loss in our simulations was below about 2% this was not the case. Both effects can probably be attributed to the different techniques used to compute the local velocity at the interface.

The experimental results obtained for liquid bubbles rising in liquid aluminium, from the ultrasound measurements gave very detailed data on the bubble growth, the bubble acceleration and the terminal rise velocity. Information about the bubble shape could not be obtained with this method. The high density ratio and the high surface tension of this system are often hard to handle in numerical codes but proved to be no problem in this work. When the bubble shape is deduced from the bubble diagram (Grace (1973)), the bubble is most probably in the wobbling regime[1]. The simulation results also showed a bubble in wobbling motion with a terminal rise velocity that was within the measurement accuracy of the experiments. It is concluded that both the *Front Tracking* model as well as the *VoF* model are well capable of simulating gas bubbles in high density liquids and with a very high surface tension.

[1]The bubble diagram includes no experimental data at this location in the graph.

4.1 Introduction

Bubble columns are gas-liquid contact devices that are frequently applied in (bio-)chemical reaction engineering because of their relative ease of construction, simple operation, and good heat and mass transfer characteristics. To simulate the behaviour of this apparatus, several mathematical models have been developed. To validate these mathematical models, data obtained from simulations using these models should be compared to experimental data. Once the models have proven to generate sufficiently accurate results, the mathematical models can be used as predictive tools. This would greatly enhance the development of bubble columns.

In this chapter, data obtained from simulations with the *VoF*-model and the *Front Tracking*-model that were described in the previous chapters, are compared to experimental data. First, the models will be compared to a wide range of experimental data taken from literature (Grace (1973), Clift et al. (1978) and Tomiyama (1998)). Second the models will be compared to a specific case, i.e. argon bubbles rising in liquid aluminium. Doing measurements under these exceptional conditions required the development of a new experimental technique. *CORUS-RD&T* has developed an ultrasound method that was able to conduct these measurements. The experimental technique, the experiments and the results will be addressed shortly in this chapter and will be compared to numerical results of the two mathematical models.

Visualisation of the simulation results pertaining to the *Front Tracking* model are represented in C. Visualisations of the *VoF* model results are shown in appendix D.

4.2 Comparison of detailed models to experiments reported in literature

4.2.1 Bubble shape and dimensionless numbers

Grace (1973) has compiled a large variety of experimental data together and it was shown that all these data fit into one figure, when an appropriate set

of dimensionless numbers is used. A copy of this graph, taken from Clift et al. (1978) is reproduced in figure 4.1. Grace (1973) used the dimensionless Morton (Mo), Eötvos (Eö) and Reynolds (Re) numbers, which are defined by

$$\mathrm{Mo} = \frac{g\mu_l^4 \Delta\rho}{\rho_l^2 \sigma^3} \tag{4.1}$$

$$\mathrm{Eö} = \frac{g\Delta\rho d_{eq}^2}{\sigma} \tag{4.2}$$

$$\mathrm{Re} = \frac{\rho_l v_\infty d_{eq}}{\mu_l} \tag{4.3}$$

where the effective diameter d_{eq} is defined as the diameter of a spherical bubble with the same volume as the bubble under consideration.

In the Morton number, viscous forces are related to the surface tension. The Eötvos number is the ratio of a Weber to a Froude number, and is a measure of the relative magnitude of the gravity and the interfacial tension forces. The Reynolds number is a measure for the terminal rise velocity. Certain regions within the graph can be connected to a specific bubble shape. Spherical bubbles are found in the left bottom corner while spherical cap bubbles are found in the right top corner.

This graph is less suitable for obtaining exact data, since all the axes have logarithmic scales. The qualitative indication of the bubble shape and approximate velocity is reasonable accurate and therefore it is very useful for a first evaluation of simulation results.

4.2.2 Correlations for the terminal rise velocity

Usually, the experimentally determined rise velocities have been fitted via the drag force F_d and the drag coefficient C_d, defined as

$$F_d = \frac{1}{2} C_d \rho_l \pi R_b^2 \left|\mathbf{v} - \mathbf{u}\right| (\mathbf{v} - \mathbf{u}) \tag{4.4}$$

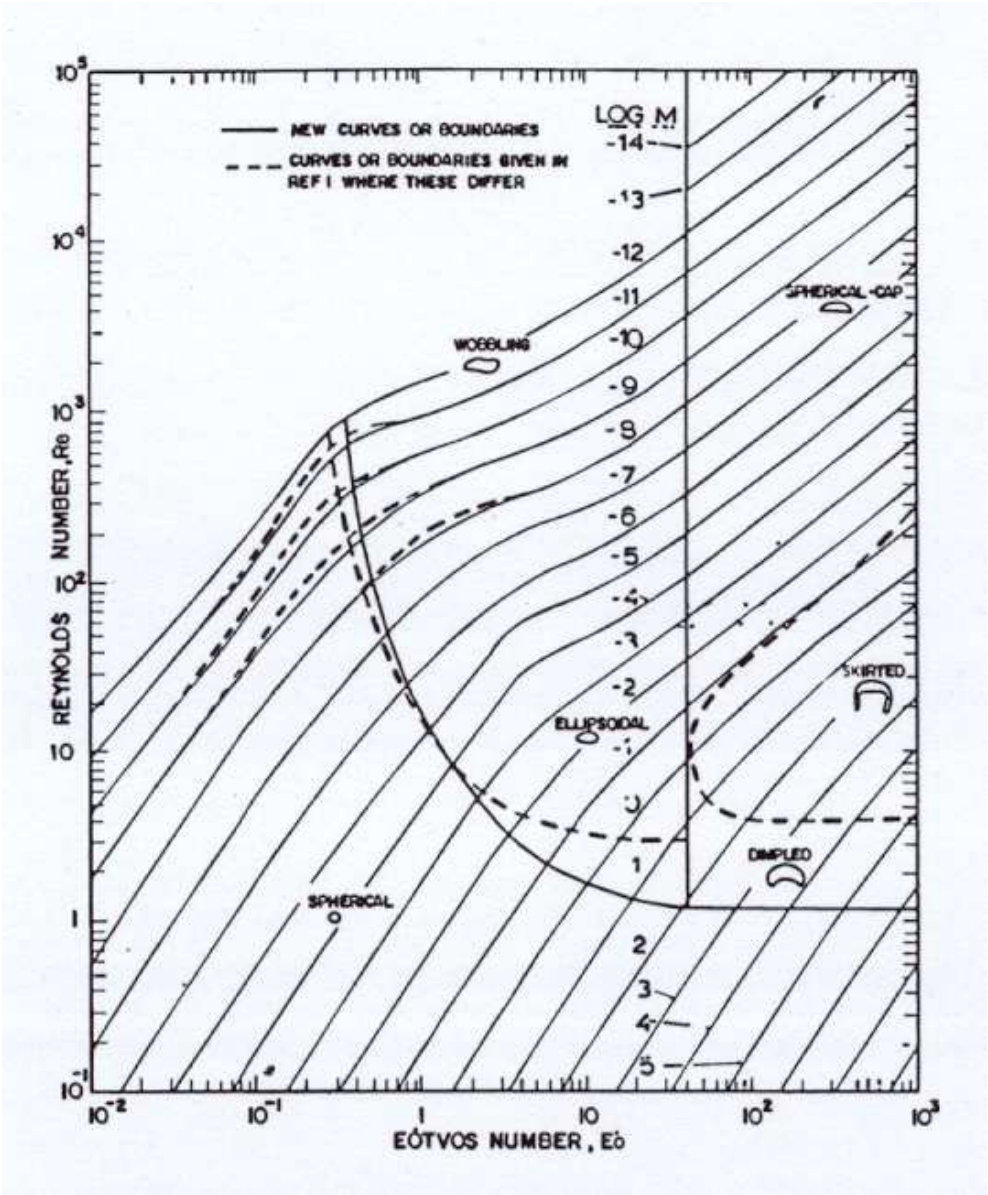

Figure 4.1: Bubble diagram. Taken from Clift et al. (1978).

Clift et al. (1978) and Tomiyama et al. (1998) reported a number of frequently used relations. Clift et al. (1978) give different correlations for the drag force coefficient C_d that are valid for spherical bubbles.

The first closure taken from Clift et al. (1978) is a fit to numerical data and is given by

$$C_d = 14.9Re^{-0.78} \tag{4.5}$$

This relation can be applied to gas bubbles, up to a bubble Reynolds number $Re = 300$.

A second equation, also reported by Clift et al. (1978), is obtained from error distribution (or Galerkin) methods and is given by

$$C_d = \frac{3.05\left(783\kappa^2 + 2142\kappa + 1080\right)}{\left(60 + 29\kappa\right)\left(4 + 3\kappa\right)} Re^{-0.74} \tag{4.6}$$

where κ is defined as μ_{gas}/μ_{liquid}. This relation can be applied in the range of $4 \leq Re \leq 100$.

Also for ellipsoidal and spherical cap bubbles Clift et al. (1978) give equations for the terminal rise velocity. For ellipsoidal air bubbles in pure water equation 4.7 was developed. This function is applicable in the range $0.15 \leq Eo \leq 40$.

$$U_\infty = \left(\left(\frac{2.14\sigma}{\rho_l d_{eq}}\right) + 0.505 g d_{eq}\right)^{0.5} \tag{4.7}$$

and for spherical cap bubbles the following equation was derived:

$$U_\infty = \frac{2}{3}\sqrt{g d_{eq}\frac{\Delta\rho}{\rho_l}} \tag{4.8}$$

Both functions only apply to air bubbles rising in water. This limitation has to be kept in mind when comparing these data to the numerical results.

Tomiyama et al. (1998) proposed a single equation that is valid for the complete range of bubble diameters and physical properties. The correlation for

C_d is based on a fit of experimental data taken from Grace (1973). Following Tomiyama et al. the drag coefficient can be computed by:

$$C_d = \max\left(\min\left(\frac{A}{Re_b}\left(1 + 0.15Re_b^{0.682}\right), \frac{3A}{Re_b}\right), \frac{8}{3}\frac{Eo}{Eo+4}\right) \tag{4.9}$$

4.2.3 Simulations: set-up and results

Using the *VoF*-model and the *Front Tracking*-model, that were described in the previous chapters, simulations were carried out that were compared with the above mentioned closure relations. Initially, a spherical bubble was positioned in a stagnant liquid under hydrostatic pressure. The computational domain was taken to be three times the diameter of the bubble in all directions and the mesh was chosen to be 60 cells in all directions.

During the simulation the flow field surrounding the bubble develops and the bubble shape changes. Typically the bubble accelerates gradually to its terminal rise velocity. Sometimes it is observed that occasionally bubbles slow down slightly due to a change in the bubble shape.

In subsequent sections the simulation results will be discussed in more detail. In figure 4.2 typical simulation results from both models are shown.

4.2.4 Spherical bubbles

Both methods were applied to compute four different bubbles that were all in the region of the Grace diagram of spherical bubbles. The physical properties that were applied during these simulation are summarised in term of the dimensionless Eö and Mo numbers and are given in table 4.1. This table also gives references to figures from the simulation results summarised in the appendixes.

The bubble shapes as presented in these figures show a more or less spherical shape. In both models, simulations of bubbles with a high surface tension, show a less smooth interface. Nevertheless, the spherical shape is conserved.

In table 4.2 the bubble Reynolds number at the terminal rise velocities of the bubbles are compared to Reynolds numbers evaluated from the closure

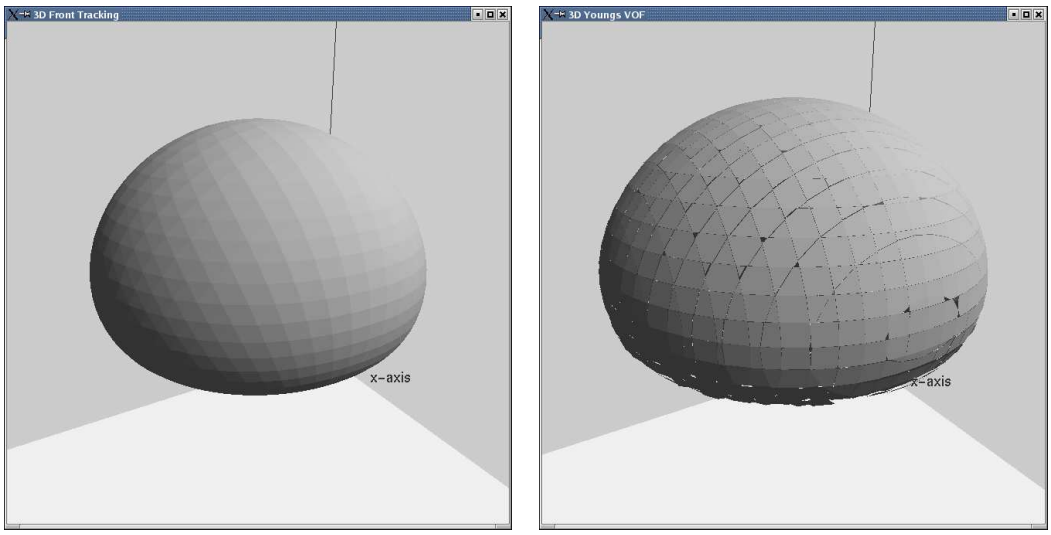

(a) (b)

Figure 4.2: Examples of different bubble shapes as computed by the *Front Tracking* model (a) and the *VoF* model (b). The dimensionless numbers for both bubbles are : Eö $= 10$, $\log(Mo) = -5.24$, but are taken after a different simulation time. figure (a) was taken after 0.1 s while figure(b) was taken after 0.3 s.

relations given in the previous section. The terminal rise velocity is obtained

Table 4.1: Dimensionless numbers of numerical experiments of (practically) spherical bubbles and references to the figures of the simulation results.

			Front Tracking	*VoF*
case	Eö	$\log(Mo)$	page/figure	page/figure
1	0.1	-8.6	147/ C.2	
2	0.1	-10.6		154/D.1
3	1.0	-1.8	147/ C.3	154/D.2
4	1.0	-3.8	148/ C.4	155/D.3
5	10.0	5.0	148/ C.5	155/D.4

Table 4.2: Reynolds number for the simulated bubbles rising at their terminal rise velocity compared to data from literature.

case	Eö	$\log(Mo)$	*VoF*	*Front Tracking*	eqn. 4.5	eqn. 4.6	eqn. 4.9
1	0.1	-8.6	-	8.48	28.00	27.70	42.30
2	0.1	-10.6	$+/-85$	-	179.35	160.73	184.48
3	1.0	-1.8	1.09	0.82	-	-	1.02
4	1.0	-3.8	8.15	6.41	5.21	5.27	5.83
5	10.0	5.0	0.11	0.130	-	-	0.055

from the velocity graphs that are included in the appendices.

A point of concern is the validity of the closure relations. Equation 4.5 and 4.6 both have a lower limit at $Re = 2$ and $Re = 4$ respectively. These equations are therefore not applicable for the third and the last simulation.

The Reynolds numbers computed by the models for the first two simulations are far lower than the Reynolds numbers predicted by the closure relations. This is probably due to parasitic currents near the interface. Parasitic currents result from the numerics of the computation. They occur at interfaces with a high surface tension or curvature. From the figures in the appendices it can be seen that the interface of these bubbles is non-smooth, indicating local currents near the interface. The circulating nature of these currents can suppress the motion of the bubble resulting in a lower rise velocity.

The computed Reynolds numbers for case 3 and 4 are slightly higher than those evaluated from the closure relations. The Reynolds numbers resulting from the *VoF*-simulations are, except for the last one, slightly higher than those obtained from the *Front Tracking* simulations.

The over-prediction of the Reynolds number is probably related to the method to evaluate local velocity. Both models interpolate the liquid and the gas phase f velocities. Inevitable inaccurcies in the computation near the interface affect interpolated local interface velocity. Since the density of the gas is much lower than the density of the liquid, the gas velocity is very sensitive to small inaccuracies in the momentum balance. The stencil used for the interpolation of the local velocity in the *Front Tracking*-model is wider than the one use in *VoF*. This means that the gas velocity near the interface has a

Table 4.3: Dimensionless numbers of simulation results of ellipsoidal/wobbling bubbles.

			VoF	*Front Tracking*
case	Eö	log (Mo)	page/figure	page/figure
6	1.0	−6.1	149/ C.6	156/D.5
7	1.0	−11.0	149/ C.7	156/D.6
8	10.0	−1.8	150/ C.8	157/D.7
9	10.0	−5.2	150/ C.9	157/D.8
10	10.0	0.6	151/ C.10	158/D.9

larger impact on the local mean velocity evaluated in *VoF*. This could cause the *VoF*-model to predict a slightly higher rise velocities. Further research is needed to elucidate the effect of the interpolation method.

4.2.5 Ellipsoidal/Wobbling bubbles

In the region for which ellipsoidal bubbles or bubbles in a wobbling motion are expected, five simulations were carried out. As in the previous subsection, the physical properties of the bubbles are given as dimensionless numbers. In table 4.3 the Eö and *log*(Mo) numbers of the simulations can be found together with a reference to the figures of the simulation results in the appendices.

The shapes of the bubbles that are presented show a reasonable agreement with the bubble diagram.

Also simulations for bubbles with Eö numbers larger than 40 were tested. During the deformation of these bubbles the rear end of the bubbles was moved so far into the bubble that the rear interface touched the leading interface. In the simulation using the *Front Tracking*-model this resulted in a torus with a thin double interface at the top. In *VoF*-simulations this resulted in a break up of the interface leaving a torus shaped bubble that in most simulations broke down in four smaller bubbles. An explanation for this problem could be related to the somewhat artificial start-up conditions of the simulations. When a bubble accelerates it has to pass through several

Table 4.4: Reynolds numbers as computed using *Front Tracking* of *VoF* compared to Reynolds numbers from several closure relations.

case	Eö	log(Mo)	*VoF*	*Front Tracking*	eqn. 4.9	eqn. 4.7
6	1.0	−6.1	50.91	40.73	34.33	54.28
7	1.0	−11.0	1023.26	930.29	890.81	930.90
8	10.0	−1.8	13.27	13.27	12.01	13.76
9	10.0	−5.2	3.58	3.24	1.16	3.41

regimes of Reynolds numbers (going up in the bubble diagram). For these larger bubbles, this path leads through the region where skirted bubbles which have thin tails, are expected. Simulation of these bubbles requires a much higher resolution than applied in this study.

In table 4.4, the Reynolds numbers computed from simulation results of the *Front Tracking*-model and the *VoF*-model are compared to the Reynolds numbers computed from closure relations.

Most of the results are well within the range that is predicted by the two closure relations. Only the computed Reynolds number for the second case is slightly higher. Again the validity of the closure relations should be discussed. Equation 4.7 is derived for bubbles rising in pure water. The second bubble in table 4.4 has its dimensionless numbers close to those of water and is therefore likely to be predicted quite accurately. The Reynolds number of the *Front Tracking* simulation is close to value predicted by this closure equation. Equation 4.9 is, according to the authors, valid for the whole range of dimensionless numbers. The simulation results are in quite reasonable agreement with these figures.

4.2.6 Discussion

The bubble shapes resulting from the simulation show a qualitative agreement with the bubble shapes that are predicted by the bubble diagram (Grace, 1973). The Reynolds numbers resulting from the simulations are mostly in the same range as those predicted from closure relations. Bubbles with a very high curvature have a somewhat lower computed terminal rise velocity than predicted by the closures. Therefore, the lower boundary at

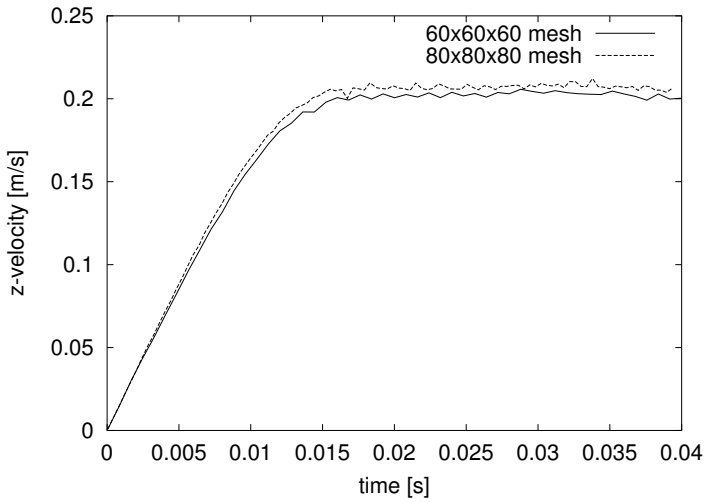

Figure 4.3: Influence of the size of the computational domain on the terminal rise velocity. In both simulations the grid spacing was kept constant $h = 4.1667 \cdot 10^{-4}\ m$. The difference in terminal rise velocity is about 4 mm/s. (Eö = 10, $\log(Mo) = -5.24$).

which, the current implementations of these models, with the chosen resolution, can be applied with reasonable accuracy is about Eö > 0.3. On the other end, bubbles with Eö > 40 showed in-realistic results. This limits the use of these models to $0.3 <$ Eö < 40.

In addition, it was checked whether the size of the domain significantly effects the terminal rise velocity. Due to the hindering of the downward liquid flow the bubble rise velocity could be decreased. In figure 4.3 the influence of the computational domain is shown. Although a larger domain results in a slightly higher rise velocity the difference is small.

Most of the *VoF* simulations show a higher Reynolds number than the *Front Tracking* simulations. It was checked if loss of gas volume during the *Front Tracking* computation effected the rise velocity. If in *Front Tracking*, the bubble volume would decrease very rapidly, this could be a reason for the decrease in terminal rise velocity. (see for example the bubble diagram: if the Eötvos number decreases, the Reynolds number decreases also). The gas loss in the simulations using the *Front Tracking* model never exceeded 2 %

of the initial gas volume. This decrease is not sufficient to account for the differences observed between the two models and therefore this hypotheses should be rejected.

A final explanation can be found in the method that was applied to evaluate the local velocity at the interface. This was already mentioned before. Since this can explain both the over-prediction of the Reynolds number of both models, as compared to the closure relations, and the difference between the models it is the most likely reason for the observed discrepancies.

Simulation results show a second difference between the *Front Tracking* and the *VoF*-model. If a sequence of images is produced, the bubble interfaces have different dynamics with both the models. Using *Front Tracking*, almost no interface dynamics is observed, while the *VoF* simulations show more interface dynamics. The absence of the dynamics in the *Front Tracking* model is most probably a result of the interpolation scheme used to compute the local velocity of the marker points. This is done using a large stencil that is likely to filter numerical disturbances. In *VoF*, the volume fluxes through the cell faces are computed using the velocity at the position of the staggered nodes, without interpolation, resulting in an immediate reaction of the interface structure to small fluctuations in the velocity field in the vicinity of the interface.

Concluding, both the models can be applied in a wide range of Eötvos numbers in the range $0.3 \leq \text{Eö} \leq 40$. For Eötvos numbers smaller than 0.3, parasitic currents influence the fluid flow to such an extent that an accurate prediction of the terminal rise velocity can no longer be obtained. For Eötvos numbers exceeding 40, the bubbles started from their initial spherical shape and deform to unrealistic torus-like bubbles. In *Front Tracking* this results in a very thin interface at the top of the bubble. In *VoF* this interface breaks up and a real torus is created. The break-up in *VoF* is due to the numerical method and has no sound physical basis. A possible solution could be to use a refined mesh. If the mesh is sufficiently small no break-up will occur. For a realistic modelling of the break-up process however a break-up algorithm should be implemented.

4.3 Comparison of experimental data on liquid aluminium to computed results

4.3.1 Introduction

Liquid metals like liquid aluminium or liquid iron are very hard to handle because of their melting temperatures (about 750^oC and 1500^oC respectively). Measurements in these liquids are therefore difficult to perform. In order to get insight in the behaviour of gas bubbles in these liquids, *CORUS RD&T* developed a new measuring technique that enables monitoring of the vertical position of a bubble interface in these metals. In the next section the technique will be addressed briefly and in the subsequent sections the measured data are compared to computational results from both *Front Tracking* and *VoF* models.

4.3.2 Experimental method

The newly developed technique uses ultrasound signals to detect the interface of the bubble. A first probe, the transmitter, sends an ultrasound signal into the liquid. The signal is reflected on the bubble interface and a second probe, called the receiver, picks up a returned signal (see figure 4.4). The time difference between the sent and received signal is a measure for the distance of the bubble interface to the probes. In figure 4.5 typical raw data pattern of such an experiment are shown.

The reported experiment was conducted with liquid aluminium. The probes needed in these experiments were especially prepared to withstand the temperatures of molten aluminium. At the wavy liquid interface, a large temperature difference exists that puts heavy demands on the probe material. Further details about the method are given by van Oord et al. (2001).

From the raw data several parameters can be computed. The growth rate for example can be calculated by analysing the slope of the curve in the lower first part of the curves. At this point in the measurement the bubble is still attached to the nozzle. The distance to the probes decreases slowly and is a direct measure for the bubble diameter. Just before the bubble detaches, the final bubble diameter can be obtained. After detaching the

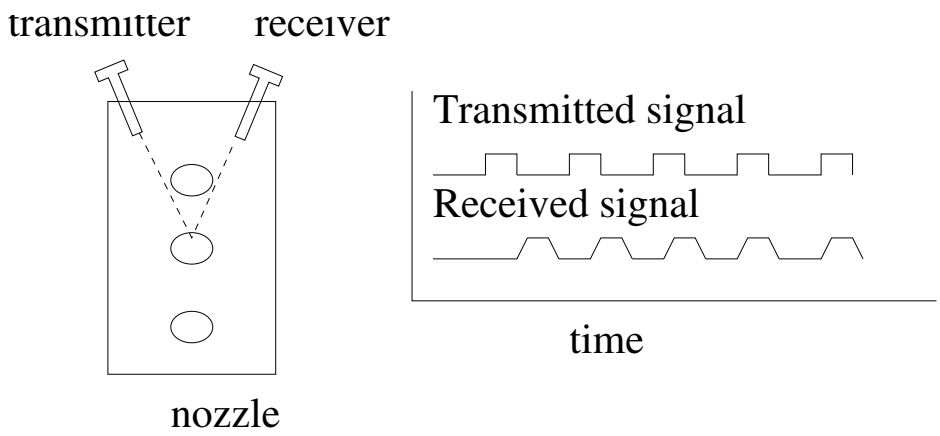

Figure 4.4: The left figure shows schematically the position of the transmitter and the receiver (after van Oord et al. (2001)). The right figure indicates the signals that are sent and received. The distance between the sent signal and the received signal decreases when the bubble comes closer to the transmitters (after van Oord et al. (2001)).

bubble accelerates to its terminal rise velocity. This acceleration phase is measured in the curved part of the data. This acceleration is of interest when studying the closure relations for the virtual mass forces. The terminal rise velocity can be computed from the steep gradient in the last part of the curves and is computed by dividing the displacement by the time. From the number of peaks, time and the gas flow rate the mean volume of the bubbles can be obtained.

4.3.3 Experimental data

From the graph shown in figure 4.5 it can be seen that 10 bubbles were released in 16 seconds, one bubble every 1.6 s. The gas flow rate used in this experiment was 1.0 $l/h = 2.77 \cdot 10^{-7}$ m^3/s. Therefore the mean bubble volume is $4.43 \cdot 10^{-7}$ m^3, which means that the mean equivalent bubble diameter is $9.3 \cdot 10^{-3}$ m.

The terminal rise velocity that was computed from this figure lies between 0.35 and 0.40 m/s. The bubble diameter (as obtained from the lower part of

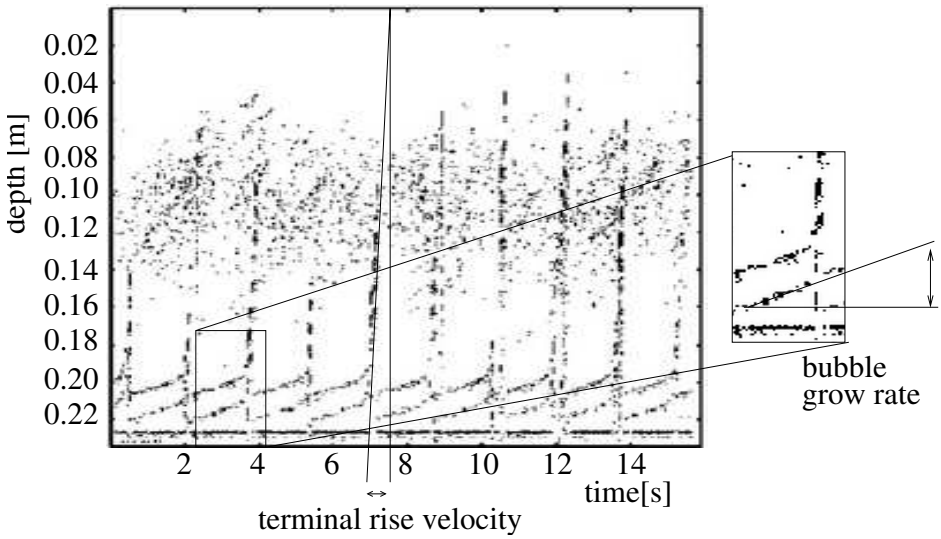

Figure 4.5: Raw data of an ultrasound measurement in liquid aluminium with a gas flow of 1 l/h. On the vertical axis the distance from the bubble to the transducers is given. Each peaks represents a single bubble. From these peaks the terminal rise velocity can be evaluated. The zoomed picture on the right, shows how to obtain the bubble grow rate from this graph.

Table 4.5: Physical properties of liquid aluminium at 930 K.

σ	$0.9\ kg/s^2$
ρ	$2.68 \cdot 10^3\ kg/m^3$
μ	$1.1 \cdot 10^{-3}\ kg/m.s$
ν_{sound}	$4650\ m/s$

the curves) is about $1 \cdot 10^{-2}\ m$ which is in good agreement with the result of the previous calculation of the mean equivalent bubble diameter.

4.3.4 Simulation results

Initial settings of the simulation

Both the *VoF* and the *Front Tracking* models were used to simulate this experiment. The model parameters that were applied are: a $60 \times 60 \times 60$ cells Eulerian grid, $l \times w \times h = 0.03\ m \times 0.03\ m \times 0.03\ m$ with a moving window, this means that the computational domain is shifted with the bubble to keep the centre of mass of the bubble in the centre of the computational domain. The initial bubble with diameter $9.8 \cdot 10^{-3}\ m$ is placed in the middle of the box. Physical properties of aluminium can be found in table 4.5. The simulated time was $0.1\ s$. The computation took about 8 days on a $1.8\ Ghz$ AMD personal computer.

Computational results

In figure 4.6(a) the x and z coordinate of the centre of mass of the bubble calculated by the VOF and *Front Tracking* model are shown (the y coordinate is left out for readability of the graph). In figure 4.6(b) the rise velocity of the bubble as a function of time is shown. The rise velocity of the *VoF* computation is slightly higher than the one computed by the *Front Tracking* model. A small part, about 2 %, of this difference can be accounted for by the loss of gas volume in the *Front Tracking* model but this value is too small to account for the entire velocity difference. *VoF* predicts a much more dynamic bubble interface compared to the *Front Tracking* model. This was

already discussed in section 4.2.6. From the bubble diagram of Grace (Grace, 1973), it can be concluded that a dynamic behaviour of the argon bubble in aluminium is to be expected and that the *Re* number is in the correct range. Since the Morton number for this liquid gas system is way out of range of this diagram only the trend can be compared.

The terminal rise velocity determined from the ultrasound experiments for this bubble is in between 0.35 and 0.40 m/s. The dynamic behaviour of the bubble interface simulated by the *VoF* model has a large impact on the velocity graph resulting in a large degree of freedom for this parameter. It is not clear if the *Front Tracking* model will start wobbling after longer simulation times. The velocity computed by the *VoF* simulations is around 0.40 m/s. The velocity computed by the *Front Tracking* model approaches this value.

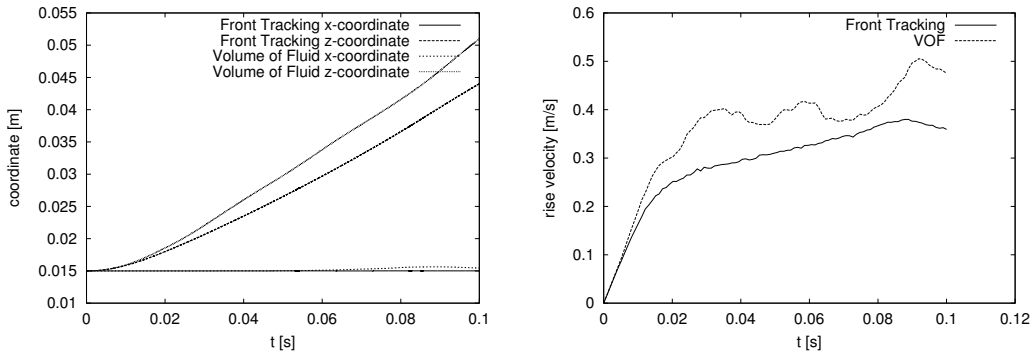

(a) (b)

Figure 4.6: Rise velocity (a) and x and z coordinate (b) of an 0.98 cm argon bubble in liquid aluminium. Dimensionless numbers Eö= 2.75, $\log(Mo) = -14$

4.3.5 Discussion

The simulations show for both models a rapid acceleration from 0 to about $0.2 - 0.3\ m/s$ whereafter the acceleration slows down. *Front Tracking* shows a increase of the velocity till about 0.08 s, while the *VoF* simulation shows a

more chaotic gradual acceleration, however with periods of acceleration and deceleration. This is due to the more pronounced wobbling motion predicted by the *VoF* model. This wobbling motion can also be seen in an animation of the numerical results. The *Front Tracking* model does not show this motion.

The models both predict the terminal rise velocity of the bubble reasonable accurately. The terminal rise velocity predicted by *VoF* is somewhat higher than the one predicted by *Front Tracking*. This could be due to the dynamic behaviour of the interface in *Front Tracking*.

4.4 Conclusion

The simulations using the *Front Tracking* model and the *VoF* model were compared to experimental data. Both models give similar and reasonable accurate results for the bubble shape as well as the terminal rise velocity. Even the very special case of an argon bubble rising in liquid aluminium (with an exceptionally high surface tension) could be simulated with a reasonable accuracy.

It was also shown that both models have their own advantages and disadvantages. The *Front Tracking* model is very stable but shows some loss of gas volume. Due to its stability it did not start to predict the wobbling motion. This motion could start after longer simulation times. Gas loss in simulations with the *VoF* method was negligible small , but this method shows a bubble interface that reacts strongly to small velocity deviation near the interface.

From the comparison with the experimental data none of the models shows to be significantly more accurate than the other.

Chapter 5

Discrete bubble modelling

Abstract

Discrete bubble models were introduced in the 1990's by Trapp and Mortensen (1993), Lapin and Lübbert (1994) and Delnoij et al. (1997). These models are very useful in predicting the local bubble 'collision' frequentcy from which, the bubble size distribution can be calculated with proper closures for coalescence and break-up. This size distribution has a major impact on e.g. the flow field and the mass transfer. In the present work the deterministic Euler-Lagrangian model, which was originally developed by Delnoij (1999), was improved on numerous aspects.

The new features include state of the art closure relations for the forces actinf on the bubbles and detailed treatment of the bubble-bubble interaction, by accounting for collision of bubble pairs. The original three dimensional, two way coupled model has evolved to a full four way coupled model. The description of the continuous phase now includes a (very) large eddy simulation (LES) model to account for sub-grid scale turbulence. The original up-wind discretisation scheme was replaced by a second order accurate Barton-scheme.

All modifications to the original model were tested separately and simulations were carried out to show the effects of the new elements. Finally, the numerical results were compared to experimental data taken from PIV measurements for a relative high superficial gas velocity (5 mm/s).

The replacement of the up-wind scheme only marginally changed the simulation results. The LES reduced the vertical liquid velocity and narrowed the range of the standard deviation values indicating a less dynamic flow pattern. Introduction of new closure relations effected the mean position of the bubbles. The bubble plume narrowed and the velocity near the plume increased consequently. By introducing full four way coupling, we were able to increase the maximum gas load and this enabled us to simulate bubble columns with superficial gas velocities up to at least 15 mm/s with local gas fractions up to about 40 %.

A reasonable resemblance between numerical and experimental data was found in the more homogeneous sections of the bubble column. In the lower parts of the column where the bubbles are located near the central axis of the bubble column, the velocities of both the liquid and the gas phase are over predicted. This is probably caused by the fact that the implemented closure relations were not derived for very high gas fractionis. Further research is needed to investigate this.

5.1 Introduction

In many processes encountered in the chemical, biological or metallurgical industry, dispersed gas-liquid flows prevail in several types of devices such as spray drying or cooling towers, evaporators, fermentation reactors, and bubble and slurry columns. In this study we focus on the numerical modelling of bubble columns. Bubble columns find a widespread application in industry because of their low operating costs and their good mixing and heat transfer characteristics. Despite their frequent application, fundamental knowledge of bubble column behaviour is still lacking.

Detailed hydrodynamic models can provide insight into the fundamentals of bubbly flow and can direct experimental work and limit the extent to which experimental work is required.

Hydrodynamic models for bubbly flows can focus on a number of length and time scales in the flow. The more detail is required the more computational effort is needed. Flows in industrial scale devices can now be simulated using Euler-Euler models that treat the different phases as inter-penetrating fluids. Euler-Lagrangian models can be considered as the next level of detail.

A number of variants of these models exist. In stochastic Euler-Lagrangian models a number of size classes is distinguished and a few representative particles of each class are tracked. In this study a deterministic Euler-Lagrangian is used. Deterministic models follow each bubble individually. This allows a very detailed treatment of all the encounters between bubbles even at a very high gas loading. This model is also referred to as the *Discrete Bubble Model* (*DBM*).

Both Euler-Euler models and Euler-Lagrange models need closure relations to account for the phenomena at sub-grid scale level (e.g. the influence of the bubble shape) that are not resolved. Since these relations are of empirical nature and are incompletely understood, this is still a disadvantage of those models.

Bubble formation, bubble shape and bubble dynamics on the level of a single or a few bubbles can be studied in great detail using detailed models like *VoF* or *Front Tracking* (Chapters 2 and 3). These models can also be used to study and derive the closure relations needed by the Euler-Euler or Euler-Lagrangian models.

In this chapter the *DBM* model developed by Delnoij (1999) will be extended. The continuous phase flow model was improved by adding an LES model and a second order accurate Barton scheme for the convective fluxes. Closure relations for the drag, lift and wake force, proposed by Tomiyama et al. (1998), were implemented.

To validate the model, the simulation results were compared to experimental data. These data were obtained using a two-camera *Particle Image Velocimetry* (*PIV*) technique. This technique can capture the motion of the continuous liquid phase and the discrete gas phase simultaneously which has the advantage that the data for both phases originate from the same experiment.

The first half of this chapter describes the mathematical model, followed by a brief overview of the numerical implementation. In the second half, the effects of the new elements will be shown. Finally the simulation results will be compared to experimental data.

5.2 Model equations

The hydrodynamic model consists of two coupled parts. The first part describes the continuous liquid phase while the second part treats the discrete gas bubbles. The coupling between the gas and the liquid phase is achieved by ensemble averaging of the momentum of the bubbles present in a specific control volume and incorporating these, as source terms into the liquid phase momentum equations. The coupling of the momentum from the liquid to the gas-phase is done via the closure relations. The interaction between bubbles is modelled via an encounter model.

5.2.1 Liquid phase hydrodynamics

The liquid phase is modelled by modified Navier-Stokes equations

$$\frac{\partial\left(\epsilon_l \rho_l \mathbf{u}\right)}{\partial t} + \nabla \cdot \epsilon_l \rho_l \mathbf{u}\mathbf{u} = -\epsilon_l \nabla p - \nabla \cdot \epsilon_l \tau_l + \epsilon_l \rho_l \mathbf{g} + \Gamma \tag{5.1}$$

and the equation of continuity

$$\frac{\partial\left(\epsilon_l \rho_l\right)}{\partial t} + \nabla \cdot \epsilon_l \rho_l \mathbf{u} = 0 \tag{5.2}$$

where ϵ_l indicates the liquid volume fraction and the source term Γ accounts for the momentum exchange between the gas bubbles and the liquid phase. The liquid phase viscous stress tensor τ_l is modelled assuming a Newtonian behaviour of the liquid. (See e.g. Bird et al. (1960))

The viscosity μ used in these equations was taken to be the sum of the molecular viscosity μ_m and the turbulent viscosity μ_t, where the latter was modelled using the Smagorinski model (Sagaut, 2001).

Smagorinski model

Jacobsen (1997) and Deen (2001) did extensive work on the selection and verification of a model that could account for the sub-grid scale turbulence.

Following them, a Smagorinski model was adopted to account for the sub-grid turbulence stresses. In this implementation the minimum mesh size is limited to a couple of bubble diameters. Deen (2001) has proven that even on this scale the LES model is preferred over, for example, the $k\epsilon$-model.

In this LES implementation, the turbulent viscosity μ_t can be evaluated by:

$$\mu_t = \rho_l l_{mix}^2 \sqrt{\frac{1}{2} S_{ij} S_{ij}} \tag{5.3}$$

where S_{ij} represents the (i,j)-th component of the strain rate tensor. The components of S are given by

$$S_{xx} = 2\frac{\partial u_x}{\partial x} \tag{5.4}$$

$$S_{yy} = 2\frac{\partial u_y}{\partial y} \tag{5.5}$$

$$S_{zz} = 2\frac{\partial u_z}{\partial z} \tag{5.6}$$

$$S_{xy} = S_{yx} = \frac{\partial u_x}{\partial y} + \frac{\partial u_y}{\partial x} \tag{5.7}$$

$$S_{xz} = S_{zx} = \frac{\partial u_x}{\partial z} + \frac{\partial u_z}{\partial x} \tag{5.8}$$

$$S_{yz} = S_{zy} = \frac{\partial u_y}{\partial z} + \frac{\partial u_z}{\partial y} \tag{5.9}$$

$$\tag{5.10}$$

The mixing length l_{mix} is related to the grid spacing h by

$$l_{mix} = C_s h \tag{5.11}$$

where C_s is the Smagorinski constant, which approximately equals 0.1.

5.2.2 Bubble dynamics

In our *DBM* all bubbles are tracked individually, where their motions are described by Newton's second law.

$$m_{bubble}\frac{d\mathbf{u}}{dt} = \mathbf{F}_{tot} \tag{5.12}$$

where F_{tot} is the total force acting on a bubble. Several authors reported forces that could influence the motion of the bubbles. A large number of these forces were summarised by Jakobsen et al. (1997). In this work, the contribution resulting from gravity, pressure, drag, lift, wake and virtual mass forces were taken into account. This approach was also taken by Jakobsen and Svendsen (2000).

$$\mathbf{F}_{tot} = \mathbf{F}_g + \mathbf{F}_p + \mathbf{F}_d + \mathbf{F}_l + \mathbf{F}_{wake} + \mathbf{F}_{vm} \tag{5.13}$$

The new velocity and position of the bubble is now computed from respectively

$$\mathbf{v}_{t+1} = \mathbf{v}_t + \frac{d\mathbf{u}}{dt}\Delta t \tag{5.14}$$

$$\mathbf{x}_{t+1} = \mathbf{x}_t + \mathbf{v}_t\Delta t + \frac{1}{2}\frac{d\mathbf{u}}{dt}(\Delta t)^2 \tag{5.15}$$

Gravity and pressure forces

The sum of the gravity and pressure forces are given by the the standard expressions,

$$\mathbf{F}_g + \mathbf{F}_p = \rho_g \mathbf{g} V_b - V_b \nabla p \tag{5.16}$$

where V_b is the bubble volume and p corresponds to the far field pressure.

Drag force

The drag force is often evaluated by:

$$\mathbf{F}_d = -\frac{1}{2} C_d \rho_l \pi R_b^2 \left|\mathbf{v} - \mathbf{u}\right| (\mathbf{v} - \mathbf{u}) \tag{5.17}$$

Delnoij (1999) applied the C_d for rigid spheres, since small spherical air bubbles rising in tap water behave like rigid particles with a low density:

$$C_d = \begin{cases} Re < 1000 & \frac{24}{Re}\left(1 + 0.15 Re^{0.687}\right) \\ Re > 1000 & 0.44 \end{cases} \tag{5.18}$$

Tomiyama et al. (1998) reported a number of other relations for purified and contaminated liquids. In the present study the one for contaminated water was incorporated in the model.

$$C_d = \max\left(\min\left(\frac{A}{Re_b}\left(1 + 0.15 Re_b^{0.682}\right), \frac{3A}{Re_b}\right), \frac{8}{3}\frac{Eo}{Eo + 4}\right) \tag{5.19}$$

where Eo is the Eötvos number and Re_b is the bubble Reynolds number evaluated for the equivalent bubble diameter. The variable A takes a value of 16 for purified liquids and 24 for slightly contaminated liquids. This formulation was adopted in the present model because it is valid over a wide range of bubble sizes and different gas-liquid combinations.

Lift force

The lift force acting on the bubble can be computed from an equation derived by Auton (1983).

$$\mathbf{F}_l = -C_l \rho_l V_b (\mathbf{v} - \mathbf{u}) \times (\nabla \times \mathbf{u}) \tag{5.20}$$

Delnoij (1999) used a C_l value of 0.53, following Auton (1987). Tomiyama et al. (1998) proposed a new function for the lift coefficient obtained from an extensive experimental and computational study.

$$C_l = 0.288 \tanh\left(0.121 Re_b\right) \tag{5.21}$$

This relation takes into account the different behaviour of larger and smaller bubbles if rising in a linear shear flow. Large bubbles move to the high velocity region while small bubbles move towards the low velocity region (Tomiyama, 1998). In the present work this latter formulation was applied.

Wake force

The wake force $\mathbf{F}_{wake}$, accounts for the different sign of the lift force between ridged and deformed particles (Jakobsen and Svendsen, 2000) and is evaluated by a formulation given by Tomiyama et al. (1998):

$$F_{wake} = -C_{wake}\rho_l V_b \left(\mathbf{v} - \mathbf{u}\right) \times \left(\nabla \times \mathbf{u}\right) \tag{5.22}$$

$$C_{wake} = \begin{cases} 0 & \text{for} \quad Eo < 4 \\ 1.05 \cdot 10^{-3} Eo^3 - 0.0159 Eo^2 - 0.00204 Eo + 0.176 & \text{for} \quad 4 < Eo < 10 \\ -0.576 & \text{for} \quad Eo > 10 \end{cases}$$

Since this formulation is similar to the formulation of the lift force, the two constants of both the lift and the wake force can be summed and used in one joint formulation.

Virtual mass force

Following Auton (1983) and Delnoij (1999) the following equation has been adopted to account for the virtual mass force acting on a bubble

$$\mathbf{F}_{vm} = -\left(\frac{D\mathbf{I}}{Dt} + \mathbf{I} \cdot \nabla \mathbf{u}\right) \tag{5.24}$$

where I is given by

$$\mathbf{I} = C_{vm}\rho_l V_b \left(\mathbf{v} - \mathbf{u}\right) \tag{5.25}$$

The value for C_{vm} is taken to be equal to 0.5.

5.2.3 Direct bubble-bubble interaction

In the three dimensional *DBM*-code developed by Delnoij (1999), the bubble-bubble interaction was neglected. Consequently, bubbles could overlap each other. In dense swarms, considerable overlap between the bubbles can prevail. Overlapping bubbles have hardly any influence on the numerical stability of the code, if the local gas fraction stays below about 5%. If the superficial gas velocity is increased, the (local) gas fraction can be significantly higher. In Sommerfeld (2000), it was stated that if the volume fraction of the gas is above $1 \cdot 10^{-3}$, the bubble bubble interaction becomes so important that four way coupling is needed. By introducing an encounter algorithm in our model this interaction has been accounted for. The algorithm ensures that bubbles never have relevant overlap with other bubbles. This opens the possibility to perform simulations at higher (local) gas hold-ups and thus higher superficial velocities.

If two bubbles hit each other two things can happen, either the bubbles bounce and separate or the bubbles coalesce. Rebounding is frequently seen when both bubbles have low Eö numbers. Coalescence is likely to occur when at least one of the bubbles has a large Eö number. In this model, only the collision is accounted for. The present models for collision and break-up are not sufficiently accurate to describe these phenomenon and are therefore not evaluated in this model. (See e.g. Chesters (1991) for models on coalescence and break-up).

If large bubbles encounter a strong shear flow, they can break up into two parts. This is also not accounted for due to the lack of accurate models that describe this phenomenon.

Bubble encounters

The collision algorithm is briefly described below. For more details on this method see e.g. Delnoij (1999) or Hoomans (2000).

From the initial position and velocity of the bubbles, for each bubble the smallest time before it encounters with any other bubble is computed. To speed up the algorithm, only those bubbles in close proximity to the reference bubble need to be taken into account. Subsequently the smallest encounter time is computed and all bubbles are moved over this time step.

The two bubbles, that are involved in this collision bounce, assuming fully elastic collision between hard spheres, by exchanging their momentum and the following smallest collision time is computed. This loop is repeated until a preset time, when the liquid flow field is updated.

The time till collision for two bubbles a and b is computed using the following equation:

$$t_{ab} = \frac{-b_{ab} - \sqrt{b_{ab}^2 - |\mathbf{v_a} - \mathbf{v_b}|^2 \left(|\mathbf{r_a} - \mathbf{r_b}|^2 - (R_a + R_b)^2 \left(1 + C_{VM}\right)^{\frac{2}{3}} \right)}}{|\mathbf{v_a} - \mathbf{v_b}|^2} \quad (5.26)$$

where

$$b_{ab} = (\mathbf{r_a} - \mathbf{r_b}) \cdot (\mathbf{v_a} - \mathbf{v_b}) \quad (5.27)$$

With the C_{VM} term the radii of the bubbles are increased slightly to account for a liquid shell which is surrounding the bubble. Its value is equal to the virtual mass coefficient.

5.3 Numerical method

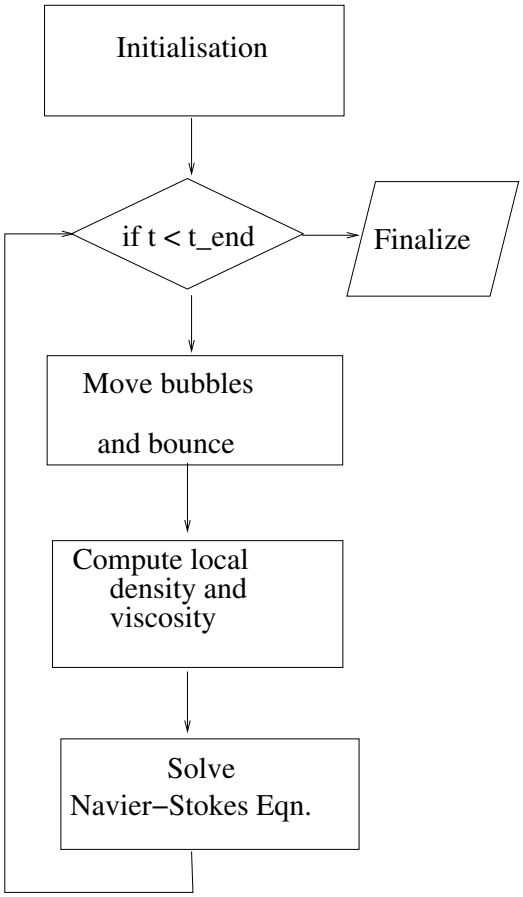

Figure 5.1: Computational flow diagram of the Discrete Bubble Code

In figure 5.1 a flow diagram of the code is presented. During the initialisation all velocities are set to 0 m/s and a hydrostatic pressure profile is applied. At start-up, no bubbles are present in the computational domain.

Every time, the main loop is entered, a number of tasks are performed. Firstly, it is checked whether any bubbles are present in the computational domain. The forces acting on these bubbles are computed from the local flow field data and they are moved according to the Newtonian laws of motion. The collision of the bubbles is done by applying the above presented collision algorithm.

Bubbles leave the computational domain if they hit the top of the domain.

Secondly, the Navier-Stokes equations, which are discretized on a staggered Eulerian grid, are solved using a SIMPLE algorithm (Patankar, 1980). An Incomplete Choleski Conjugate Gradient (ICCG) method is used to solve the resulting PPE. The convective terms are evaluated by a second order accurate flux limited Barton scheme (Centrella and Wilson, 1984). The viscous stresses are evaluated from standard central difference approximations.

At all the boundaries (except for the top) of the computational domain, no-slip conditions are applied. Free-slip is applied at the top wall. Fluid inflow

and outflow is allowed for by arranging ring cells near the top of the column.

5.4 Experimental set-up

Before showing the results from the numerical simulations, the experimental set-up used to validate the model results will be explained.

A *Particle Image Velocimetry* (*PIV*) technique[1] was used to measure the flow-field of the gas and the liquid phase. The *PIV* setup consisted of two parallel cameras connected to two data cubes. This configuration made it possible to measure the liquid and the gas-phase velocity distribution simultaneously. To study the flow pattern of the continuous phase the motion of tracer particles was analysed while in the discrete phase the bubbles themselves were used as tracers for the *PIV* measurements. Using fluorescent tracer particles and optical filters it is possible to separate the signal from the continuous and the discrete phases during the measurements. Details on this method have been reported by Deen (2001).

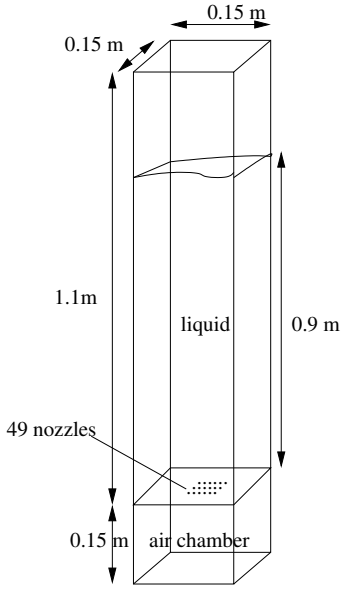

Figure 5.2: Schematic representation of the bubble column used for the experiments.

The experimental data reported in this study are taken with a light sheet positioned at the centre of the bubble column. In figure 5.3, time averaged data from these measurements are shown. The left figure (a) shows the liquid phase velocity field while the right figure (b) shows the gas phase velocity field. In the continuous phase, an upwards directed stream is located at the centre of the column while at the walls a small downstream can be observed.

For validation of the numerical models a number of characteristic parameters have been selected. At four different heights in the column (0.18, 0.36, 0.54 and 0.72 m), the vertical liquid velocity (u_z), the vertical bubble velocity (v_z)

[1] A good introduction to *PIV* can be found in Raffel et al. (1998)

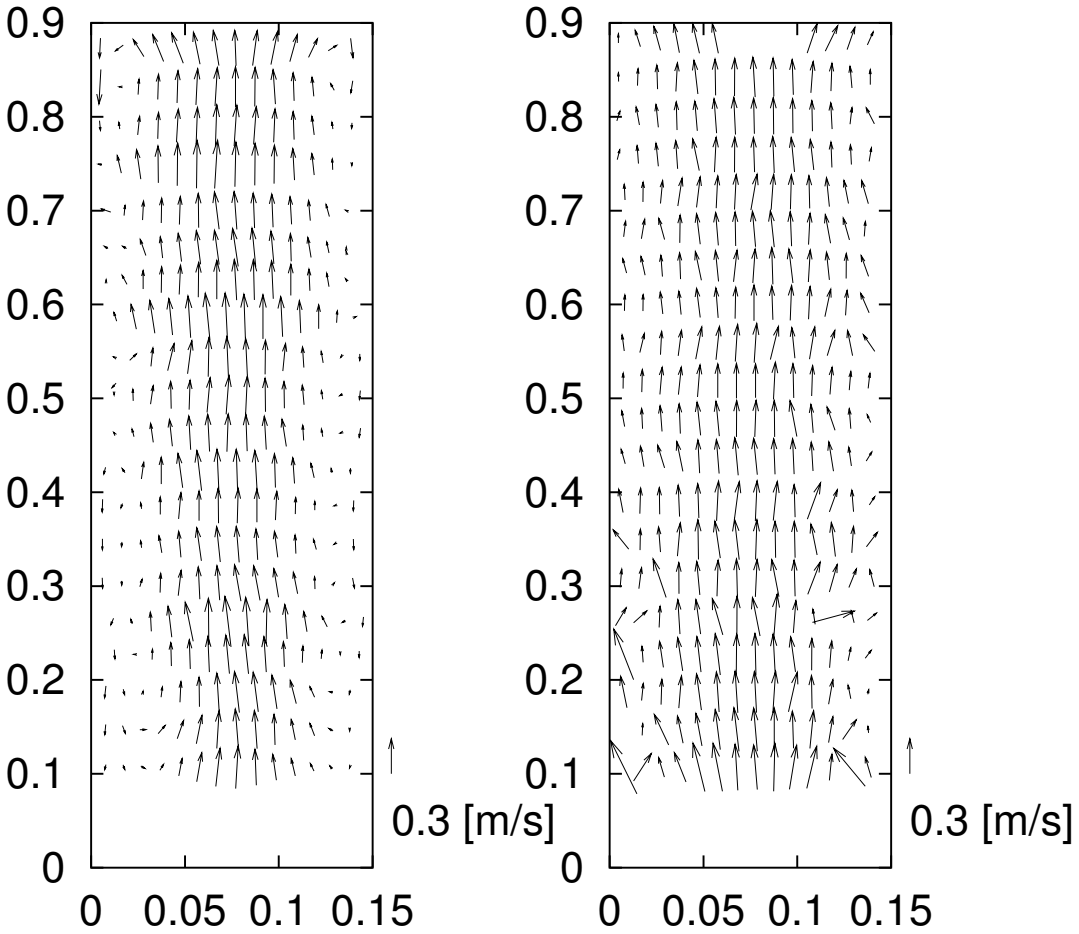

(a) Liquid phase

(b) Gas phase

Figure 5.3: Data obtained from *PIV* measurements. a: continuous phase, b: gas phase. $L/D = 6$, $v_{sup} = 0.0049\ m/s$.

and the standard deviation of u_z were determined and plotted in the same graph as the numerical data.

The laser, used for construction of the light sheet, was positioned on the right side of the bubble column. The data obtained for the left side of the column are therefore somewhat less accurate since the light was sometimes blocked by the bubbles in the path of the light. This could be observed in the standard deviation of the vertical velocity. See for example the experimental data in figure 5.11(b).

5.5 Model verification

In this section the simulation results are discussed. Firstly we concentrate on the implementation of new elements and secondly a comparison with experimental data from *PIV* measurements.

All simulations were performed for a rectangular bubble column (see figure 5.2). The dimensions of this column were 0.15 m × 0.15 m × 0.9 m. The bubbles were injected through 49 nozzles with a pitch of 6.25 mm in the middle of the column. For the experiments the same column was used. The air for the bubbles was supplied via an air chamber of 0.15 m×0.15 m×0.15 m (see figure 5.2) which was situated below this bottom plate. The nozzles had a diameter of 1.0 mm. The total column height was 1.1 m of which 0.9 m was filled with demineralised water before starting the experiment.

In table 5.1 the details of the simulations that were carried out have been summarised. The first simulations use the model reported by Delnoij (1999)[2]. In simulation 2, the effects of mesh refinement are investigated. In simulations 3 and 4, the Barton algorithm for the discretisation of the convective terms and the LES turbulence model are introduced.

In simulation 5, the bubble diameter is doubled as this is more in line with the experimentally observed bubble size. Since the current implementation of the model is limited to bubbles which are smaller than the mesh size the calculations were carried out on a relatively course mesh. In simulation 6 the closure relations proposed by Tomiyama et al. (1998) have been introduced. In simulation 7, the superficial gas velocity is doubled and the Barton and

[2]The virtual mass forces are computed explicitly as proposed by Darmana (2002)

LES algorithm are switched on. In simulation 8 the collision algorithm is invoked. Finally in simulation 9 the settings of simulation 8 are combined with the bubble diameter and the superficial gas velocity of simulation 1.

All data in the subsections below are time averaged. After about 20 s of simulated time, a stable operating regime was established. It was shown that these first 20 s of every simulation introduced considerable noise to the averaging process and were therefore left out in the time averaging. The simulations on the coarse mesh were averaged over 180 s (from 20 s to 200 s). The simulations on the finer mesh were averaged over 120 s (from 20 s to 140 s) in view of the required computational efforts.

Table 5.1: Overview of the simulations. Flux scheme : UP Upwind, BA Barton. Closure relations A:Delnoij (1999), B:Tomiyama (1998)

case.	mesh	V_{sup} $[mm/s]$	d_b $[mm]$	Δt	closure	flux-scheme	LES	encounter model
1	$15 \times 15 \times 90$	2.4	3.0	0.001	A	UP		
2	$25 \times 25 \times 90$	2.4	3.0	0.001	A	UP		
3	$25 \times 25 \times 90$	2.4	3.0	0.001	A	BA		
4	$25 \times 25 \times 90$	2.4	3.0	0.001	A	BA	$\surd$	
5	$15 \times 15 \times 90$	2.4	6.0	0.001	A	UP		
6	$15 \times 15 \times 90$	2.4	6.0	0.001	B	UP		
7	$15 \times 15 \times 90$	5.0	6.0	0.001	B	BA	$\surd$	
8	$15 \times 15 \times 90$	5.0	6.0	0.001	B	BA	$\surd$	$\surd$
9	$15 \times 15 \times 90$	2.4	3.0	0.001	B	BA	$\surd$	$\surd$
10	$15 \times 15 \times 90$	2.4	3.0	0.0005	B	BA	$\surd$	$\surd$

Case 1 : Base case / Delnoij Model

This model was extensively discussed by Delnoij (1999) and is used as a starting point to inspect the effects of the proposed modifications. In figure 5.4 the vertical liquid velocity, the liquid standard deviation value and the vertical gas velocity are presented at four different heights, for this case. Firstly the dependence on grid size and time step were studied. Figure 5.5 shows two simulation results where the number of computation cells was changed from $15 \times 15 \times 90$ to $25 \times 25 \times 90$ (case 2). Although the grid size did effect the simulation results to some extent, possibly because of the smaller averaging time for the finer grid, it is believed that quite reasonable results can be obtained with the relatively coarse grid. In figure 5.6 simulation results using different time-steps[3] are shown. The time-step was changed from 10^{-3} s to $5 \cdot 10^{-4}$ s. In the lower section of the column the differences in the calculation results are minimal, while in the upper section the differences are somewhat larger, but still relatively small, indicating a small start-up effect. It is concluded that with the coarse grid and the larger time-step quite acceptable results can be obtained.

Case 3: Effect of flux scheme

Replacing the Upwind flux scheme, as used in cases 1 and 2, by a second order accurate Barton flux scheme to discretise the convection terms has a small effect on the flow pattern of the two phases. When the Barton flux scheme was applied, a small decrease in gas velocity was observed. The maximum mean liquid velocity decreased from about 0.15 m/s to about 0.12 m/s. From previous work (e.g. Rider et al. (1995)) it is known that the gas-phase velocity field is strongly effected by the flux-model, while the liquid phase velocity field is was hardly effected. In our Lagrangian modelling of the gas phase the discrete bubbles are tracked very accurately. Hence, only a small improvement in the description of the continuous phase is observed.

[3]These simulations were conducted with the a version of the *DBM* code where all new elements were included.

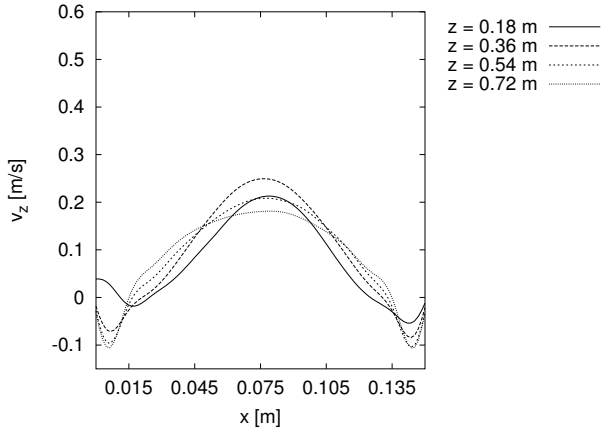

(a) Vertical liquid velocity.

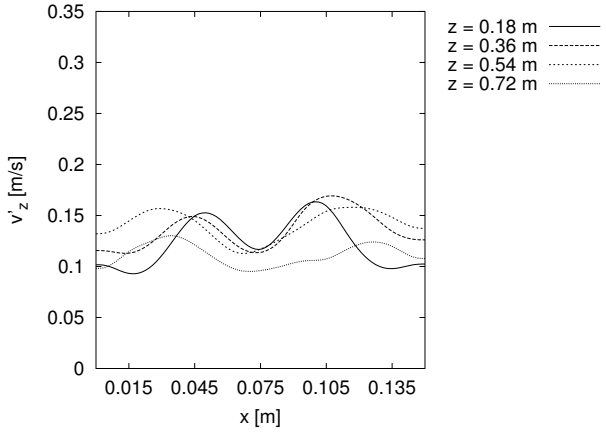

(b) Standard deviation of the vertical liquid velocity.

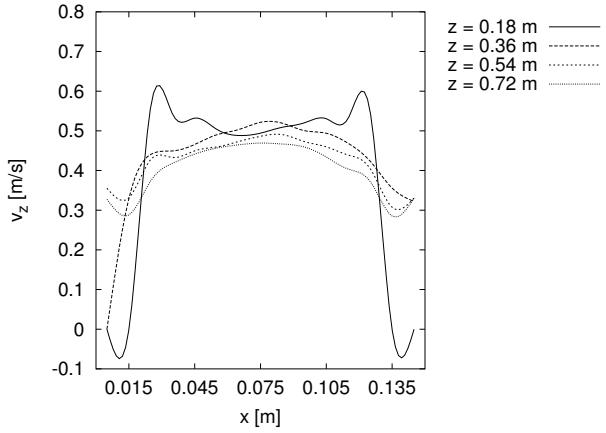

(c) Gas phase velocity.

Figure 5.4: Case 1: base case.

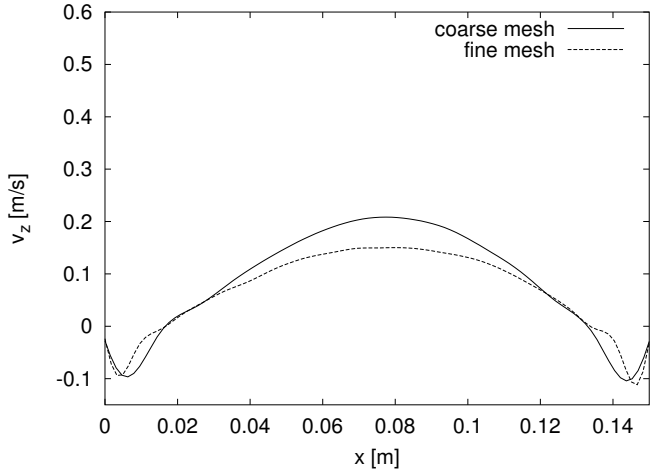

Figure 5.5: Vertical liquid velocity at 0.54 m computed on a course and a fine mesh.

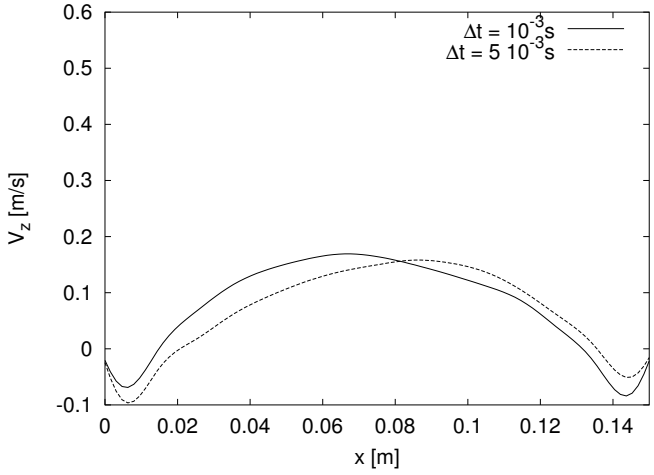

Figure 5.6: Vertical liquid velocity at 0.54 m computed with time-steps of 10^{-3} and $5 \cdot 10^{-4}$ respectively.

Case 4: Effect of the LES turbulence model

In case 4 an LES turbulence model was introduced. The liquid phase velocity profile, shown in figure 5.7, shows a slight decrease in the velocity as compared to the previous cases where the turbulent viscosity was ignored. Especially the maximum velocity in the lower part of the column has decreased and has become much more flat. With the LES turbulence model the variation of the gas velocity as a function of the axial coordinate increased, which could be caused by an increased start-up effect. The standard deviation values decreased to about one third of the value of the previous case indicating a decreased dynamic behaviour of the bubble column. All these effects can be explained by the increase in viscosity that was introduced by the turbulence modelling.

Cases 5-6: Effect of the bubble diameter and the bubble closure relations

For case 5, a bubble diameter of 6 mm was used because this is closer to the experimentally observed bubble sizes. When using the same drag relation as Delnoij (1999), which were taken from Clift et al. (1978), larger bubbles have a higher terminal velocity than smaller bubbles (see table 5.2). In figure 5.10 b, this increased gas velocity can be recognized. The mean vertical liquid velocity has decreased (see figure 5.10 a). This can be explained by the decrease in total cross-section area of the bubbles. The volume of the bubbles increases with d_b^3, while the cross section area increases by d_b^2. Consequently, using a constant gas loading, the number of bubbles decreases more rapidly, when assuming larger bubbles, than the decrease in the total cross-section area. Therefore, the total drag-force exerted on the liquid phase decreases, resulting in a decreased mean liquid velocity.

The introduction of new closure relations effects the mean position of the bubble plume. In figure 5.9 a snapshot of the bubble positions, simulated using the Delnoij (1999) and the Tomiyama (1998) closure relations is shown. With the Tomiyama closure relations the bubble plume remains more concentrated and is less spread over the cross-section of the column. The homogeneous top region observed with Delnoij closures is almost absent. Consequently, the liquid and gas velocities near the centre of the column have increased, resulting in a slightly different velocity distribution, as is shown in figure

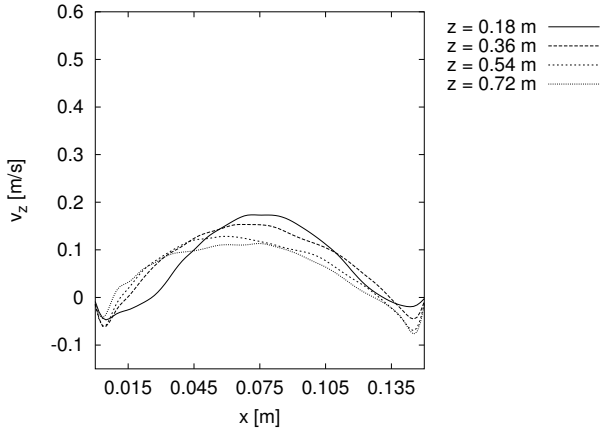

(a) Vertical liquid velocity.

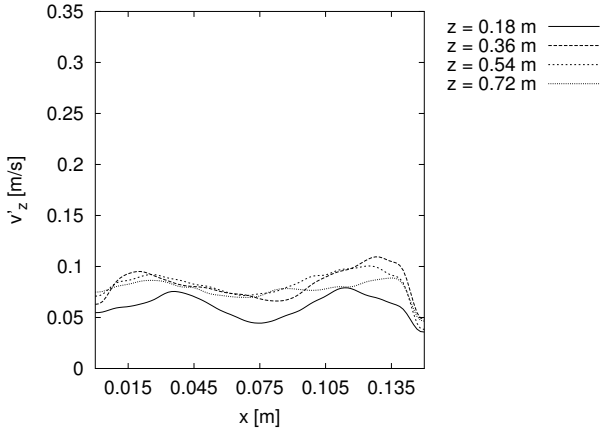

(b) Standard deviation of the vertical liquid velocity.

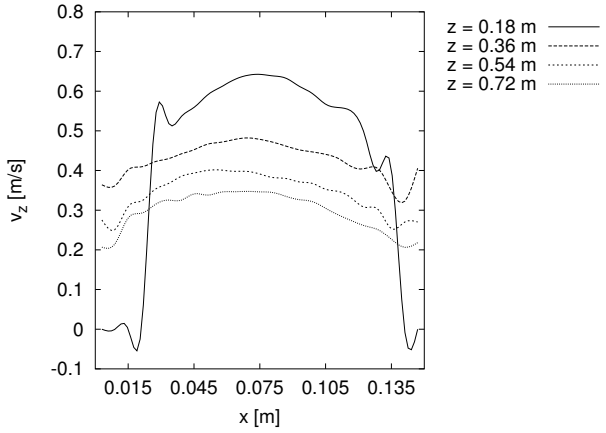

(c) Gas phase velocity.

Figure 5.7: Case 4: refined grid using the Barton flux scheme and the LES model.

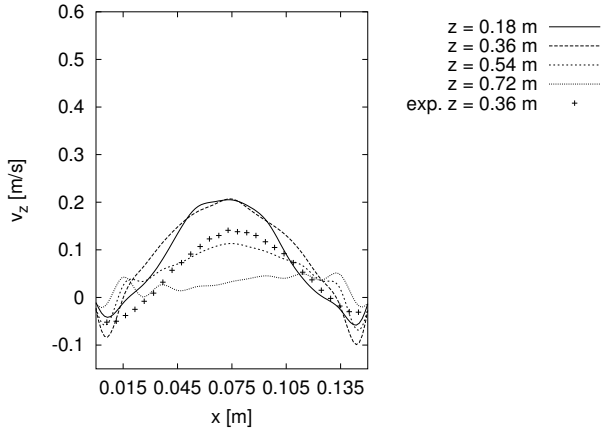

(a) Vertical liquid velocity.

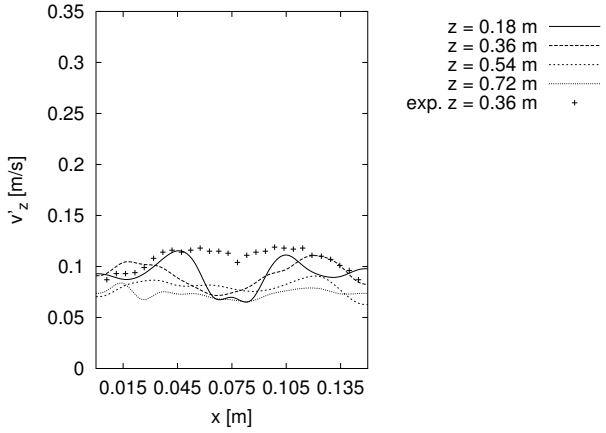

(b) Standard deviation of the vertical liquid velocity.

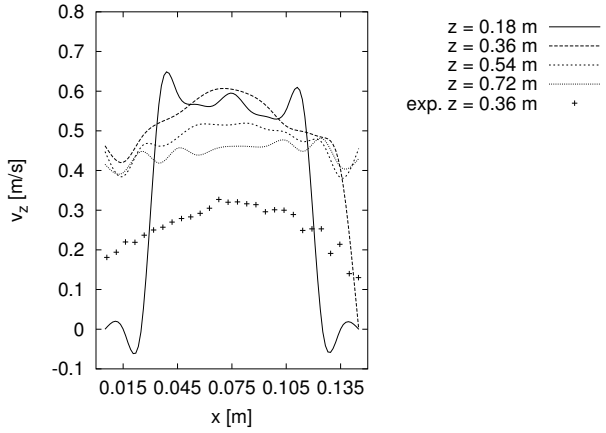

(c) Gas phase velocity.

Figure 5.8: Case 5: bubble diameter 6 *mm* bubbles.

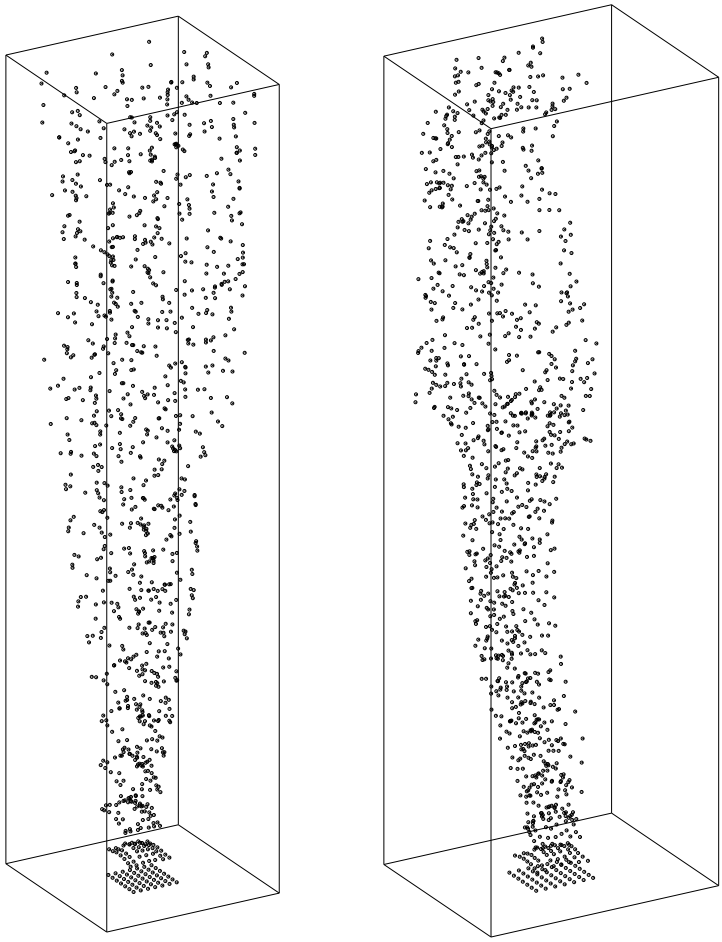

(a) Delnoij closures (b) Tomiyama closures

Figure 5.9: Distribution of the bubbles using the Delnoij closures (a) and the Tomiyama closure relations(b).(Case 5 and 6)

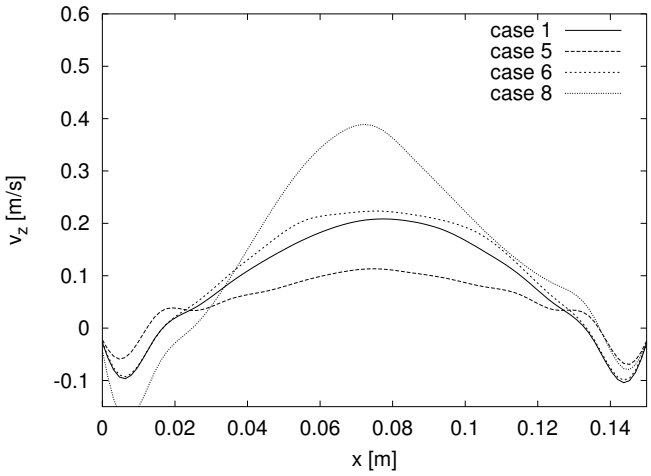

(a) Vertical liquid velocity

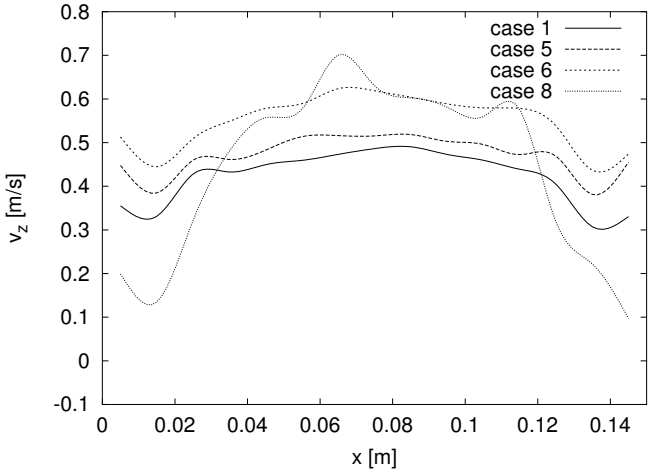

(b) Gas velocity

Figure 5.10: Liquid and gas velocity at $z = 0.54\ m$ for the cases 1,5,6 and 8.
case 1: Delnoij base case.
case 5 $d_b = 6\ mm$; $V_{sup} = 2.4\ mm/s$; Delnoij Closures.
case 6 $d_b = 6\ mm$; $V_{sup} = 2.4\ mm/s$; Tomiyama Closures.
case 8 $d_b = 6\ mm$; $V_{sup} = 5.0\ mm/s$; Tomiyama Closures, LES-model, encounter model.

Table 5.2: Terminal rise velocity of bubbles using different diamters and different drag relations.

$d_b\ [mm]$	$v_\infty\ [m/s]$	$v_\infty\ [m/s]$
	Clift et al. (1978)	Tomiyama (1998)
4	0.34	0.39
6	0.42	0.38

5.10.

Case 7-8: Effect of superficial velocity and encounter model

In case 7 the superficial gas velocity was increased from 2.4 mm/s to 5.0 mm/s. Because of the high void fractions that occur at these high gas loadings, this simulation, without the encounter algorithm, crashed after about 16 s simulated time, as was expected.

In case 8 the encounter algorithm was incorporated and consequently the void fractions that occur at this high gas velocity (5 mm/s) could be computed without any computational difficulties. For the higher superficial gas velocity with the encounter model, the mean gas velocity was hardly effected, however, the mean vertical liquid velocity has increased strongly, especially in the centre of the column.

Case 9: Comparison of the Delnoij model with the improved model

When the results of the base case (case 1) are compared to a simulation with all new features switched on all the effects described above are found simultaneously. The bubble plume narrows, resulting in increased gas and liquid velocities near the plume. The mean velocity of both phases has decreased slightly as a result of the LES turbulence modelling. As a side effect of this, the standard deviation velocity has slightly decreased indicating a less dynamic behaviour of the plume.

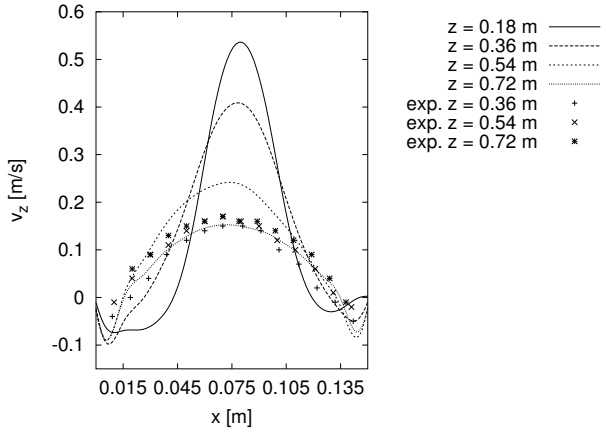

(a) Vertical liquid velocity.

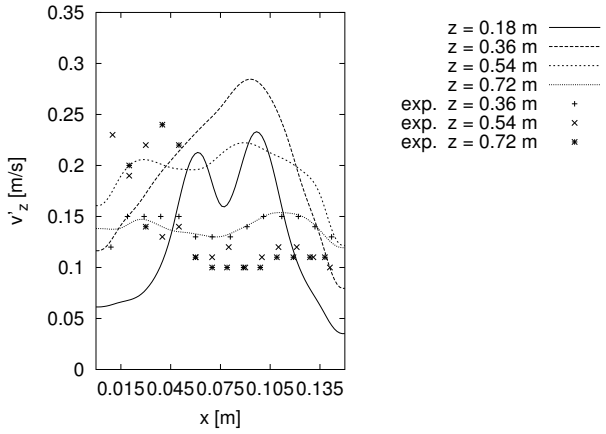

(b) Standard deviation of the vertical liquid velocity.

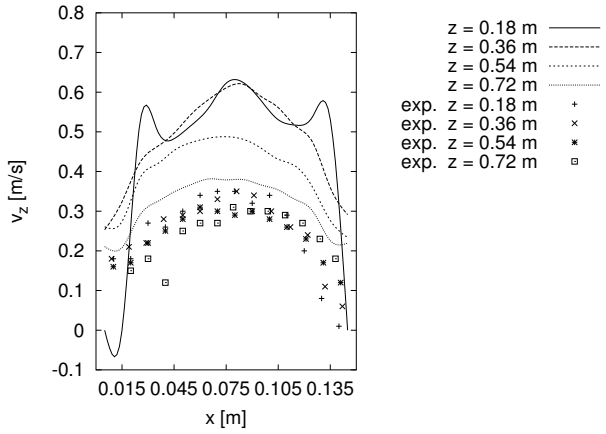

(c) Gas phase velocity.

Figure 5.11: Case 8: high superficial gas velocity using the encounter model.

5.5.1 Comparison to experimental results.

The simulation results of case 8 were compared to experimental data and show a quite reasonable correspondence at higher axial positions in the column. The liquid as well as the gas velocity in the lower part of the column is strongly over-predicted. The over-prediction of the gas velocity is probably due to the high void fraction at the relatively high superficial gas velocity. The closure relations should be adapted to accommodate these high void fractions. The over prediction of the liquid velocity has most likely the same origin. The standard deviation values predicted by the model are also slightly high compared with the experimental data, pointing towards an over-prediction of the dynamics in the column. These results could indicate that the total viscosity of the system is under predicted, probably caused by an under-prediction of the turbulence. Another option could be that the assumed fully elastic encounters of the bubbles generate too high bubble velocities.

5.6 Concluding remarks

Firstly it was shown that with the selected grid size, time-step and averaging time quite reasonable results could be obtained. The introduction of the Barton second order accurate limited flux scheme for the discretisation of the convection terms had a minor effect on the distribution of the liquid velocity. The increase by the LES turbulence modelling resulted in a lower and more flat liquid phase profile and strongly decreases the standard deviation values. The incorporation of the new closure relations for the forces acting on the bubbles narrows the bubble plume and consequently the velocities near the plume increased. This effect will probably increase when a size distribution is applied to the bubble diameter. The introduction of the Barton second order accurate limited flux scheme and the LES turbulence model had a minor effect on the distribution of the liquid velocity. The introduction of a collision model, enabled simulation of bubble columns with high gas loadings. The comparison to experimental data showed that the model over predicts the gas and liquid velocities in the lower part of the column, while at the top section the predictions are reasonably accurate. Further research is needed to investigate closure relations that account for high void fractions,

the elasticity of the bubble encounters and an accurate evaluation of the local effective viscosity.

5.7 Acknowledgements

The author wishes to thank Prof. B. Hjertager and Dr. ir. N. G. Deen for the opportunity to conduct two camera *PIV* measurements in their bubble column set-up at Aalborg University Esbjerg, Denmark. Also thanks to D. Darmana (MSC) for the huge amount of work he did in finding the origin of a numerical error in the code.

Chapter 6

Concluding remarks and outlook to future developments

In this final chapter, the concluding remarks of this study are summarised and in the final section new challenges in the field of modelling bubbly flows are discussed. Along with this outlook possible paths to reach these new objectives are proposed.

6.1 Conclusions: Detailed models

In this study both a *VoF* and a *Front Tracking* model were successfully implemented in a computer code. Within the constraint of 0.5 <Eö< 40 and the computational limits in time and computer capacity as used in this study, these models perform very well. The applicability window can probably be enlarged if sufficient fine grids are applied. The advances that were made during development of these codes includes the incorporation of:

for *Front Tracking*:

- a flow solver algorithm that can handle very high density ratios
- a straightforward implementation of the surface tension model based on interfacial tensile forces
- an integrated version of the Peskin smoothing function

- an energy minimisation algorithm
- and an algorithm that can re-construct the interface mesh in a number of very exceptional cases.

for *VoF*:

- a newly developed surface tension algorithm based on the interfacial tensile forces between adjacent surface elements
- a smoothing function for computing the normal to the interface, the local density and the local viscosity
- a correction for the computed fluxes
- the computation of the local viscosity is now based on the harmonic averaging of the kinematic viscosity.

Both codes are capable of evaluating two fluid systems with a density ratio of up to 10^4. This was achieved by using a non-conservative form of the Navier-Stokes equation that treats the local density explicitly in time. The error that is introduced by this scheme is relatively small as a result of the small time steps that are applied in the simulations(10^{-5} s).

In the *Front Tracking*-model the surface tension model of Unverdi and Tryggvason (1992) has been simplified. The approach presented in this study does not need the creation of the curved surface over every interface element. This reduces the amount of computational work which is needed for two reasons. Firstly, the computation of the mean value of the tensile stresses between two adjacent surface elements is avoided. Secondly, the evaluation of the stresses on segments of the curved interface representation is not needed. It was shown that the excess pressure inside the bubble was predicted equally well by this new method as by the original method used by Unverdi and Tryggvason (1992).

The newly introduced surface energy minimisation performs well and results in a smoother interface. It reduces the number of 'sharp' angles between interface elements. This results in less excessive local tensile forces which has a stabilising effect on the numerics.

The last improvement to the model is the addition of an algorithm that is able to take out a few interface mesh problems that can cause numerical problems that make the code crash.

In the *VoF*-model, the introduction of a new surface tension algorithm that is also based on the tensile stresses between the interface segments has replaced the frequently applied *CSF* model of Brackbill et al. (1992). The algorithm gives very accurate results in predicting the excess pressure inside the bubble and can cope with highly curved interfaces.

A second major improvement is the use of a smoothened colour function for the computation of the orientation of the interface segments. For the calculation of the volume beneath the interface, the non-smoothed colour function is applied. This results in a better connectivity of the adjacent surface elements. For the smoothening, an integrated version of the smoothing function of Peskin (1977) is applied. This has the advantage of being non iterative method, oppose to the iterative methods previously published in the literature (see e.g. (Rider and Kothe, 1998)).

6.1.1 Comparison of the models

The bubble shapes predicted by both models correspond well in agreement with the shapes reported in literature. The *VoF*-model is superior in its inherent conservation of the gas volume. It also predicts, if compared to the *Front Tracking*-model, a more dynamic behaviour of the interface, resulting in an more dynamic bubble motion.

Bubbles simulated using the *Front Tracking*-method have a slightly smaller terminal rise velocity. This is probably caused by the relative wide computational stencil that is used to compute the velocity at the location of the node's. The *VoF*-model evaluates the motion of the interface based on the flux through the cell faces. This flux is computed using the staggered velocity data at the cell faces. In *Front Tracking* however, the local velocity a the location of a node is computed using a smooth delta function. The local velocity is the weighted average of the fluid velocity at a number of cells surrounding the node. This could have a stabilising effect on the interface dynamics.

6.2 Conclusions: Discrete Bubble Models

The three-dimensional discrete bubble model was improved by the introduction of four-way coupling, new closure relations, a second order limited flux scheme and a LES turbulence model.

The introduction of the four way coupling enabled the simulation of a higher gas throughput through the column. Simulations with superficial gas velocities up to 15 mm/s were conducted. The new closure relations changed the topology of the bubble plume. The bubble plume was narrowed and the liquid velocity near the plume consequently increased. The incorporation of the second order accurate Barton flux scheme had little effect on the overall flow behaviour since the behaviour of the gas phase was already described in great detail. The LES model effectively increased the viscosity resulting in lower liquid velocities and decreased column dynamics.

Comparison with experimental data showed that the numerical results are reasonably accurate in the more dispersed regions of the column. The velocities in the regions where the bubble concentration is high is somewhat over predicted.

6.3 Outlook: detailed models

6.3.1 Single bubble systems

In future research the detailed models *Front Tracking* and *VoF*, that were developed in this study, could be applied to test or even derive closure relations for less detailed models such as *DBM* or any other Euler-Lagrangian or Euler-Euler model. This could be achieved by performing computations using a number of selected 'canonical' flow patters which isolate the effect of one single closure relation. For example, from a bubble rising in a stagnant liquid the drag force on that bubble can be evaluated and from its acceleration the virtual mass force could be obtained. An other example could be to study the lift force by releasing a bubble in a shear flow.

A second subject that would be of interest to study is the influence of a number of bubbles on the behaviour of the other bubbles. Tryggvason (1999) and Tomiyama (1998) have reported some work in this field but only for a

limited number of configurations.

6.3.2 Multiple bubble systems

Multiple bubble systems are the next challenge in detailed modelling. Closure relations used in Euler-Lagrangian and Euler-Euler models often ignore the presence of surrounding bubbles. By using detailed models such as *VoF* and *Front Tracking*, simulations can be run to study the influence of neighbouring bubbles on the shape, dynamics and the collective behaviour of the rising bubbles.

In this section two simulations of systems with more than one bubble are shown. The physical properties that were used in these simulations are listed in table 6.1. When considering systems with more than one bubble, a few remarks concerning break-up and coalescence of bubbles must be made. *VoF*-models are, up to now, only able to compute one interface within each computational cell. Consequently, if two interfaces move into the same computational cell, they will be detected as a single interface leading to artificial coalescence. The same problem emerges with respect to breakage of bubbles. Bubbles only break if one cell between the two new bubbles is almost empty. In other words, in *VoF* all fluids are 'super-coalescent': bubbles that hit each other always coalesce. The *VoF* method should be extended to allow for two or more interfaces in one cell to overcome this problem. Once this has been achieved, subgrid models should be develloped to incorporate the pressure build up between the bubbles in the momentum equations.

In *Front Tracking* this problem does not occur the same way. This is due to the fact that each interface is represented by its own unstructured mesh. The different meshes do not interact with each other, even when the meshes pass each other. In *Front Tracking* this could be overcome by writing an algorithm that can create a connection between the meshes of the different bubbles. Since the meshes are unstructured, this could be a arduous task. Whether interfaces merge or break, could be determined by computing the total energy of the new structure. If the newly formed mesh has a lower total energy than this new mesh is preferred over the previous one. If not the re-meshing should be reversed. The *Front Tracking* model would also need a subgrid model to include the pressure build-up between the bubbles in the momentum equations.

Table 6.1: Physical and numerical data used in the multiple bubble experiments.

bubble diameter	d_e	$0.006\ m$
dimensionless numbers	$\log(Mo)$	-3.2
	Eo	5.7
liquid phase	ρ	$1230\ kg/m^3$
	μ	$0.023\ Pa.s$
gas phase	ρ	$1.29\ kg/m^3$
	μ	$17.1 \cdot 10^{-6}\ Pa.s$
	σ	$0.0759\ N/m$
column	number of cells	$60 \times 60 \times 60$
	dimensions	$0.025 \times 0.025 \times 0.025\ m^3$

The multiple bubble systems that will be shortly discussed here are:

- co-axial rising bubbles
- adjacent rising bubbles

Two co-axial bubbles

Two bubbles with $d_e = 6\ mm$ were released in the centre of the column at a mutual vertical distance of 6 mm from each other. Figure 6.1 shows the development of the two bubbles in time. The upper bubble develops to its normal shape as if no other bubbles were present. Under influence of the vortices behind the leading bubble, the tailing bubble is deformed, it accelerates and slowly catches up with the first bubble. Finally the bubbles coalesce.

Two Adjacent bubbles

The same bubbles which were used in the previous section were released next to each other in a $0.021\ m \times 0.021\ m \times 0.021\ m$ box, using $70 \times 70 \times 70$ grid cells. The distance between the two centres of mass was $0.0080\ m$. From their originally spherical shape the bubbles develop to the ellipsoidal shape

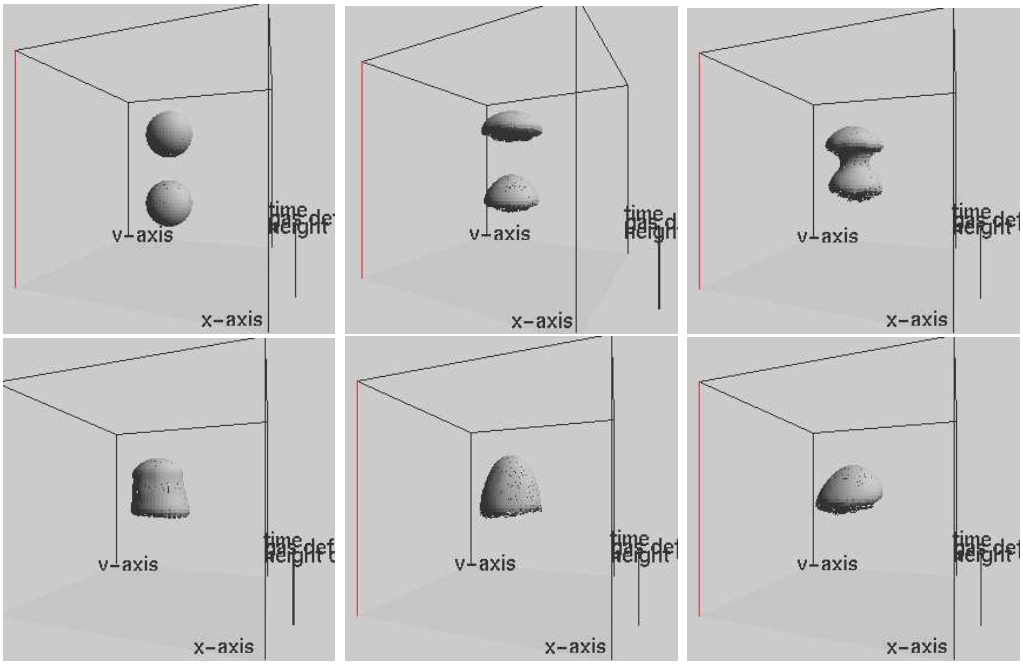

Figure 6.1: Two co-axial rising bubbles, with their shape evolution and developing flow field using the full three dimensional *VoF* algorithm. During the simulation the computational domain is moved with the centre of mass of the two bubbles.

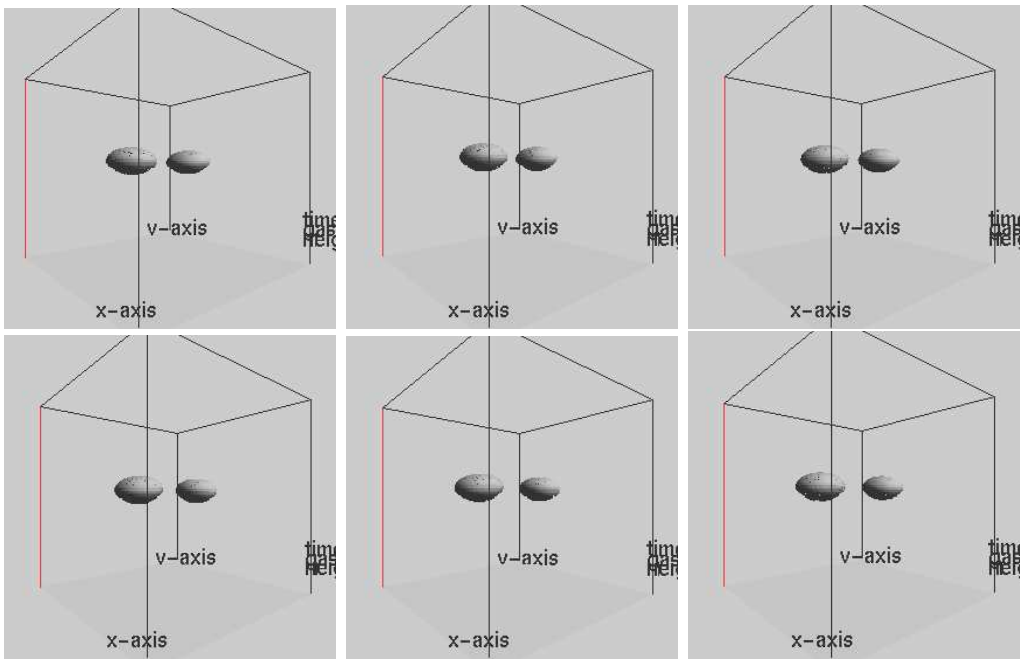

Figure 6.2: Two adjacent bubble rising in a spiralling motion. $t = 0.005$, 0.0075, 0.01, 0.0125, 0.015, 0.0175 s

as expected from Grace's bubble diagram (Grace, 1973). As a result of the interaction between the bubbles the bubbles start a wobbling motion and a spiralling path. The simulation results are shown in figure 6.2.

6.3.3 Discussion

Within the operating window previously given, the *VoF* algorithm can be used to study systems containing multiple bubbles, resulting in data on the influence which neighbouring bubbles and their wakes have on each other. Details on bubble collision, break-up or coalescence can only be described with the *VoF* algorithms, if a more fundamental sub-grid model of these phenomena is included in the code. If two bubbles are released in a co-axial configuration, the tailing bubble catches up with the leading one resulting in coalescence of the bubbles. If two adjacent bubbles are released, the model predicts a spiralling motion.

Studying the dynamics of coalescence or break-up would involve a more detailed description of the interface dynamics. In the *VoF*-model the break-up and coalescence now occur as a result of the numerics and break-off errors. An algorithm to give the occurrence of these phenomena a sound physical basis should be developed to be able to simulate these phenomena. A first step to obtain this would be the development of an algorithm that allows more than one interface in a cell to avoid immediate merging of the interfaces if two interfaces enter a cell. For *Front Tracking* it is already possible to have more interfaces within one cell. Here the problem is to restructure the three dimensional interface mesh. A good starting point for coalescence could be the computation of the surface energy which was introduced in this thesis. Two interfaces only merge if the total energy of the newly formed interface is less than the energy of the original interface.

6.4 Outlook: Discrete Bubble Modelling

Discrete Bubble Models can already be applied to compute laboratory scale bubble columns. Refining the closure relations for the forces acting on the bubbles is still of major interest. New elements that should be introduced, include the treatment of bubbles that have a diameter larger than the cell spacing. In particular the interpolation of the local velocity for this size of bubbles and the treatment of the coupling from the discrete to the continuous phase is not clear.

Coalescence and break-up models should be studied and could be implemented in this code. This would make the model more versatile.

DBM could be combined with one of the detailed models to model a wide range of bubble diameters. The larger bubbles are dynamic and have a large impact on the flow patterns. The smaller, almost spherical bubbles only follow the flow and therefore are probably reasonably accurately described by closure relations. A further reason to treat small bubbles as discrete elements, is that smaller bubbles are hard to handle in detailed codes. The resulting information from these computations is probably not worth the computational effort needed to do so. Nevertheless, in case of mass-transfer, the small bubbles would be of great importance.

Apart from improving the fluid flow dynamics it would be interesting to

incorporate heat transfer, mass transfer and the treatment of chemical reactions. With this addition, the models can be applied to simulate real live chemical engineering problems. This could also be used to improve the physical product properties. Density, viscosity and especially surface tension of solutions could be computed more accurately.

6.4.1 Code optimisation and speed-up of the simulations

All the codes that were used in this study are still very time consuming (order of weeks or months on state of the art hardware). Specially if a sufficiently fine mesh is applied. The required CPU time could probably be reduced by better coding and applying smarter mathematical approaches such as (algebraic) multi grid methods to solve the Navier-Stokes equation or a ghost fluid method to separate the phases. To reduce the 'wall clock time', speed up could be achieved by making use of parallel hardware. The *PVM* [1] and the *MPI*[2] techniques are especially suitable for doing this, since they can be applied on a variety of parallel computers or clusters of computers.

6.4.2 Final remarks

In this thesis a large number of improvements have been introduced to different codes. These improvements were needed to compute a number of things which had not previously been possible. It will always be possible and necessary to improve the physics behind these models, but computer books are comparable to good books: they are only of use when read. The objective is never the code itself but the simulation results obtained with it. Comparing the simulation results with good experimental data, the weak points of the codes can be found and new ideas about the underlying physics can be generated. These can then be applied to further improve the predictive capability of the codes.

[1] Parallel Virtual Machine
[2] Message Passing Interface

Nomenclature

A	surface area	m^2
C	constant	
d	diameter	m
$D()$	Dirac-δ-function	
Eo	Eötvos number	
f	liquid fraction/ colour or indicator function	
F	force	N
g	constant of gravity	m/s^2
h	grid spacing	m
h	intersection allong the axis	
l	length of edge between two elements	m
L	length of computational domain	m
D	width of the computational domain	m
Mo	Morton number	
$\mathbf{n}$	normal vector	
p	presure	Pa
R,r	radius	m
$\mathbf{r}$	coordinate	m
Re	Reynolds number	
s	length	m
s_l	surface area	m^2
S	strain tensor	
t	time	s
$\mathbf{t}$	tangent vector	
$\mathbf{u}$	liquid velocity	m/s
$\mathbf{v}$	bubble velocity	m/s
V	volume	m^3
x,y,z	coordinate	m

Greek

α	angle	rad
Γ	bubble momentum	$N.m$
ϵ	liquid fraction	
ρ	density	kg/m^3
σ	surface tension constant	N/m
κ	curvature	m^{-1}
μ	dynamic viscosity	$Pa.s$
ν	velocity of sound	m/s
Ψ	stream function	

Subscripts

b	bubble
d	drag
e	interfacial pull
eq	equivalent
g	gas
g	gravity
i, j	between element i and j
l	liquid
l	surface element edge
l	lift
max	maximum
min	minimum
mix	mixing length
p	pressure
s	Smagorinski
vm	virtual mass
st	surface tension
tot	total
x	x-direction
y	y-direction
z	z-direction

Appendix A

Interface reconstruction in 3D-VOF

A.1 Introduction

In this appendix all the equations needed in 3D-VOF to reconstruct the interface and to calculate the fluxes are given. To limit the number of cases, all components of the normal $\vec{n}$ to the interface will be taken positive and it is assumed that the void fraction in a given cell is always smaller than 0.5. Furthermore it is made sure that the components of $\vec{n}$ always satisfy $n_1 < n_2 < n_3$. $n_y \leq n_z$. If one of these conditions is not full filled the interface will be rotated of translated in such a way that all the conditions are full-filed and after calculation of the fluxes these will be re-rotated. The rotations are explained in appendix B. In this appendix it is assumed that the size of the cell is unity which can be achieved via proper normalisation of the coordinates. $(1 \times 1 \times 1)$.

A.2 Determination of the surface element type

The determination of the surface element type is identical to the one used by D.L. Youngs (Youngs, 1987). Nevertheless the key issues will be given here. Young distinguishes the five surface elements types shown in figure A.1.

In the next paragraphs the variables h_0, h_1 and h_2 represent the distances from the origin of a given cell to the intersection point of the plane with respectively the x, y and z-axis of the computational cell. Due to the rotations and translations $h_0 \leq h_1 \leq h_2$.

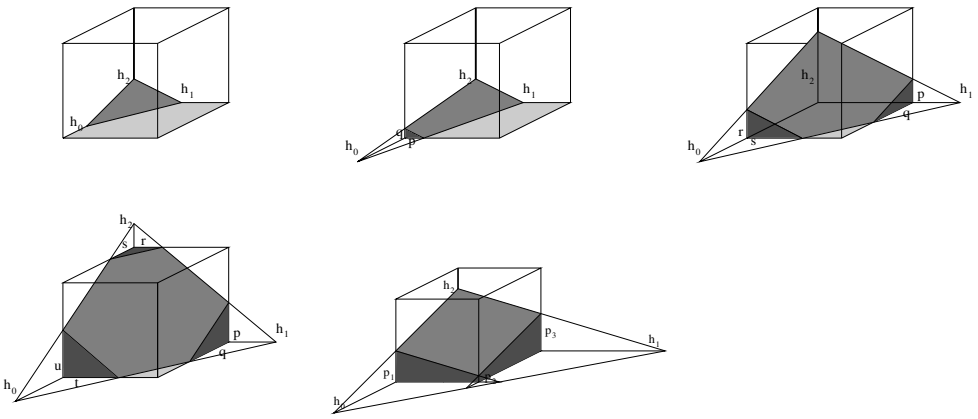

Figure A.1: The five surface element types.

In table A.1 the selection criteria for each type are given. A few cases need special attention. This is when one of the normal-vector components is 0. If e.g. $n_0 = 0$ and $n_1 = 0$. This means that a horizontal plane is present corresponding to an interface element of type 5. If $n_0 = 0$ and $f_{i,j,k} \leq \frac{n_1}{2n_2}$ the interface type is 2. If the last inequality is not fulfilled the interface element type is 5 again.

A.3 Calculation of the fluxes

Once the interface element type is known and the flow field is known the fluxes through the cell faces can be computed which in principal can occur through all six cell faces. Since the fluxes are calculated at the cell faces, only the outwardly directed fluxes need to be evaluated. In the next sections the calculation of these outward fluxes in all possible directions and for all five surface element types will be given.

Table A.1: Selection criteria for surface element types.

type	criteria
1	$6fn_0n_1n_2 \leq {n_0}^3$
2	${n_0}^3 < 6n_0n_1n_2f \leq {n_1}^3 - (n_1 - n_0)^3$
3	$n_0 + n_1 \geq n_2$ and ${n_1}^3 - (n_1 - n_0)^3 < 6fn_0n_1n_2 \leq {n_2}^3 - (n_2 - n_0)^3 - (n_2 - n_1)^3$ or $n_0 + n_1 < n_2$ and ${n_1}^3 - (n_1 - n_0)^3 < 6fn_0n_1n_2 \leq (n_0 + n_1)^3 - {n_0}^3 - {n_1}^3$
4	$n_0 + n_1 \geq n_2$ and ${n_2}^3 - (n_2 - n_0)^3 - (n_2 - n_1)^3 \leq 6fn_0n_1n_2$
5	$n_0 + n_1 \leq n_2$ and $(n_0 + n_1)^3 - {n_0}^3 - {n_1}^3 < 6fn_0n_1n_2$

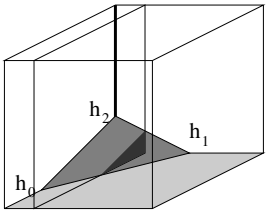

Figure A.2: Type 1.

Table A.2: Fluxes for type 1 surface element.

cell face	criteria	flux	figure
north	$v_n\Delta t \leq 1.0 - h_0$	$F_n = 0$	
	$v_n\Delta t > 1.0 - h_0$	$F_n = \left(\frac{h_0+v_n\Delta t-1}{h_0}\right)^3$	
south	$-v_s\Delta t \geq h_0$	$F_s = f$	
	$-v_s\Delta t < h_0$	$F_s = f\left(1 - \left(\frac{h_0+v_s\Delta t}{h_0}\right)^3\right)$	
west	$v_w\Delta t \leq 1.0 - h_1$	$F_w = 0$	
	$v_w\Delta t > 1.0 - h_1$	$F_w = \left(\frac{h_1+v_w\Delta t-1}{h_1}\right)^3$	A.2
east	$-v_e\Delta t \geq h_1$	$F_e = f$	
	$-v_e\Delta t < h_1$	$F_e = f\left(1 - \left(\frac{h_1+v_e\Delta t}{h_1}\right)^3\right)$	A.2
top	$v_t\Delta t \leq 1.0 - h_2$	$F_t = 0$	
	$v_t\Delta t > 1.0 - h_2$	$F_t = \left(\frac{h_2+v_t\Delta t-1}{h_2}\right)^3$	
bottom	$-v_b\Delta t \geq h_2$	$F_s = f$	
	$-v_b\Delta t < h_2$	$F_b = f\left(1 - \left(\frac{h_2+v_b\Delta t}{h_2}\right)^3\right)$	

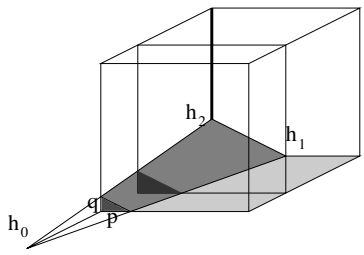

Figure A.3: Type 2 flux through north or south face.

Table A.3: Fluxes for type 2 surface element.

cell face	criteria	flux	figure
north		$F = \frac{1}{6}\left[-\left(pq\left(h_0-1\right)\right)\right.$ $\left.+\left(p_1q_1\left(h_0-1+v_0\Delta t\right)\right)\right]$ with $q = \frac{h_2}{h_0}\left(h_0-1\right)$ $p = \frac{h_1}{h_0}\left(h_0-1\right)$ $p_1 = p + v_0\Delta t\frac{h_1}{h_0}$ $q_1 = q + v_0\Delta t\frac{h_2}{h_0}$	A.3
south		$F = f - \frac{1}{6}\left[\left(h_0+v_0\Delta t\right)p_1q_1\right.$ $\left.-pq\left(h_0-1\right)\right]$ with $q = \frac{h_2}{h_0}\left(h_0-1\right)$ $p = \frac{h_1}{h_0}\left(h_0-1\right)$ $p_1 = p + \left(1+v_0\Delta t\right)\frac{h_1}{h_0}$ $q_1 = q + \left(1+v_0\Delta t\right)\frac{h_2}{h_0}$	A.3
west	$v_w\Delta t \le 1-h_1$	$F_w = 0$	
	$1-h_1 < v_w\Delta t \le 1-p$	$F_w = \frac{1}{6}\frac{h_0h_2}{h_1^2}\left(h_1+v_w\Delta t-1\right)^3$	A.4a
	$1-p < v_w\Delta t$	$F_w = f - \frac{1-v_w\Delta t}{4}\left[2h_2+2q-2\left(1-v_1\Delta t\right)\frac{h_2}{h_1}\right]$	A.4b
east	$-v_e\Delta t \ge h_1$	$F_e = f$	
	$p \le -v_e\Delta t < h_1$	$F_e = f - \frac{1}{6}\frac{h_0h_2}{h_1^2}\left(h_1+v_e\Delta t\right)^3$	A.4b
	$p > -v_e\Delta t$	$F_e = \frac{-v_e\Delta t}{4}\left[2h_2+2q-2\left(-v_e\right)\Delta t\frac{h_2}{h_1}\right]$	A.4a
top	$v_t\Delta t \le 1-h_2$	$F_t = 0$	
	$1-h_2 < v_t\Delta t \le 1-q$	$F_t = \frac{1}{6}\frac{h_0h_1}{h_2^2}\left(h_2+v_t\Delta t-1\right)^3$	
	$1-q < v_t\Delta t$	$F_t = f - \frac{1-v_t\Delta t}{4}\left[2h_1+2p-2\left(1-v_t\Delta t\right)\frac{h_1}{h_2}\right]$	
bottom	$-v_b\Delta t \ge h_2$	$F_b = f$	
	$q \le -v_b\Delta t < h_2$	$F_b = f - \frac{1}{6}\frac{h_0h_1}{h_2^2}\left(h_2+v_b\Delta t\right)^3$	
	$q > -v_b\Delta t$	$F_b = \frac{-v_b\Delta t}{4}\left[2h_1+2p-2\left(-v_b\right)\Delta t\frac{h_1}{h_2}\right]$	

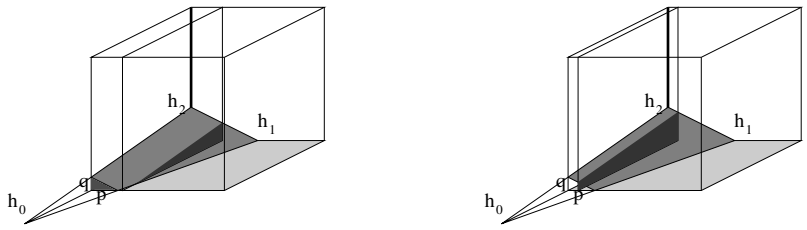

Figure A.4: Type 2 flux through west or east face

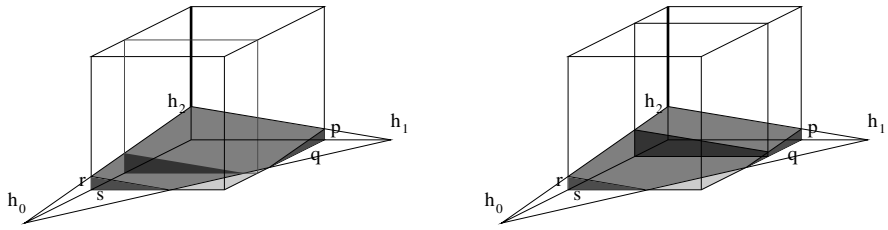

Figure A.5: Type 3 flux through north or south face.

Table A.4: Fluxes for type 3 surface element.

cell face	criteria	flux	figure
north	$v_n\Delta t \leq 1-q$	$F_n = \frac{1}{6}\frac{h_1 h_2}{h_0^2}\left[(h_0-1+v_n\Delta t)^3-(h_0-1)^3\right]$	A.5a
	$v_n\Delta t > 1-q$	$F_n = f-\frac{1-v_n\Delta t}{4}\left[2p+2h_2-2(1-v_n\Delta t)\frac{h_2}{h_0}\right]$	A.5b
south	$(-v_s)\Delta t \leq q$	$F_s = \frac{-v_s\Delta t}{4}\left[2p+2h_2-2(-v_s\Delta t)\frac{h_2}{h_0}\right]$	A.5b
	$(-v_s)\Delta t > q$	$F_s = f-\frac{1}{6}\frac{h_1 h_2}{h_0^2}\left[(h_0+v_s\Delta t)^3-(h_0-1)^3\right]$	A.5a
west	$v_w\Delta t \leq 1-s$	$F_w = \frac{1}{6}\frac{h_0 h_2}{h_1^2}\left[(h_1-1+v_w\Delta t)^3-(h_1-1)^3\right]$	
	$v_w\Delta t > 1-s$	$F_w = f-\frac{1-v_w\Delta t}{4}\left[2r+2h_2-2(1-v_w\Delta t)\frac{h_2}{h_1}\right]$	
east	$(-v_e)\Delta t \leq s$	$F_e = \frac{-v_e\Delta t}{4}\left[2r+2h_2-2(-v_e\Delta t)\frac{h_2}{h_1}\right]$	
	$(-v_e)\Delta t > s$	$F_e = f-\frac{1}{6}\frac{h_0 h_2}{h_1^2}\left[(h_1+v_e\Delta t)^3-(h_1-1)^3\right]$	
top	$v_2\Delta t \leq 1-h_2$	$F_t = 0$	
	$1-h_2 < v_2\Delta t \leq 1-r$	$F_t = \frac{1}{6}(h_2+v_2\Delta t-1)^3\frac{h_0 h_1}{h_2^2}$	A.6a
	$1-r < v_2\Delta t \leq 1-p$	$F_t = \frac{1}{6}\frac{h_1}{h_2}\frac{h_0}{h_2}\left[\epsilon^3-\left(\epsilon-\frac{h_2}{h_0}\right)^3\right]$ with $\epsilon = h_2+v_t\Delta t-1$	A.6b
	$1-p \leq v_2\Delta t$	$F_t = \frac{1}{6}\frac{h_0 h_1}{h_2^2}\left[(h_2+v_t\Delta t-1)^3-(r+v_t\Delta t-1)^3-(p+v_t\Delta t-1)^3\right]$	A.6c
bottom	$-v_b\Delta t \geq h_2$	$F_b = f$	
	$h_2 > -v_b\Delta t \geq r$	$F_b = f-\frac{1}{6}\frac{h_1}{h_2}(h_2+v_b\Delta t)^3$	A.6a
	$r > -v_b\Delta t \geq p$	$F_b = f-\frac{1}{6}\frac{h_1}{h_2}\frac{h_0}{h_2}\left[\alpha^3-\left(\alpha-\frac{h_2}{h_0}\right)^3\right]$ with $\alpha = h_2+v_b\Delta t$	A.6b
	$p > -v_b\Delta t$	$F_b = f-\left[\frac{1}{6}\frac{h_0 h_1}{h_2^2}\left((h_2+v_b\Delta t)^3-(p+v_b\Delta t)^3-(r+v_b\Delta t)^3\right)\right]$	A.6c

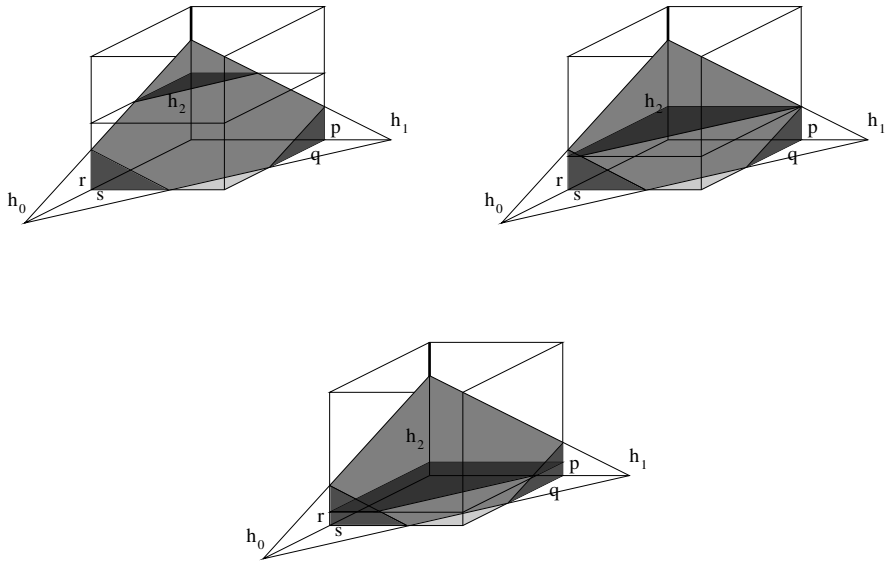

Figure A.6: Type 3 flux through top or bottom face.

Table A.5: Fluxes for type 4 surface element.

cell face	criteria	flux	figure
north	$v_0\Delta t \leq 1-q$	$F_n = \frac{1}{6}\frac{h_1 h_2}{h_0^2}\left[(h_0-1+v_n\Delta t)^3-(h_0-1)^3\right]$	A.7a
	$1-q < v_0\Delta t \leq 1-s$	$F_n = \frac{1}{6}\frac{h_1 h_2}{h_0^2}\left[(h_0+v_n\Delta t-1)^3-(h_0-1)^3 - (q+v_0\Delta t-1)^3\right]$	A.7b
	$1-s < v_0\Delta t$	$F_n = \frac{1}{6}\frac{h_1 h_2}{h_0^2}\left[(h_0+v_n\Delta t-1)^3-(h_0-1)^3 - (q+v_n\Delta t-1)^3-(s+v_n\Delta-1)^3\right]$	A.7c
south	$-v_0\Delta t \leq s$	$F_s = f-\frac{1}{6}\frac{h_1 h_2}{h_0^2}\left[(h_0+v_s\Delta t)^3-(h_0-1)^3 - (q+v_s\Delta t)^3-(s+v_s\Delta t)^3\right]$	A.7c
	$s < -v_0\Delta t \leq q$	$F_s = f-\frac{1}{6}\frac{h_1 h_2}{h_0^2}\left[(h_0+v_s\Delta t)^3-(h_0-1)^3 - (q+v_b\Delta t)^3\right]$	A.7b
	$q \leq -v_0\Delta t$	$F_s = f-\frac{1}{6}\frac{h_1 h_2}{h_0^2}\left[(h_0+v_s\Delta t)^3-(h_0-1)^3\right]$	A.7a
west	$v_w\Delta t \leq 1-t$	$F_w = \frac{1}{6}\frac{h_0 h_2}{h_1^2}\left[(h_1-1+v_w\Delta t)^3-(h_1-1)^3\right]$	
	$1-t < v_w\Delta t \leq 1-r$	$F_w = \frac{1}{6}\frac{h_0 h_2}{h_1^2}\left[(h_1+v_w\Delta t-1)^3-(h_1-1)^3 - (t+v_w\Delta t-1)^3\right]$	
	$1-r < v_w\Delta t$	$F_w = \frac{1}{6}\frac{h_0 h_2}{h_1^2}\left[(h_1+v_w\Delta t-1)^3-(h_1-1)^3 - (t+v_w\Delta t-1)^3-(t+v_w\Delta-1)^3\right]$	
east	$-v_e\Delta t \leq r$	$F_e = f-\frac{1}{6}\frac{h_0 h_2}{h_1^2}\left[(h_1+v_e\Delta t)^3-(h_1-1)^3 - (t+v_e\Delta t)^3-(r+v_e\Delta t)^3\right]$	
	$r < -v_e\Delta t \leq t$	$F_e = f-\frac{1}{6}\frac{h_0 h_2}{h_1^2}\left[(h_1+v_e\Delta t)^3-(h_1-1)^3 - (t+v_e\Delta t)^3\right]$	
	$t < -v_e\Delta t$	$F_e = f-\frac{1}{6}\frac{h_0 h_2}{h_1^2}\left[(h_1+v_e\Delta t)^3-(h_1-1)^3\right]$	
top	$v_t\Delta t \leq 1-u$	$F_t = \frac{1}{6}\frac{h_0 h_1}{h_2^2}\left((h_2+v_t\Delta t-1)^3-(h_2-1)^3\right)$	
	$1-u < v_t\Delta t \leq 1-p$	$F_t = \frac{1}{6}\frac{h_0 h_1}{h_2^2}\left[(h_2+v_t\Delta t-1)^3-(h_2-1)^3 - (u+v_t\Delta t-1)^3\right]$	
	$1-p < v_t\Delta t$	$F_t = \frac{1}{6}\frac{h_0 h_1}{h_2^2}\left[(h_2+v_t\Delta t-1)^3-(h_2-1)^3 - (p+v_t\Delta t-1)^3-(u+v_t\Delta t-1)^3\right]$	
bottom	$-v_b\Delta t \leq p$	$F_b = f-\frac{1}{6}\frac{h_0 h_1}{h_2^2}\left[(h_2+v_b\Delta t)^3-(h_2-1)^3 - (p+v_b\Delta t)^3-(u+v_b\Delta)^3\right]$	
	$p < -v_b\Delta t \leq u$	$F_b = f-\frac{1}{6}\frac{h_0 h_1}{h_2^2}\left[(h_2+v_b\Delta t)^3-(h_2-1)^3 - (u+v_b\Delta t)^3\right]$	
	$u < -v_b\Delta t$	$F_b = f-\frac{1}{6}\frac{h_0 h_1}{h_2^2}\left[(h_2+v_b\Delta t)^3-(h_2-1)^3\right]$	

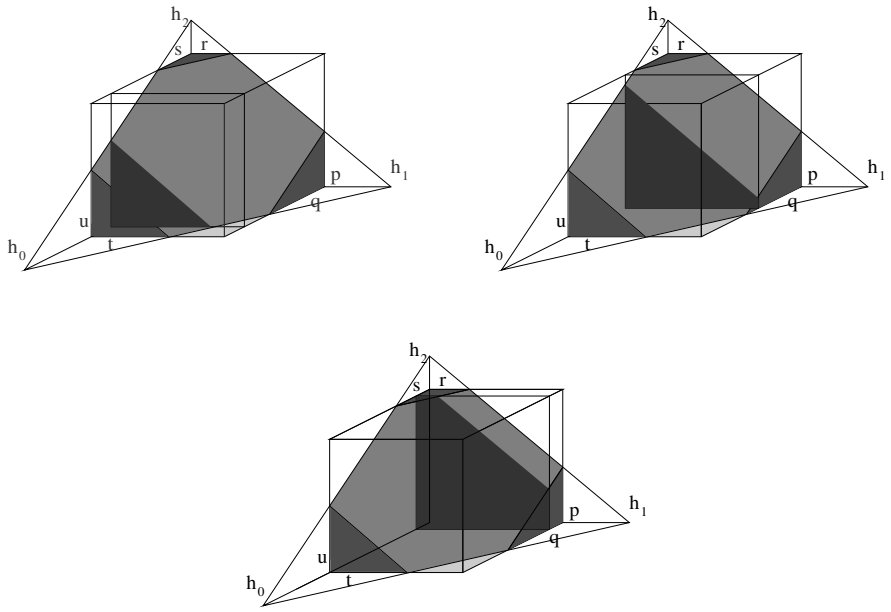

Figure A.7: Type 4 flux through north or south face.

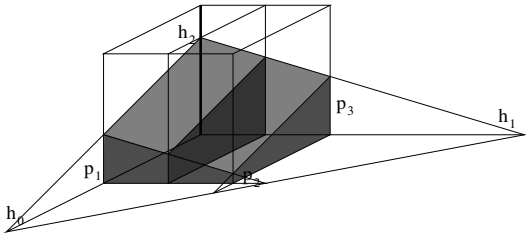

Figure A.8: Type 5 flux though north or south face.

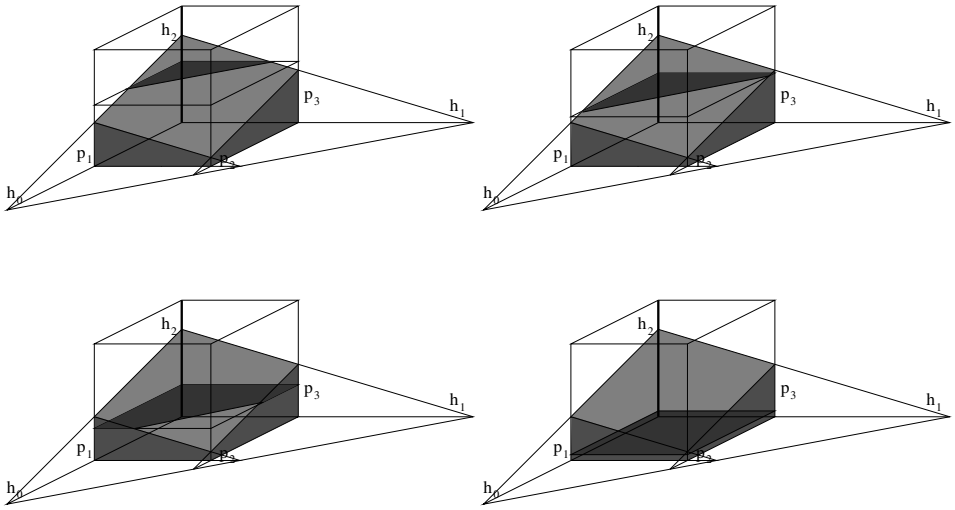

Figure A.9: Type 5 flux through top or bottom face.

Table A.6: Fluxes for type 5 surface element.

cell face	criteria	flux	figure
north		$F_n = \frac{1}{4}\left\|v_n\right\| \Delta t \left(P_1 + P_2 + P_3 + P_4\right)$ with $P_1 = h_2 - \frac{h_2}{h_0}$ $P_2 = h_2 - \frac{h_2}{h_1} - \frac{h_2}{h_0}$ $P_3 = P_1 + v_n \Delta t \frac{h_2}{h_0}$ $P_4 = P_2 + v_n \Delta t \frac{h_2}{h_0}$	
south		$F_s = \frac{1}{4}\left\|v_s\right\| \Delta t \left(P_1 + P_2 + P_3 + P_4\right)$ with $P_1 = h_2$ $P_2 = h_2 - \frac{h_2}{h_1}$ $P_3 = P_1 + v_s \Delta t \frac{h_2}{h_0}$ $P_4 = P_2 + v_s \Delta t \frac{h_2}{h_0}$	
west		$F_w = \frac{1}{4}\left\|v_w\right\| \Delta t \left(P_1 + P_2 + P_3 + P_4\right)$ with $P_1 = h_2 - \frac{h_2}{h_0}$ $P_2 = h_2 - \frac{h_2}{h_1} - \frac{h_2}{h_0}$ $P_3 = P_1 + v_n \Delta t \frac{h_2}{h_1}$ $P_4 = P_2 + v_n \Delta t \frac{h_2}{h_1}$	A.8
east		$F_e = \frac{1}{4}\left\|v_n\right\| \Delta t \left(P_1 + P_2 + P_3 + P_4\right)$ with $P_1 = h_2$ $P_2 = h_2 - \frac{h_2}{h_0}$ $P_3 = P_1 + v_e \Delta t \frac{h_2}{h_1}$ $P_4 = P_2 + v_e \Delta t \frac{h_2}{h_1}$	A.8
top	$v_t \Delta t \leq 1 - h_2$	$F_t = 0$	
	$1 - h_2 < v_t \Delta t \leq 1 - p_1$	$F_t = \frac{1}{6}\left(xyz\right)$ with $z = h_2 + v_t \Delta t - 1$ $x = z\frac{h_0}{h_2}$ $y = z\frac{h_1}{h_2}$	A.9a
	$1 - p_1 < v_t \Delta t \leq 1 - p_3$	$F_t = \frac{xyz}{6}\left[1 - \left(\frac{x-1}{x}\right)^3\right]$ with $z = h_2 + v_t \Delta t - 1$ $x = z\frac{h_0}{h_2}$ $y = z\frac{h_1}{h_2}$	A.9b
	$1 - p_3 < v_t \Delta t \leq 1 - p_2$	$F_t = \frac{1}{6} xyz \left[1 - \left(\frac{y-1}{y}\right)^3 - \left(\frac{x-1}{x}\right)^3\right]$	A.9c
	$1 - h_2 < v_t \Delta t$	$F_b = f - (1 - v_2 \Delta t)$	A.9d

Table A.7: Fluxes for type 5 surface element.(continued)

cell face	criteria	flux	figure
bottom	$-v_b\Delta t \leq p_2$	$F_b = -v_b\Delta t$	A.9d
	$p_2 < -v_b\Delta t \leq p_3$	$F_b = f - \frac{xyz}{6}\left[1 - \left(\frac{x-1}{x}\right)^3 - \left(\frac{y-1}{y}\right)^3\right]$ with $z = h_2 + v_b\Delta t$ $x = z\frac{h_0}{h_2}$ $y = z\frac{h_1}{h_2}$	A.9c
	$p_3 < -v_b\Delta t \leq p_1$	$F_b = f - \frac{xyz}{6}\left[1 - \left(\frac{x-1}{x}\right)^3\right]$ with $z = h_2 + v_b\Delta t$ $x = z\frac{h_0}{h_2}$ $y = z\frac{h_1}{h_2}$	A.9b
	$p_1 < -v_b\Delta t \leq h_2$	$F_b = f - \frac{1}{6}xyz$ with $z = h_2 + v_b\Delta t$ $x = z\frac{h_0}{h_2}$ $y = z\frac{h_1}{h_2}$	A.9a
	$h_2 < -v_b\Delta t$	$F_b = f$	

Appendix B

Translation

In this appendix the forward and backward rotation and translation of the interface element is explained. The forward translation is meant to place the surface elements in one *standard case position*. This involves only changes in the sign and the values of the vector components within the vector. By backward translation, the transition from the *standard case position* to the original orientation is meant. This involved the fluxes and tangent vectors needed for the new surface tension model.

B.1 Forward translation

In this section the steps taken to place the interface in a *standard case position* are explained. To limit the number of surface elements types to five , there is a need to only have positive components in de normal to the interface $\vec{n}$ and that the distance between the origin of the cell and the intersection points of the interface with the axis are in a certain order. This is done in two steps.

In the first step all components of $\vec{n}$ are made positive. This ensures that the liquid volume is always in the same corner as the origin of the cell. When a component of the original vector is negative the absolute value is taken and at the same time the the translation is registered in the variable rx,ry or rz for every cell.

The second step is to place the surface element in such a way that the largest

distance between the origin of the cell and the intersection point of the axis and the interface is at the x-axis, the middle one at the y-axis and shortest is along the z-axis. Because this length is proportional to $\frac{1}{n_i}$ this is done by putting the shortest vector component at the position of the x-component, the middle one at the position of the y-component and finally the largest at the position of the z-component. This rotation is again registered for every cell. This is done in the variable rnx,rny and rnz.

In the *standard case position* the axis are not called x,y and z but, for the sake of clarity, 0, 1 and 2. So if the shortest distance between origin and intersection point is on the x-axis, it is transfered to the 2-axis and $rnx = 2$.

In this way, the normal is given such a direction that the surface element is always in the *standard case position* and all the information about the translation is stored in rx,ry,rz and rnx,rny and rnz.

Once this translation is known, the velocities on all cell faces are rotated also. This is done for every cell just before the calculation of the fluxes through the cell faces.

B.2 Backward translation of fluxes

Once the fluxes for the *standard case position* are calculated, they must be re-translated to the original system. This is again done in two steps, but now in reverse order. First the axis are put on the real position and second the direction is fluxes are assigned to the right positive and negative cell faces.

If for example the $rnx = 2$ and $rx = -1$ than first the fluxes calculated in the *standard case position* for the top and the bottom of the cell are assigned to the north and the south respectively. $rx = -1$ means that in the original system the volume fraction was situated opposite of the origen of the cell. So the back and front flux are swapped.

B.3 Backward translation of the tangent vectors

The new proposed surface tension model needs tangent vectors along the edge of the surface elements. These tangent vectors are calculated during the type selection. Since this is done for a *standard case position*, these vectors are also given in *standard case position*. In this section the translation of these vectors to the original system is given. This is just like in the last section done in two steps. First the vectors are translated to right axis and secondly the are swapped if needed.

B.3.1 Translation to original axis

In this re-translation there are six possible options. The first one is made visible in figure B.1. If the 0-axis has to be transformed to the z-axis , two options stay open. The first one is the the 2-axis is being transformed to the x-axis and the 1-axis stays where it is (middle), or the 3-axis is transformed to the y-axis and the 1-axis is transformed to the x-axis(right).

The transformation of the vector is given in table B.1. In this table the vector on $i + \frac{1}{2}$ is called $\vec{t}_{north}$, on $i - \frac{1}{2}$ is called $\vec{t}_{south}$, $j + \frac{1}{2}$ is called $\vec{t}_{east}$ etc.

B.3.2 Swapping the back and front.

During the translation only the sides of the cell were changed (if needed). ($i + \frac{1}{2}$ was changed with $i - \frac{1}{2}$, $j - \frac{1}{2}$ was changed with $j + \frac{1}{2}$, etc.) In the tables B.2, B.3 and B.4 the translation to be performed are given. On the top row of each table the new tangent vector is indicated. In the second row it is explained how this vector is constructed.

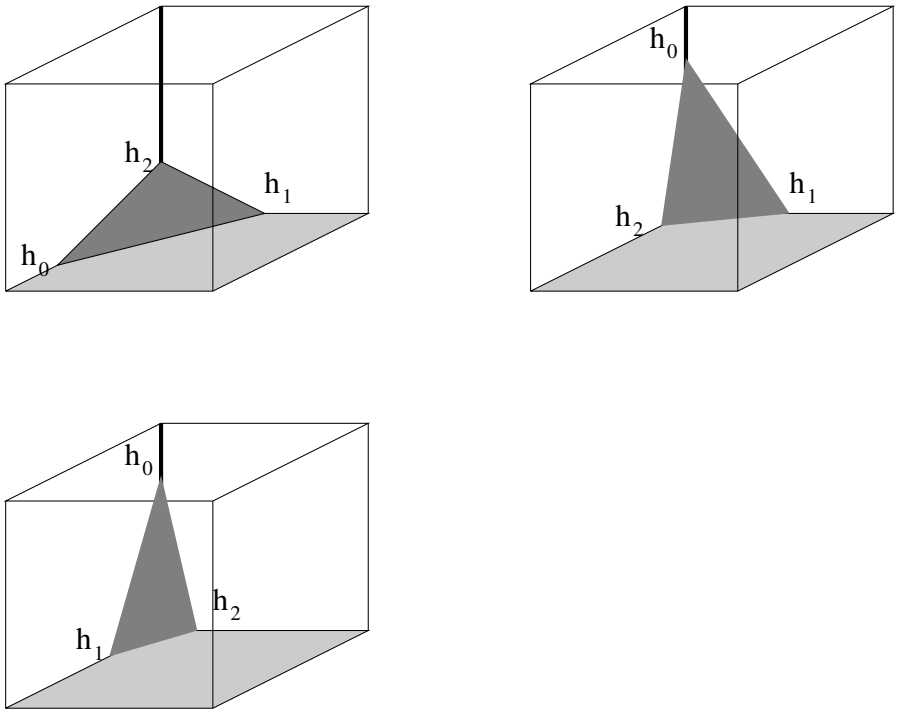

Figure B.1: without translation(left top) with two possible rotations(right top and lower)

	$\vec{t}_{north}$	$\vec{t}_{south}$	$\vec{t}_{east}$	$\vec{t}_{west}$	$\vec{t}_{top}$	$\vec{t}_{bottom}$
$0 \to x$ $1 \to y$ $2 \to z$	$\begin{pmatrix} 0 \\ t_{north,y} \\ t_{north,z} \end{pmatrix}$	$\begin{pmatrix} 0 \\ t_{south,y} \\ t_{south,z} \end{pmatrix}$	$\begin{pmatrix} t_{east,x} \\ 0 \\ t_{east,z} \end{pmatrix}$	$\begin{pmatrix} t_{west,x} \\ 0 \\ t_{west,z} \end{pmatrix}$	$\begin{pmatrix} t_{top,x} \\ t_{top,y} \\ 0 \end{pmatrix}$	$\begin{pmatrix} t_{bottom,x} \\ t_{bottom,y} \\ 0 \end{pmatrix}$
$0 \to x$ $1 \to z$ $2 \to y$	$\begin{pmatrix} 0 \\ -t_{north,z} \\ -t_{north,y} \end{pmatrix}$	$\begin{pmatrix} 0 \\ -t_{south,z} \\ -t_{south,y} \end{pmatrix}$	$\begin{pmatrix} -t_{bottom,x} \\ 0 \\ -t_{bottom,y} \end{pmatrix}$	$\begin{pmatrix} -t_{top,x} \\ 0 \\ -t_{top,y} \end{pmatrix}$	$\begin{pmatrix} -t_{west,x} \\ -t_{west,z} \\ 0 \end{pmatrix}$	$\begin{pmatrix} -t_{east,x} \\ -t_{east,z} \\ 0 \end{pmatrix}$
$0 \to y$ $1 \to z$ $2 \to x$	$\begin{pmatrix} 0 \\ t_{top,x} \\ t_{top,y} \end{pmatrix}$	$\begin{pmatrix} 0 \\ t_{bottom,x} \\ t_{bottom,y} \end{pmatrix}$	$\begin{pmatrix} t_{south,z} \\ 0 \\ t_{south,y} \end{pmatrix}$	$\begin{pmatrix} t_{north,z} \\ 0 \\ t_{north,y} \end{pmatrix}$	$\begin{pmatrix} t_{east,z} \\ t_{east,x} \\ 0 \end{pmatrix}$	$\begin{pmatrix} t_{east,z} \\ t_{east,x} \\ 0 \end{pmatrix}$
$0 \to y$ $1 \to x$ $2 \to z$	$\begin{pmatrix} 0 \\ -t_{west,x} \\ -t_{west,z} \end{pmatrix}$	$\begin{pmatrix} 0 \\ -t_{east,x} \\ -t_{east,z} \end{pmatrix}$	$\begin{pmatrix} -t_{south,y} \\ 0 \\ -t_{south,z} \end{pmatrix}$	$\begin{pmatrix} -t_{north,y} \\ 0 \\ -t_{north,z} \end{pmatrix}$	$\begin{pmatrix} -t_{top,y} \\ -t_{top,x} \\ 0 \end{pmatrix}$	$\begin{pmatrix} -t_{bottom,y} \\ -t_{bottom,x} \\ 0 \end{pmatrix}$
$0 \to z$ $1 \to x$ $2 \to y$	$\begin{pmatrix} 0 \\ t_{west,z} \\ t_{west,x} \end{pmatrix}$	$\begin{pmatrix} 0 \\ t_{east,z} \\ t_{east,x} \end{pmatrix}$	$\begin{pmatrix} t_{bottom,y} \\ 0 \\ t_{bottom,x} \end{pmatrix}$	$\begin{pmatrix} t_{top,y} \\ 0 \\ t_{top,x} \end{pmatrix}$	$\begin{pmatrix} t_{north,y} \\ t_{north,z} \\ 0 \end{pmatrix}$	$\begin{pmatrix} t_{south,y} \\ t_{south,z} \\ 0 \end{pmatrix}$
$0 \to z$ $1 \to y$ $2 \to x$	$\begin{pmatrix} 0 \\ -t_{top,y} \\ -t_{top,x} \end{pmatrix}$	$\begin{pmatrix} 0 \\ -t_{bottom,y} \\ -t_{bottom,x} \end{pmatrix}$	$\begin{pmatrix} -t_{east,z} \\ 0 \\ -t_{east,x} \end{pmatrix}$	$\begin{pmatrix} -t_{west,z} \\ 0 \\ -t_{west,x} \end{pmatrix}$	$\begin{pmatrix} -t_{north,z} \\ -t_{north,y} \\ 0 \end{pmatrix}$	$\begin{pmatrix} -t_{south,z} \\ -t_{south,y} \\ 0 \end{pmatrix}$

Table B.1: summary of all re-translations

$\vec{t}_{north}$	$\vec{t}_{south}$	$\vec{t}_{east}$	$\vec{t}_{west}$	$\vec{t}_{top}$	$\vec{t}_{bottom}$
$\begin{pmatrix} 0 \\ -t_{south,y} \\ -t_{south,z} \end{pmatrix}$	$\begin{pmatrix} 0 \\ -t_{north,y} \\ -t_{north,z} \end{pmatrix}$	$\begin{pmatrix} t_{east,x} \\ 0 \\ -t_{east,z} \end{pmatrix}$	$\begin{pmatrix} t_{west,x} \\ 0 \\ -t_{west,z} \end{pmatrix}$	$\begin{pmatrix} t_{top,x} \\ -t_{top,y} \\ 0 \end{pmatrix}$	$\begin{pmatrix} t_{bottom,x} \\ -t_{bottom,y} \\ 0 \end{pmatrix}$

Table B.2: summary of re-translations north-south change

$\vec{t}_{north}$	$\vec{t}_{south}$	$\vec{t}_{east}$	$\vec{t}_{west}$	$\vec{t}_{top}$	$\vec{t}_{bottom}$
$\begin{pmatrix} 0 \\ t_{north,y} \\ -t_{north,z} \end{pmatrix}$	$\begin{pmatrix} 0 \\ t_{south,y} \\ -t_{south,z} \end{pmatrix}$	$\begin{pmatrix} -t_{west,x} \\ 0 \\ -t_{west,z} \end{pmatrix}$	$\begin{pmatrix} -t_{east,x} \\ 0 \\ -t_{east,z} \end{pmatrix}$	$\begin{pmatrix} -t_{top,x} \\ t_{top,y} \\ 0 \end{pmatrix}$	$\begin{pmatrix} -t_{bottom,x} \\ t_{bottom,y} \\ 0 \end{pmatrix}$

Table B.3: summary of re-translations east-west change

$\vec{t}_{north}$	$\vec{t}_{south}$	$\vec{t}_{east}$	$\vec{t}_{west}$	$\vec{t}_{top}$	$\vec{t}_{bottom}$
$\begin{pmatrix} 0 \\ -t_{north,y} \\ t_{north,z} \end{pmatrix}$	$\begin{pmatrix} 0 \\ -t_{south,y} \\ t_{south,z} \end{pmatrix}$	$\begin{pmatrix} -t_{east,x} \\ 0 \\ t_{east,z} \end{pmatrix}$	$\begin{pmatrix} -t_{west,x} \\ 0 \\ t_{west,z} \end{pmatrix}$	$\begin{pmatrix} -t_{bottom,x} \\ -t_{bottom,y} \\ 0 \end{pmatrix}$	$\begin{pmatrix} -t_{top,x} \\ -t_{top,y} \\ 0 \end{pmatrix}$

Table B.4: summary of re-translations top-bottom change

Appendix C

Results for the parameter study with the Front Tracking model

In this appendix the *Front Tracking* figures referred to in table 4.3 and table 4.1 are given. In figure C.1 the diagram of Grace (1973) is given with the approximate points that were computed here.

In the figures below, the left side graph presents the final (steady state) shape of the bubble, while the graph on the right side shows the bubble velocity in x, y and z-direction as a function of time. The simulation was stopped when a steady velocity was reached.

For all simulations the gas properties of were used (see table C.1. The selected liquid properties are given in the figures legend.

Table C.1: Physical data of air used in the simulations.

ρ	$1.293\ kg/m^3$
μ	$17.1 \cdot 10^{-6}\ Pa.s$

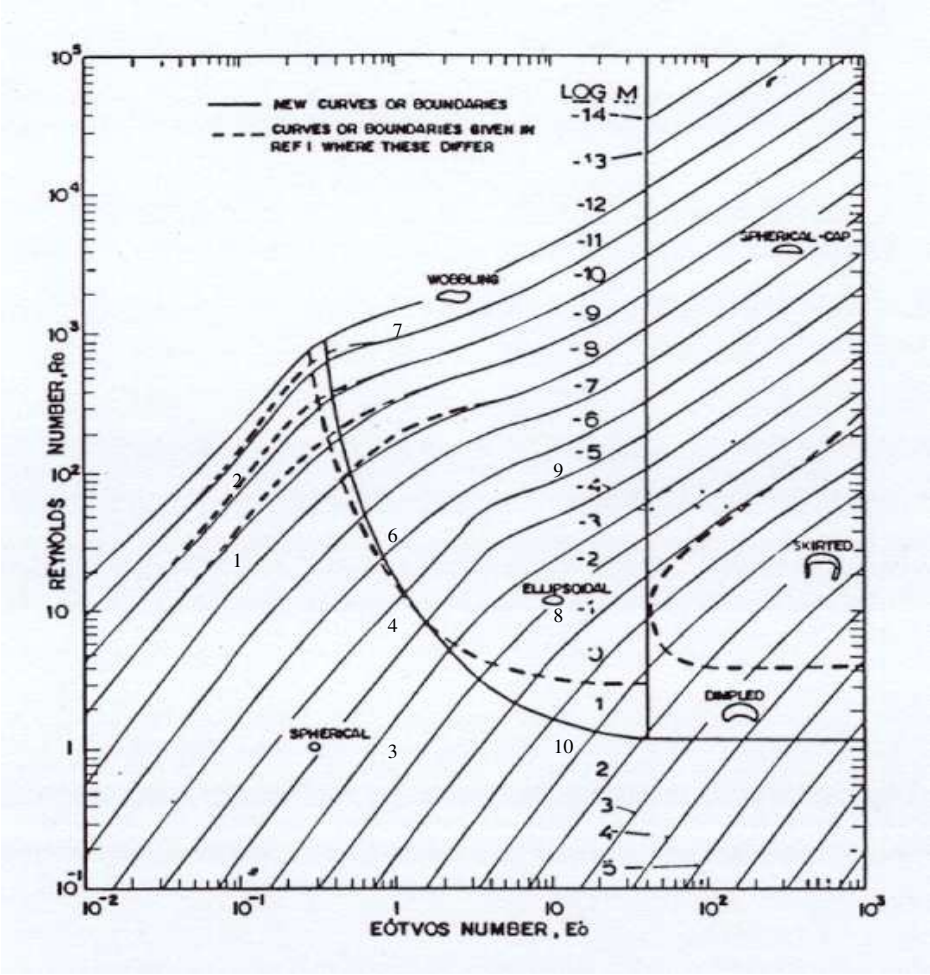

Figure C.1: Grace's diagram with the position of the cases for which simulations were carried out.

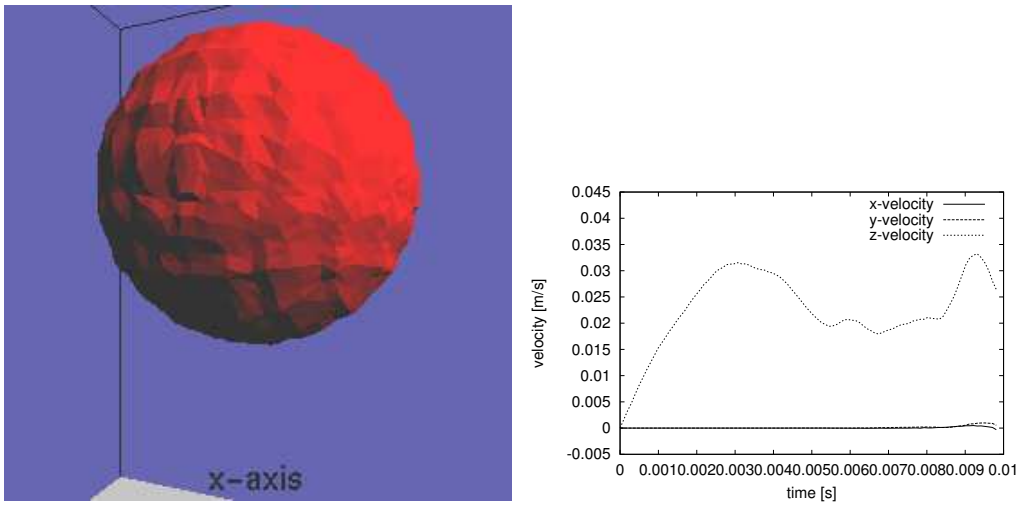

Figure C.2: Case 1: liquid parameters : $\rho = 864\ kg/m^3$, $\mu = 1.46 \cdot 10^{-3}\ Pa.s$, $\sigma = 0.0278\ N/m$. Dimensionless numbers : $Eo = 0.1$ and $\log(Mo) = -8.6$.

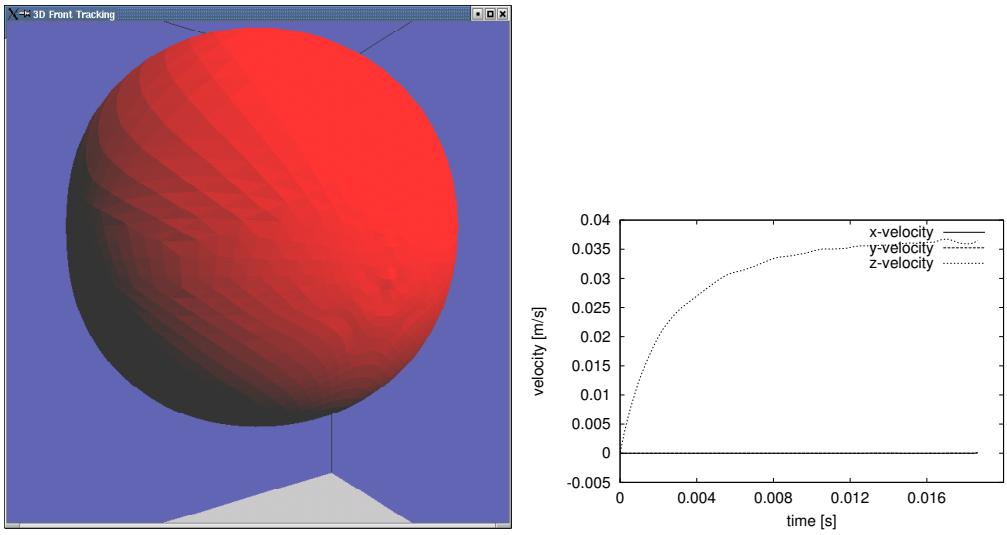

Figure C.3: Case 3: liquid parameters : $\rho = 886\ kg/m^3$, $\mu = 5.80 \cdot 10^{-2}\ Pa.s$, $\sigma = 0.0207\ N/m$. Dimensionless numbers : $Eo = 1.0$ and $\log(Mo) = -1.8$.

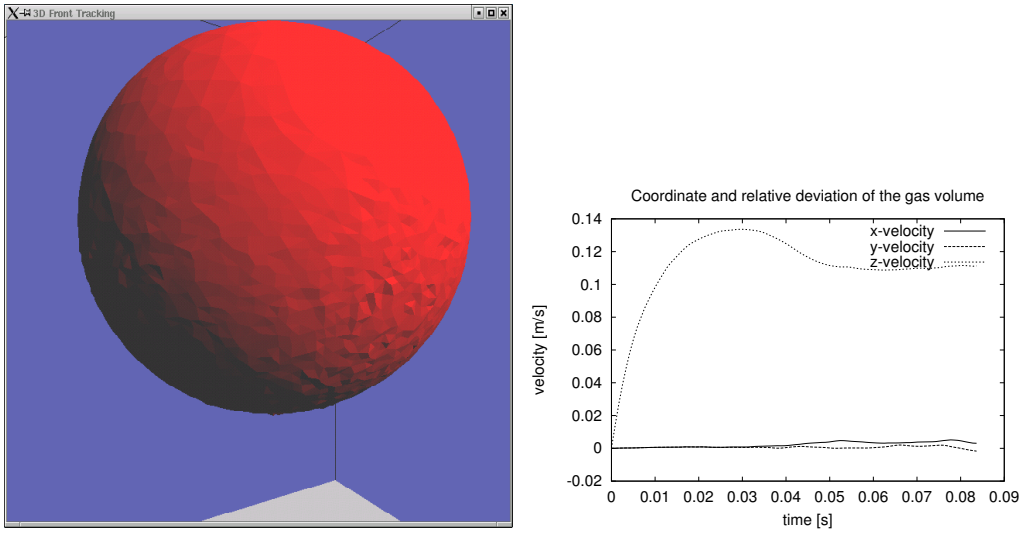

Figure C.4: Case 4: liquid parameters : $\rho = 1262\ kg/m^3$, $\mu = 5.50{\cdot}10^{-2}\ Pa.s$, $\sigma = 0.0792\ N/m$. Dimensionless numbers : $Eo = 1.0$ and $\log(Mo) = -3.8$.

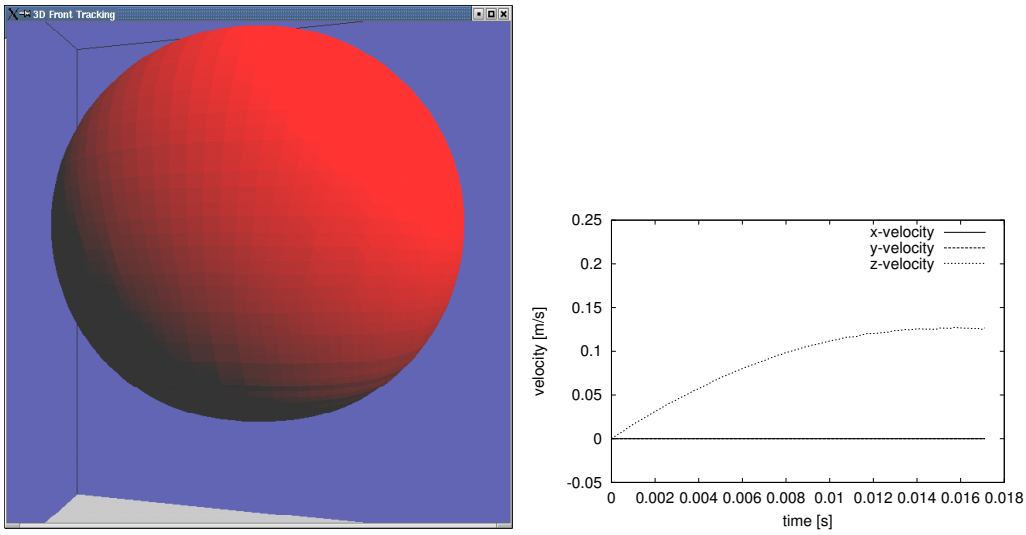

Figure C.5: Case 5:liquid parameters : $\rho = 1380\ kg/m^3$, $\mu = 1.04{\cdot}10^{+1}\ Pa.s$, $\sigma = 0.0956\ N/m$. Dimensionless numbers : $Eo = 10.0$ and $\log(Mo) = 5$.

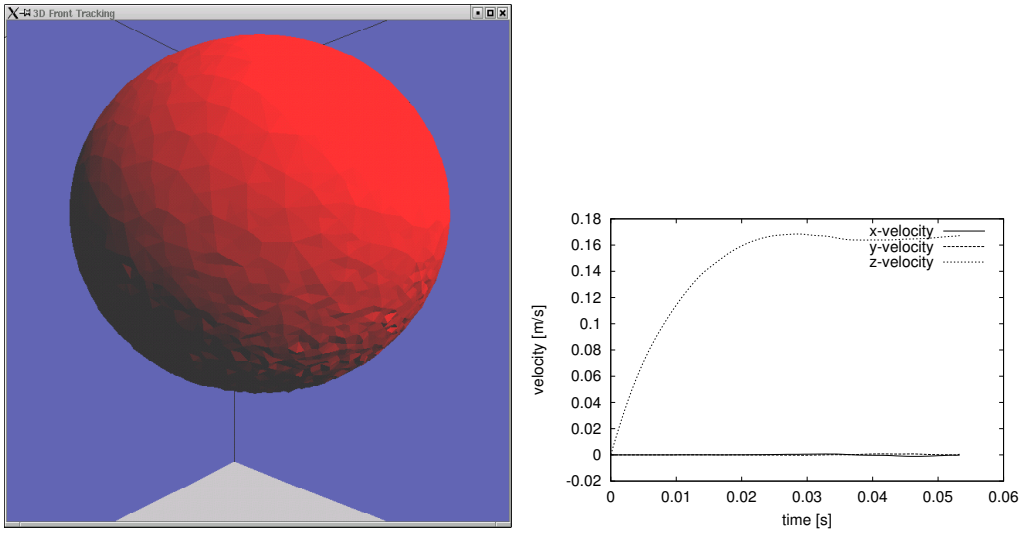

Figure C.6: case 6: liquid parameters : $\rho = 813\ kg/m^3$, $\mu = 5.6 \cdot 10^{-3}\ Pa.s$, $\sigma = 0.0245\ N/m$. Dimensionless numbers : $Eo = 1.0$ and $\log(Mo) = -6.1$.

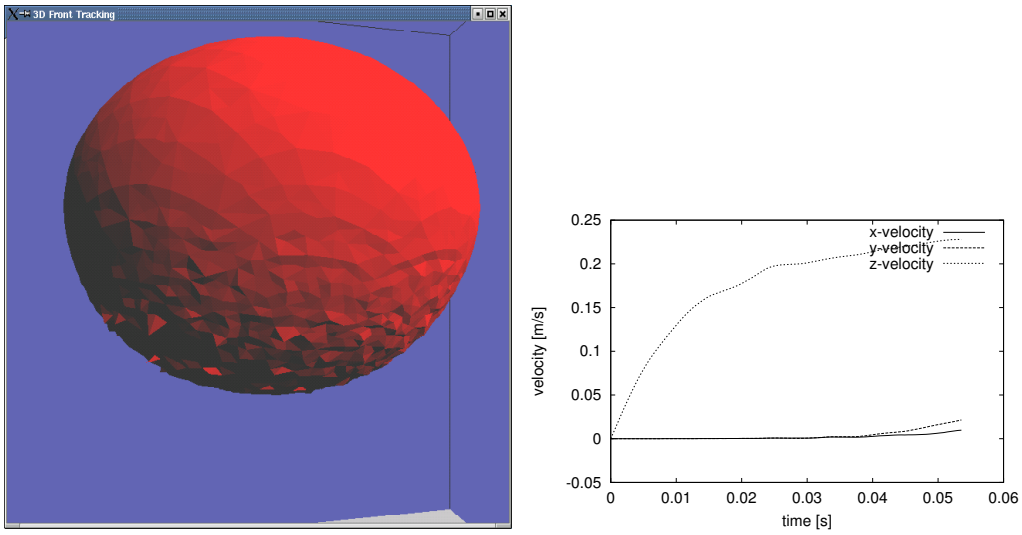

Figure C.7: case 7: liquid parameters : $\rho = 723\ kg/m^3$, $\mu = 2.33 \cdot 10^{-4}\ Pa.s$, $\sigma = 0.0159\ N/m$. Dimensionless numbers : $Eo = 1.0$ and $\log(Mo) = -11$.

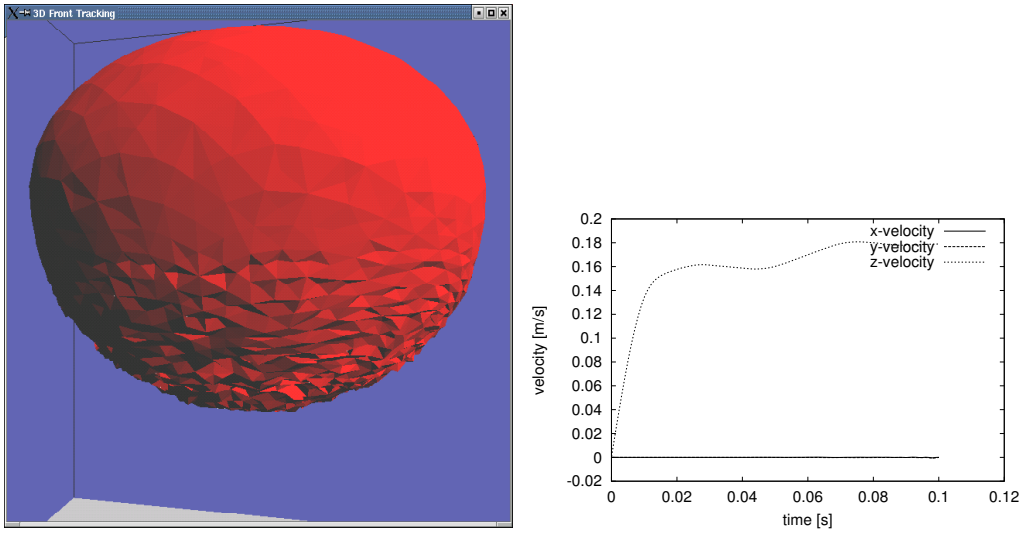

Figure C.8: Case 8: liquid parameters : $\rho = 866\ kg/m^3$, $\mu = 5.80 \cdot 10^{-2}\ Pa.s$, $\sigma = 0.0207\ N/m$. Dimensionless numbers : $Eo = 10.0$ and $\log(Mo) = -1.84$.

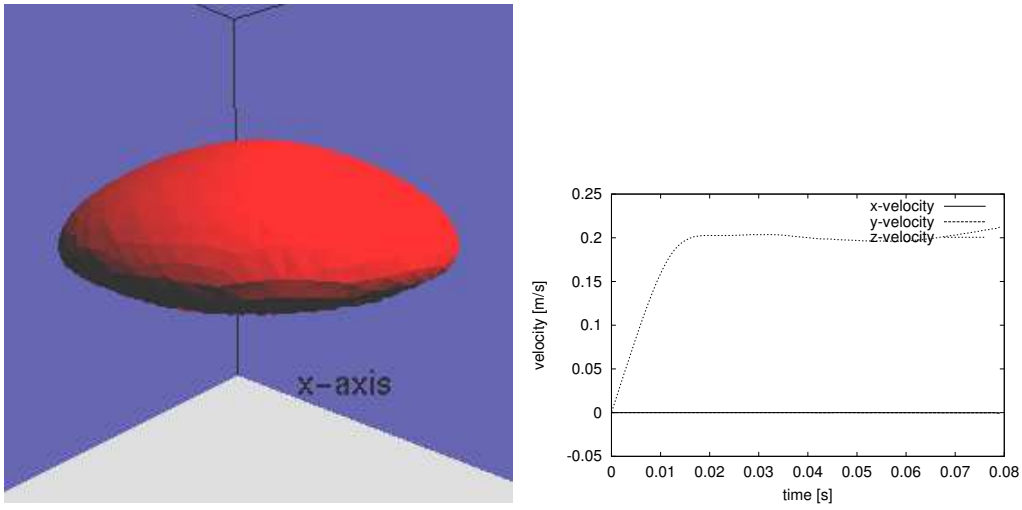

Figure C.9: Case 9: liquid parameters : $\rho = 1230\ kg/m^3$, $\mu = 2.37 \cdot 10^{-2}\ Pa.s$, $\sigma = 0.0759\ N/m$. Dimensionless numbers : $Eo = 10.0$ and $\log(Mo) = -5.24$.

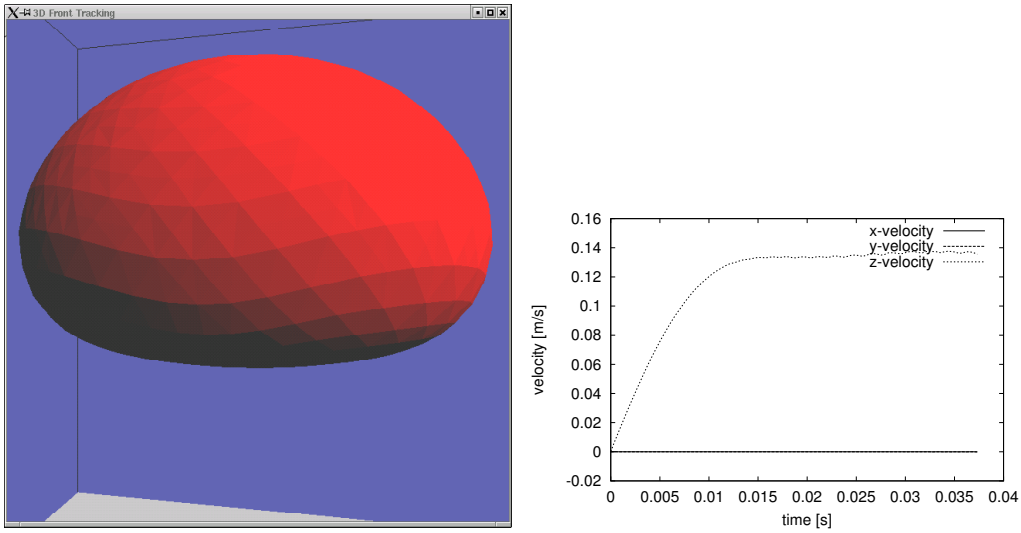

Figure C.10: Case 10: liquid parameters : $\rho = 880\ kg/m^3$, $\mu = 2.94 \cdot 10^{-1}\ Pa.s$, $\sigma = 0.0280\ N/m$. Dimensionless numbers : $Eo = 10.0$ and $\log(Mo) = 0.58$.

Appendix D

Results for the parameter study with the Volume of Fluid model

In this appendix the *VoF* figures refered to in table 4.1 and table 4.3 are given. The approximate position of these simulations in the Grace-bubble diagram (Grace, 1973) is given in figure C.1. For all simulations the physical properties of air were used for the gas phase (see table D.1). Simulations were carried out until the velocity became constant.

Table D.1: Physical data of air used in the simulations.

ρ	$1.293\ kg/m^3$
μ	$17.1 \cdot 10^{-6}\ Pa \cdot s$

In the figures below, the graph on the left indicates the final shape of the bubble. The figure on the right shows the bubble velocity in x, y and z-direction.

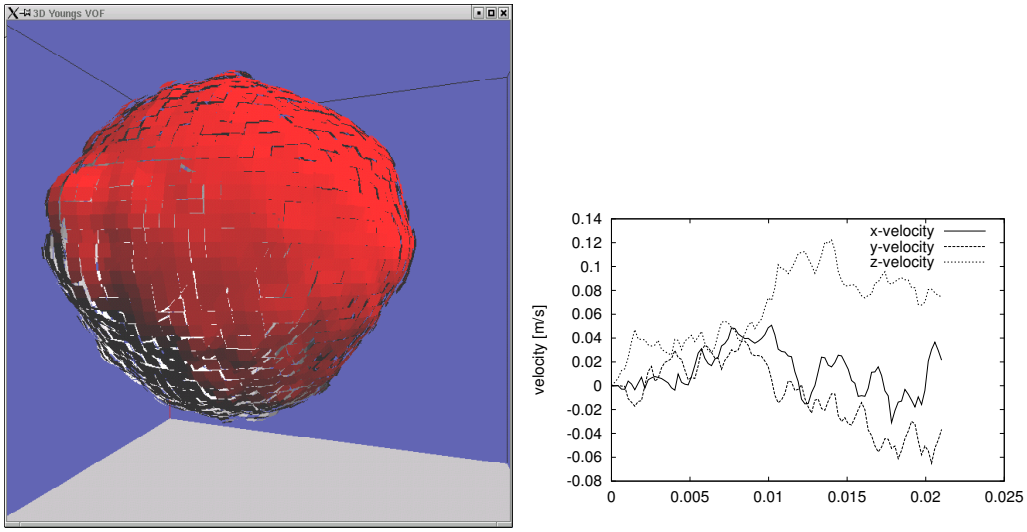

Figure D.1: Case 2: liquid parameters : $\rho = 998\ kg/m^3$, $\mu = 1.00 \cdot 10^{-3}\ Pa.s$, $\sigma = 0.0728\ N/m$. Dimensionless numbers : $Eo = 0.1$ and $\log(Mo) = -10.59$.

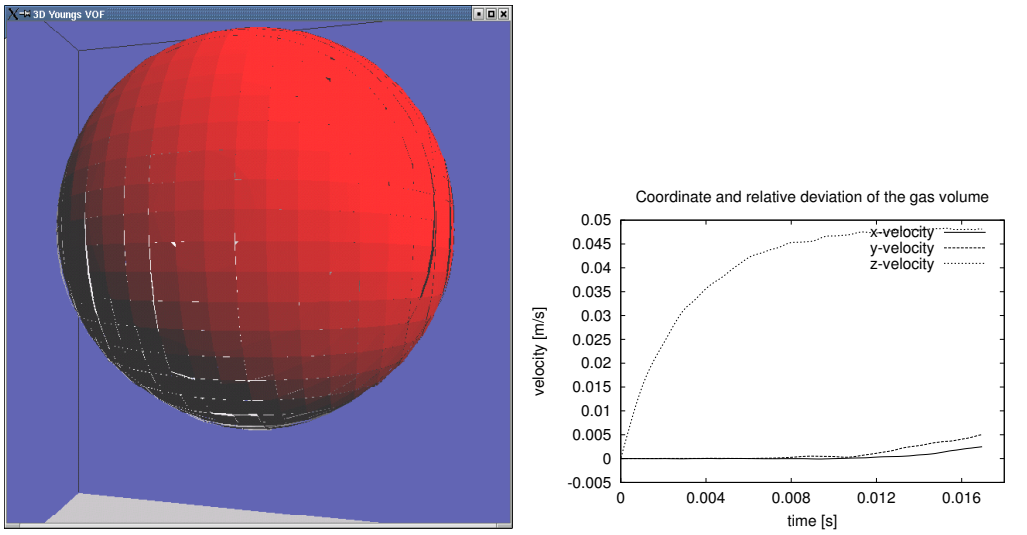

Figure D.2: Case 3: liquid parameters : $\rho = 886\ kg/m^3$, $\mu = 5.80 \cdot 10^{-2}\ Pa.s$, $\sigma = 0.0207\ N/m$. Dimensionless numbers : $Eo = 1.0$ and $\log(Mo) = -1.8$.

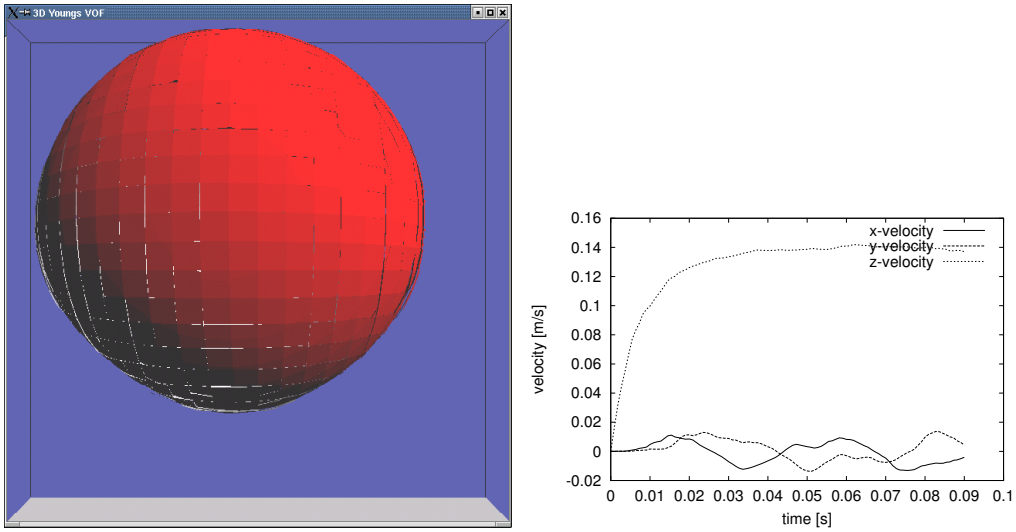

Figure D.3: Case 4: liquid parameters : $\rho = 1262\ kg/m^3$, $\mu = 5.50 \cdot 10^{-2}\ Pa.s$, $\sigma = 0.0792\ N/m$. Dimensionless numbers : $Eo = 1.0$ and $\log(Mo) = -3.8$.

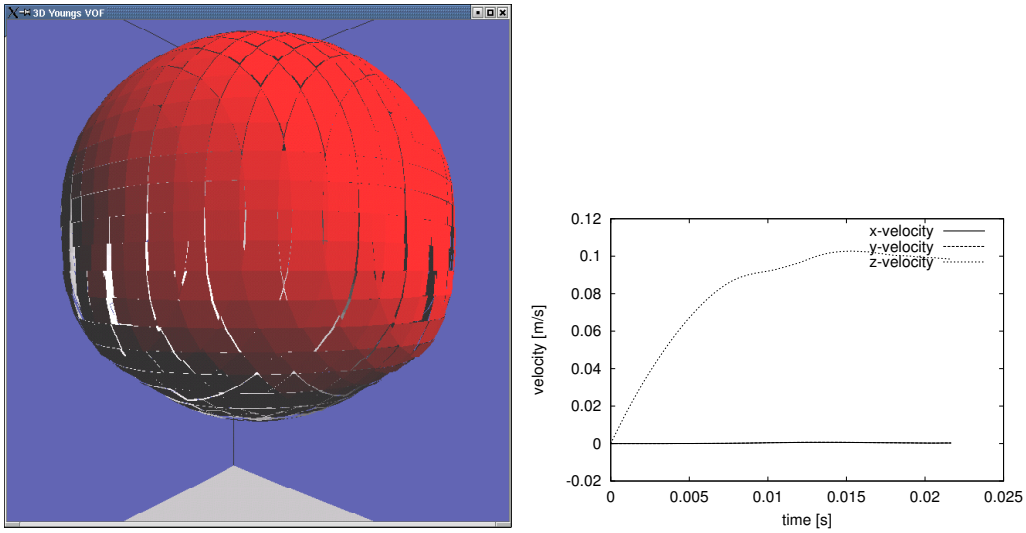

Figure D.4: Case 5: liquid parameters : $\rho = 1380\ kg/m^3$, $\mu = 1.04 \cdot 10^1\ Pa.s$, $\sigma = 0.0956\ N/m$. Dimensionless numbers : $Eo = 10.0$ and $\log(Mo) = 5.0$.

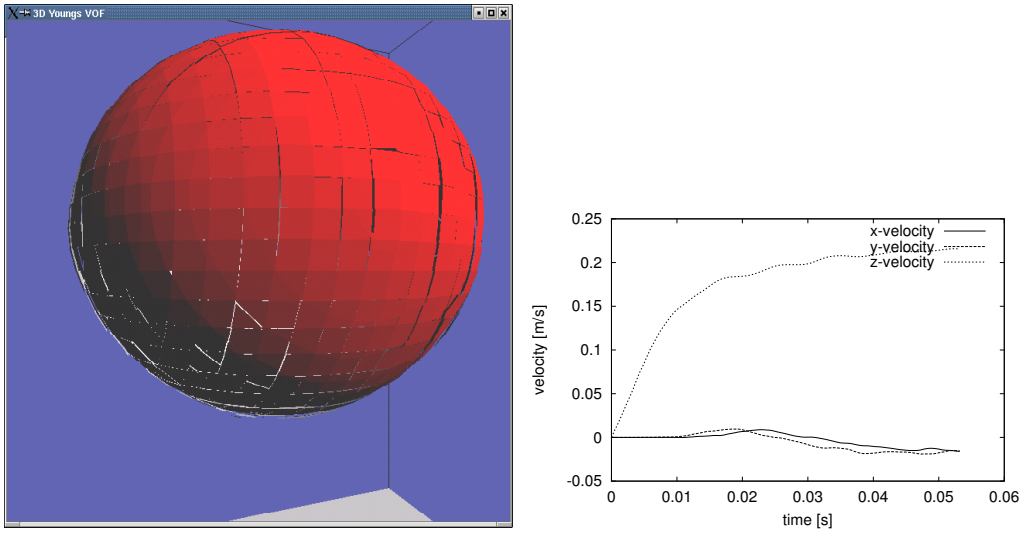

Figure D.5: Case 6: liquid parameters : $\rho = 813\ kg/m^3$, $\mu = 5.6 \cdot 10^{-3}\ Pa.s$, $\sigma = 0.0245\ N/m$. Dimensionless numbers : $Eo = 1.0$ and $\log(Mo) = -6.1$.

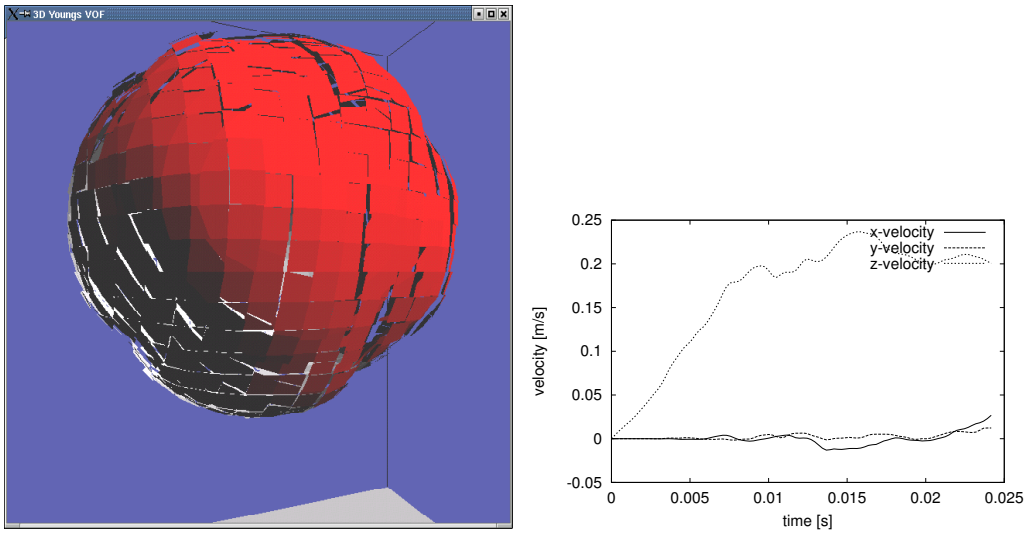

Figure D.6: Case 7: liquid parameters : $\rho = 723\ kg/m^3$, $\mu = 2.33 \cdot 10^{-4}\ Pa.s$, $\sigma = 0.0159\ N/m$. Dimensionless numbers : $Eo = 1.0$ and $\log(Mo) = -11$.

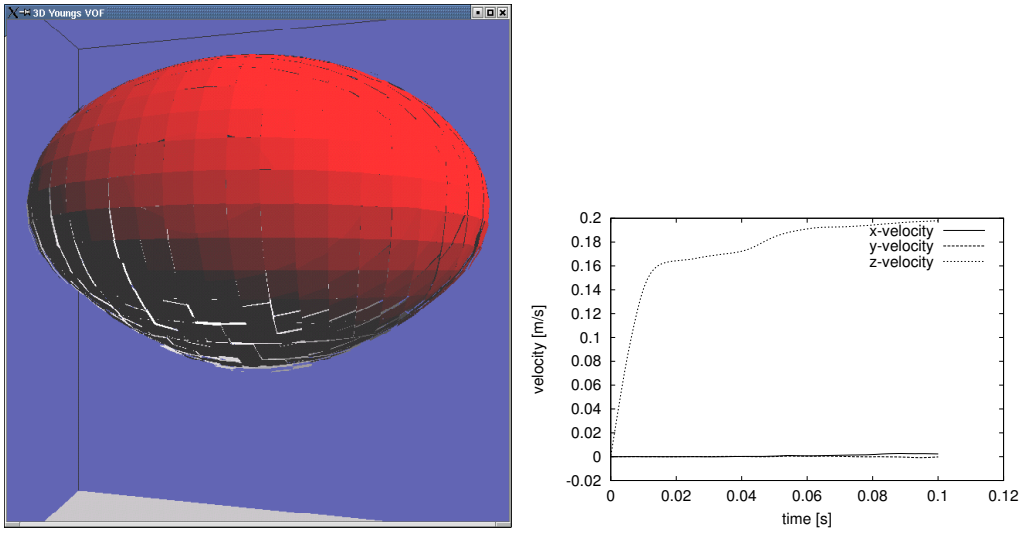

Figure D.7: Case 8: liquid parameters : $\rho = 866\ kg/m^3$, $\mu = 5.80 \cdot 10^{-2}\ Pa.s$, $\sigma = 0.0207\ N/m$. Dimensionless numbers : $Eo = 10.0$ and $\log(Mo) = -1.84$.

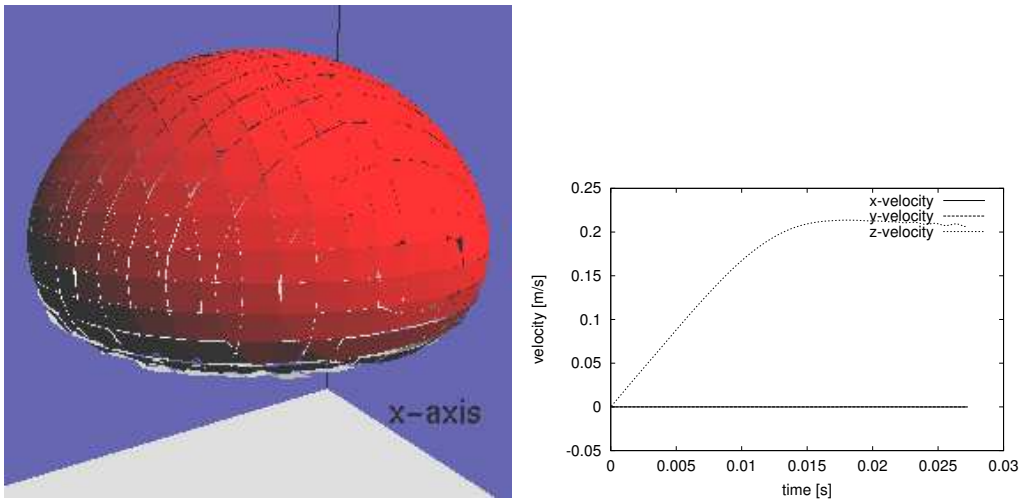

Figure D.8: Case 9: liquid parameters : $\rho = 1230\ kg/m^3$, $\mu = 2.37 \cdot 10^{-2}\ Pa.s$, $\sigma = 0.0759\ N/m$. Dimensionless numbers : $Eo = 10.0$ and $\log(Mo) = -5.24$.

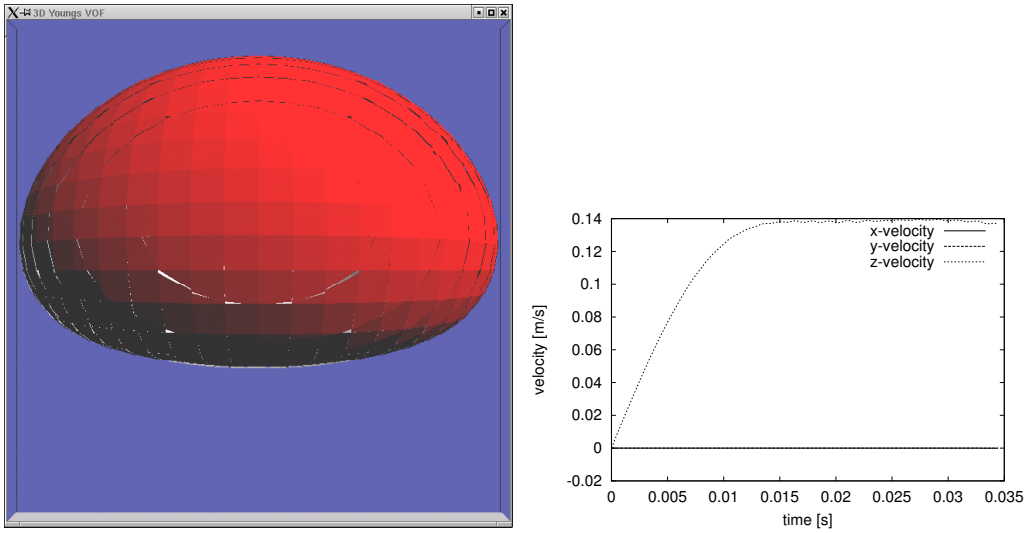

Figure D.9: Case 10: liquid parameters : $\rho = 880\ kg/m^3$, $\mu = 2.94 \cdot 10^{-1}\ Pa.s$, $\sigma = 0.0280\ N/m$. Dimensionless numbers : $Eo = 10.0$ and $\log(Mo) = 0.58$.

Appendix E

Smoothing with an integrated Peskin function

To avoid instabilities due to steep gradients near the interface the indicator function is smoothed. In our codes an integrated version of the smoothing function proposed by Peskin (1977) has been used. Peskin suggested to use the following smoothing function.

$$D\left(x-\tilde{x}\right)=\frac{1}{nh}\left(1+\cos\left(\frac{\pi}{nh}\left(x-\tilde{x}\right)\right)\right) \tag{E.1}$$

In recent years Peskin and McQueen (1994) proposed a numerical approximation of this function to reduce the computational time required for the evaluation of the indicator function, using a algebraic expression instead of the cosine function.

$$D\left(x-\tilde{x}\right)=\begin{cases} d_1\left(x-\tilde{x}\right) & if \quad |x-\tilde{x}|\leq 1 \\ \frac{1}{2}-d_1\left(2-|x-\tilde{x}|\right) & if \quad 1<|x-\tilde{x}|<2 \\ 0 & if \quad |x-\tilde{x}|\geq 2 \end{cases} \tag{E.2}$$

$$d_1(r)=\frac{3-2\,|r|+\sqrt{1+4\,|r|-4r^2}}{8} \tag{E.3}$$

However, if one of the functions is applied to a discrete domain and integrated over entire domain, it does not necessarily add up to exactly 1, because the

nodal value is assumed for the whole integration step (see figure E.1). When equation E.1 or E.2 is used, a filter must be applied to overcome overshoots or undershoots in the $f(\mathbf{x})$-field. Since this filtering effects the $f(\mathbf{x})$-field, it indirectly also effects the results of the Navier-Stokes equations. One would rather use a normalised smoothing function, so that filtering can be avoided. The smoothing function used in this study uses an integrated version of equation E.1 that does fulfill this requirement.

$$D(x-\tilde{x}) = \frac{1}{2h}\left[x_j - x_i + \frac{nh}{\pi}\left(\sin\left(\frac{\pi}{nh}(x_j-\tilde{x})\right) - \sin\left(\frac{\pi}{nh}(x_i-\tilde{x})\right)\right)\right] \quad \text{(E.4)}$$

Here x_i and x_j are the boundaries of the integration steps. The original Peskin function also uses the height at the centre of the integration step as the height of the entire step. This could lead to deviations as can clearly be seen for the most right integration step in figure E.1. The proposed function is integrated over every integration step and therefore always adds up to exactly 1. Furthermore, the original Peskin function always takes the width of the domain to be h. This holds for the $2n-2$ integration steps closest to the middle of the curve, but the two steps at the ends of the curve could be either smaller or larger (see figure E.1). It was chosen to limit the integration steps to $2n$.

In the example shown in figure E.1 the integrated function takes the integration step on the left side of the curve to start at $x = -1.8$ and end at $x = -0.5$. The width of this step is 1.3. On the other end of the curve the integration starts at $x = 1.5$ and ends at $x = 2.2$. The width of this step is only 0.7. This can be summarised as

$$x_i = \tilde{x} - nh \text{ if } x - h < \tilde{x} - nh \quad \text{(E.5)}$$

$$x_i = x - \frac{1}{2}h \text{ if } x - h \geq \tilde{x} - nh \quad \text{(E.6)}$$

$$x_j = \tilde{x} + nh \text{ if } x + h > \tilde{x} + nh \quad \text{(E.7)}$$

$$x_j = x - \frac{1}{2}h \text{ if } x + h \leq \tilde{x} + nh \quad \text{(E.8)}$$

It could be argued that the integration step in the right side interval of figure E.1 should be divided over two cells, n and $n+1$ and similarly to the left side.

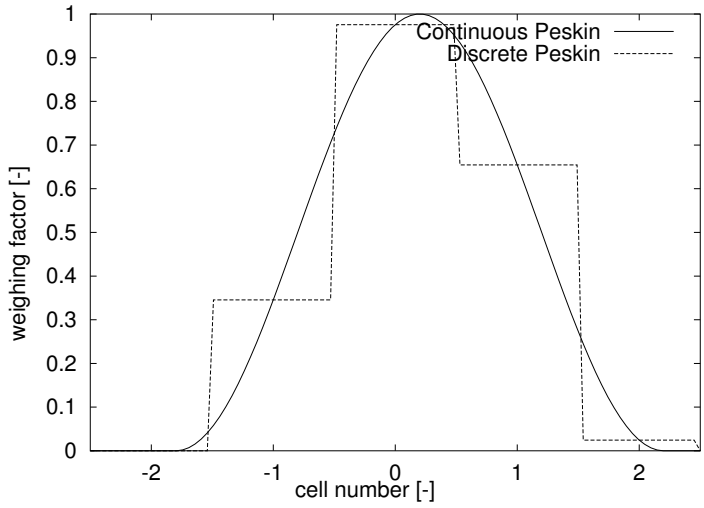

Figure E.1: Discrete Peskin function if the middle of the curve is located at 0.2 $h = 1.0$ and $n = 2$.

However, since the contribution of this last part is very small and the amount of computational work is rather large, it was chosen to add this contribution to step n (and step 1 for the left side).

In figure E.2 the relative gas losses from a rising (3.4 mm) air bubble in water, using the original Peskin function and the integrated Peskin smoothing function are shown. The type of smoothing function hardly effects the relative gas losses. It was chosen to use the integrated Peskin function for the *VoF* and the *Front Tracking* model, despite the fact that this function takes some extra computer time compared to the original function (0.18 μs/call versus 0.10 μs/call on a 1 Ghz AMD PC)

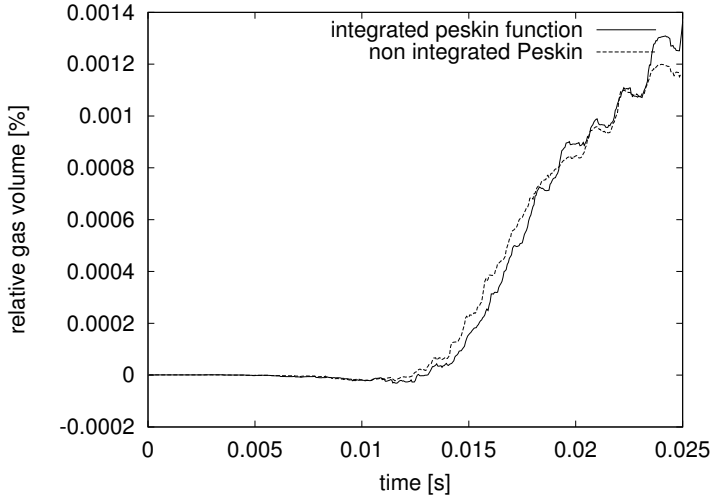

Figure E.2: Relative deviation of the gas volume of a 3.4 mm air bubble rising in water using the original Peskin or the Integrated Peskin smoothing function ($30 \times 30 \times 30$ mesh, $h = 0.226\ mm$) as a function of time.

Bibliography

T. R. Auton.
The Dynamics of Bubbles, Drops and Particles in Motion in Liquids.
PhD thesis, University of Cambridge (UK), 1983.

T. R. Auton.
The lift force on a spherical body in a rotational flow.
Journal of Fluid Mechanics, 183:199–218, 1987.

R. B. Bird, W. E. Steward, and E. N. Lightfoot.
Transport Phenomena.
John Wiley and sons, 1960.
ISBN 0-471-07395-4.

J. U. Brackbill, D. B. Kothe, and C. Zemach.
A continuum method for modeling surface tension.
Journal of Computational Physics, 100:335–354, 1992.

B. Bunner and G. Tryggvason.
Simulation of large bubble systems.
In *1997 ASME Fluids Engineering Division Summer Meeting*, Summer Meeting. ASME Fluid Engineering Division, June 1997.

J. Centrella and J. R. Wilson.
Planar numerical cosmology ii. the difference equations and numerical tests.
Astrophys. J. suppl. Ser., 54:229–249, 1984.

A. K. Chesters.
The modelling of coalescence processes in fluid-liquid dispersions: A review of current understanding.

Trans IChemE, 69(part A), July 1991.

R. Clift, J. R. Grace, and M. E. Weber.
Bubbles, Drops and Particles.
Academic Press NewYork, 1978.
ISBN 0-12-176950-X.

D. Darmana.
Simulation of bubble column reactors with interphase mass transfer (quarterly report).
Technical report, Twente University, TNW/FAP, 2002.

R. DeBar.
Fundamentals of the kraken code.
Technical Report UCIR-760, LLNL, 1974.

N. G. Deen.
An Experimental and Computational Study of Fluid Dynamics in Gas-Liquid Chemical Reactors.
PhD thesis, Aalborg University, Esbjerg, Denmark, 2001.

E. Delnoij.
Fluid Dynamics of Gas-Liquid Bubble Columns, A Theoretical and Experimental Study.
PhD thesis, Twente University, The Netherlands, 1999.

E. Delnoij, F. A. Lammers, J. A. M. Kuipers, and W. P. M. van Swaaij.
Dynamic simulation of dispersed gas-liquid two-phase flow using a discrete bubble model.
Chemical Engineering Science, 52(9):1429–1458, 1997.

A. Esmaeeli and G. Tryggvason.
Direct numerical simulations of bubbly flows. part 1. Low reynolds number arrays.
Journal of Fluid Mechanics, 377:313–345, 1998.

A. Esmaeeli and G. Tryggvason.
Direct numerical simulations of bubbly flows. part 2. Moderate reynolds number arrays.
Journal of Fluid Mechanics, 385:325–358, 1999.

Short Courses : Modelling and Computations of Multiphase Flows, volume IIB, March 1999. ETH Zurich.

M. J. V. Goldschmidt.
Hydrodynamic Modelling of Fluidised Bed Spray Granulation.
PhD thesis, Twente University, The Netherlands, 2001.

J. R. Grace.
Shapes and velocities of bubbles rising in infinite liquids.
Trans. Instn. Chem. Eng., 51:116–120, 1973.

F. H. Harley, L. L. Smarr, and J. R. Wilson.
A numerical study of nonspherical black hole accretion. ii. finite differencing and code calibration.
Astophys. J. Suppl. Ser., 55:211–246, 1984.

F. H. Harlow and J. E. Welch.
Numerical calculations of time-dependent viscous incompressible flow of fluid with free surfaces.
Physics of Fluids, 8:2184–2189, 1965.

C. W. Hirt and B. D. Nichols.
A computational method for free surface hydrodynamics.
Journal of Pressure Vessel technology, 103:136, 1981.

B. Hoomans.
Granular Dynamics of Gas-Solid Two-Phase Flow.
PhD thesis, Twente University, The Netherlands, 2000.

C. B. Jacobsen.
Large Eddy Simulation of Confined Swirling Flow - a Numerical and Experimental Investigation of Isothermal Combustion Chamber Flows.
PhD thesis, Aalborg University, Denmark, 1997.

H. A. Jakobsen, B. H. Sannæs, S. Grevskott, and H. F. Svendsen.
Reviews: Modeling of vertical bubble-driven flows.
Industrial and Engineering Chemical Research, 36:4052–4074, 1997.

H. A. Jakobsen and H. F. Svendsen.
Challenges on predictive fluid dynamic modeling of bubble column reactors.

In *CD-ROM*. CHISA 2000, August 2000.
Abstract printed in book of Abstracts and full text on CD-ROM.

D. B. Kothe, R. C. Mjolsness, and M. D. Torrey.
Ripple: A computer program for incompressible flows with free surfaces.
Technical report, Los Alamos National Laboratory, October 1994.
http://gnarly.lanl.gov/home.html.

A. Lapin and A. Lübbert.
Numerical simulation of the dynamics of two-phase gas-liquid flows in bubble columns.
Chemical Engineering Science, 49(21):3661–3674, 1994.

B. D. Nichols and C. W. Hirt.
Improved free surface boundary conditions for numerical incompressible-flow calculations.
Journal of Computational Physics, 8:434–448, 1971.

B. D. Nichols and C. W. Hirt.
Methods for calculating multi-dimensional, transient free surface flows past bodies.
Technical Report LA-UR-75-1932, Los Alamos National Laboratory, 1975.
[Appeared in the first International conference on Numerical Ship Hydrodanymics, Gaithersbrug, MD,10/75].

W. F. Noh and P. R. Woodward.
SLIC(simple line interface mehtod).
Lecture Notes in Physics, 59:330, 1976.

S. V. Patankar.
Numerical Heat Transfer and Fluid Flow.
Taylor & Francis, 1980.

C. S. Peskin.
Numerical analysis of blood flow in the heart.
Journal of Computational Physics, 25:220–252, 1977.

C. S. Peskin and D. M. McQueen.
Mechanical equilibrium determines the fractal fiber architecture of aortic heart-valve leaflets.
American Journal of Physiology, 266(1)(part 2):H319–H328, January 1994.

A. Prosperetti.
Navier-Stokes numerical algorithms for free-surface flow computations: An overview.
In *To appear in the proceedins of CISM Course on Drop-Surface Interactions*, page 21, 2001.

M. Raffel, C. Willert, and J. Kompenhans.
Particle Image Velocimetry.
Springer, 1998.
ISBN 3-540-63683-8.

W. J. Rider and D. B. Kothe.
Reconstructing volume tracking.
Journal of Computational Physics, 141:112–152, 1998.

W. J. Rider, D. B. Kothe, J. J. Mosso, J. H. Cerutti, and J. I. Hochstein.
Accurate solution algorithms for incompressible multiphase flow.
Technical Report 95-0699, AIAA, 1995.
also available at : http://laws.lanl.gov/XHM/personnel/wrj/Web_papers/pubs.html.

M. Rudman.
Volume-tracking methods for interfacial flow calculations.
International Journal for Numerical Methods in Fluids, 24:671–691, 1997.

M. Rudman.
A volume-tracking method for incompressible multifluid flows with large density variations.
International Journal for Numerical Methods in Fluids, 28:357–378, 1998.

P. Sagaut.
Large Eddy Simulations for Incompressible Flows.
Springer, 2001.
ISBN 1434-8322.

S. Shin and D. Juric.
Modelling three-dimensional multiphase flow using a level contour reconstruction method for front tracking without connectivity.
Journal of Computational Physics, 180:427–470, 2002.

M. Sommerfeld.

Overview of fundamentals part i and ii.
In *Theoretical and Experimental Modelling of Particle Flows*, April 2000.

A. Tomiyama.
Struggle with computational bubble dynamics.
In *Third International Conference on Multiphasse Flow*, 1998.

A. Tomiyama, K. Miyoshi, H. Tamai, I. Zun, and T. Sakaguchi.
A bubble tracking method for the prediction of spatial evolution of bubble flow in a vertical pipe.
In *3rd. International conference on multiphase flow*. ICMF, 1998.

A. Tomiyama, A. Sou, I. Zun, N. Kanami, and A. Sakaguchi.
Effects of eötvös number and dimensionless liquid volumetric flux on lateral motion of a bubble in laminar duct flow.
In *Multiphase Flow 1995, Proceedings of the Second International Conference on Multiphase Flow*, pages 3–15, 1995.

J. A. Trapp and G. A. Mortensen.
A discrete particle model for bubble-slug two phase flow.
Journal of Computational Physics, 107:367–377, 1993.

G. Tryggvason.
Embedded interface methods.
In *Short Courses : Modelling and Computations of Multiphase Flows* ETH (1999).

G. Tryggvason, B. Bunner, O. Ebrat, and W. Tauber.
Computations of multiphase flows by a finite difference/front tracking method. i. multi-fluid flows.
In *29th Computational Fluid Dynamics Lecture Series*, pages 1–44. Von Karman Institute for fluid Dynamics, March 1998.

G. Tryggvason, B. Bunner, A. Esmaeeli, D. Juric, N. Al-Rawahi, W. Tauber, J. Han, S. Nas, and Y.-J. Jan.
A front tracking method for the computations of multiphase flow.
Journal of Compuatational Physics, 169:708–759, 2001.

S. O. Unverdi and G. Tryggvason.
A front-tracking method for viscous, incompressible, multi-fluid flows.
Journal of Computational Physics, 100:25–37, 1992.

R. van Damme and L. Alboul.
Tight triangulations.
Mathematical Methods for Curves and Surfaces, pages 517–526, 1995.

J. van Oord, S. Sinnema, and J. Landskroon.
Development of an ultrasonic measurement technique in liquid metals.
In *Conference preprints 2th international congress on the Science & technology of steelmaking*. The intitute of materials, April 2001.

D. L. Youngs.
Time-dependant multi material flow with large fluid distortion.
In K. W. Morton and B. J. Baines, editors, *Numerical Methods for Fluid Dynamics*, pages 273–285. Academic, New York, 1982.

D. L. Youngs.
An interface tracking method for a 3d Eulerian hydrodynamics code.
Technical Report AWRE/44/92/35, Atomic Weapons Research Establishment, April 1987.

S. Zaleski.
Multiphase-flow cfd with volume of fluid (vof) methods.
In *Short Courses : Modelling and Computations of Multiphase Flows* ETH (1999).

Curriculum Vitae

Michiel Gunsing werd geboren op 17 december 1971 in IJsselstein. Na het lager onderwijs in Wessem werd met goed gevolg het VWO doorlopen aan de scholengemenschap st. Ursula te Horn.

In augustus 1990 begon hij zijn studie Chemische technologie aan de Universiteit Twente die in 1996 werd afgerond met een afstudeeropdracht bij de groep proceskunde en het behalen van de ingenieurs (ir.) titel.

Na zijn studie trad hij in dienst bij PURAC biochem bv alwaar hij als GMP validatiespecialist de kwaliteit van de pharmaceutische procesinstallaties documenteerde.

In september 1998 begon Michiel alsnog aan een promotieproject bij de vakgroep proceskunde o.l.v W.P.M van Swaaij. Gaande het project werd deze groep gesplitst in een groep Ontwerp Ontwikkeling van Industriele Projecten (OOIP) o.l.v. G. Versteeg en Fundamentele Aspecten van de Proceskunde (FAP) o.l.v. J.A.M. Kuipers, alwaar het project werd voortgezet en afgerond.

Op 23 juni 2000 trouwde hij met Isabel van Beckum. Op 20 maart 2001 werd hun dochter Emma geboren en twee jaar later op 29 maart 2003 volgde Cecile.

Vanaf 16 september 2002 is Michiel in diens bij NIZO food research als projectleider predicive modelling.

Dankwoord

In de afgelopen vijf en een half jaar is er erg veel werk verzet dat uiteindelijk heeft geleid tot dit proefschrift. Er is een persoon die het aan elkaar geschreven heeft en zijn naam op dit boekje heeft gezet, maar een proefschrift komt niet tot stand zonder de medewerking van velen die op een of andere manier een bijdrage hebben geleverd.

Mijn dank gaat uit naar Hans Kuipers voor zijn begeleiding, discussies en correctiewerk. Ook Martin van Sint Annaland als begeleider. Martin ondanks je late instap in dit project is het je gelukt op niveau mee te discussieren.

Dank ook aan alle collega computeraars die inhoudelijk hebben bijgedragen aan de inhoud van dit werk: Mathijs, Arnoud, Esther, Bob en later ook Albert, Jeroen en Ji. Met Mathijs en Arnoud heb ik tijden een 'eigen' kantoor gedeeld waar zebravinken en de rode klapper voor de nodige afleiding zorgden. Goede herinneringen heb ik aan aan de zeilweekenden en de bijbehorende barbecues.

Ook dank aan Wim van Swaaij. Onze ontmoeting waren laag in aantal maar hoog van kwaliteit.

Een groot deel van met name het experimentele werk dat helaas niet tot dit boekje is doorgedrongen is door de studenten verricht die bij mij afstudeerden een prakticum opdracht vervulden of anderszinds bij mijn project betrokken waren. Albert Bokkers, Leobert van der Groep, Ciske Dillerop, François Broust, Jeroen van Schagen en Bob Lefeber. Allen bedankt.

Voor de technische ondersteuning kon ik altijd terugvallen op een goede basis. Benno, Wim, Gerrit, Henk-Jan, Robert voor de experimentele zaken en de mannen van SGA voor hun ondersteuning met het grote computermaterieel. De SGI machines en het linux cluster. Jan, Joachim, Gilbert en Bert.

Allemaal bedankt!

CORUS wil ik danken voor hun financiële ondersteuning die dit project mogelijk maakte en in het bijzonder Wico Verloop, Ivo Opstelten en Sjaak van Oord die als projectleider vanuit Beverwijk, aan dit project hebben getrokken. Eveneens ook dank aan Jan Landskroon die de probes voor de meetresultaten vervaardigde en Piet Commandeur en Cees van der Zwet Slotenmaker van het laboratorium die de experimenten met vloeibaar aluminium en ijzer hebben uitgevoerd.

Ook de inzet van Kees Venner waardeer is zeer. Ik had graag een draaiende multi-grid solver in mijn code gehad maar helaas was de tijd tekort om dit voor elkaar te krijgen.

Frits van Beckum bedank ik voor al zijn bijdragen op zijn vakgebied en de Engelse taal, als klankbord, als printer operator en postbode in tijden dat de de PTT of de interne post het liet afweten.

Jenny, dank voor je correctiewerk en je telefoonsupport, ze gaven een geheel nieuwe kijk op de Engelse taal.

Uiteraard ook dank aan Arnoud Higler (nogmaals) en Marcel Kaljee die mij als paranimfen hebben gesteund in de voorbereiding van, en tijdens de verdediging van mijn proefschrift.

Tot slot wil ik Isabel bedanken voor haar nimmer aflatende steun tijdens de hoogte en dieptepunten die er tijdens deze promotie zijn geweest. Emma en Cecile dank ik voor de tijd dat ze mij hebben moeten missen. Vanaf nu is papa er weer helemaal bij.